10-21-2019

Ultrafast and Real-Time Dynamics of Nanomaterials Studied by Advanced Spectroscopic Techniques

Jeewan Chaminda Ranasinghe
Louisiana State University and Agricultural and Mechanical College

ULTRAFAST AND REAL-TIME DYNAMICS OF NANOMATERIALS STUDIED BY ADVANCED SPECTROSCOPIC TECHNIQUES

A Dissertation

Submitted to the Graduate Faculty of the
Louisiana State University and
Agricultural Mechanical College
in partial fulfillment of the
requirements for the degree of
Doctor of Philosophy

in

The Department of Chemistry

by
Jeewan Chaminda Ranasinghe
B.S. University of Peradeniya, 2010
December 2019

This PhD Dissertation is
Dedicated to
My Family Members

Acknowledgements

Attending graduate school has been a very humbling experience, and I could not complete this journey without the help of many others. I would like to take this time to express thanks to the many people who have helped and supported me during my time in graduate school. The work in this thesis could not have been completed without you.

I am very thankful to Professor Louis Haber for granting me the opportunity to join his research group and to enter the world of ultrafast lasers. Additionally, I would like to thank him for his valuable guidance, support, and vision on research and life. The work in this PhD, and furthermore after this PhD, would not be possible without Dr. Haber, a man of immense vision and ideas.

I am also thankful for my committee members, Professor Bin Chen, Professor Kenneth Lopata, Professor George Stanley, and Professor Evan Agullo, who have guided me on my research and brought their expertise to my research projects. Additionally, I would like to thank Professor Isiah Warner and Professor Kevin McPeak for their excellent collaborations. I am very thankful for Ying Xiao for her help with electron microscopy and Dr. Rafael Cueto for help with dynamic light scattering measurements.

I have to thank the former and current members of the Haber group: Dr. Tony Karam, Dr. Raju Kumal, Dr. Rami Khoury, Dr. Holden Smith, Prakash Hamal, Asela Dikkumbura, and Min Chen as it has been a pleasure working with you all. It is a rare thing to find coworkers who devote their time, resources, and effort to the success of others and you guys are an ideal example of that. To all my friends from the class of 2014, thank you for making the last five years an unforgettable experience.

Family and friends have been important so I would like to thank my parents Chandani Kalyanasseli and Hector Ranasinghe, who cultivated a scientific curiosity and always push me to be the best of best. I would also like to thank my sisters Vindhya Ranasinghe, Kalani Ranasinghe, and Ishani Ranasinghe. Without the love and support of my family, I would not be here today.

This work was supported in part by the National Science Foundation EPSCoR CIMM project under award OIA-1541079. So, I would like to thank generous financial support throughout my graduate career.

Table of Contents

List of Figures

Abstract

Ultrafast and nonlinear spectroscopies are used to study excited-state dynamics and monitor real-time growth dynamics of different types of nanomaterials. In the first study, the growth dynamics of colloidal gold-silver core-shell nanoparticles are studied using *in situ* second harmonic generation and extinction spectroscopy. The growth lifetimes are studied under different reaction conditions, resulting in different silver shell thicknesses, with spectral comparisons to finite-difference time-domain calculations. The results are consistent with a three-step growth process. During the first step of the nanoparticle growth reaction, rough and uneven surfaces are formed rapidly giving rise to plasmonic hot spots with corresponding broad, red-shifted plasmon spectra. In the second step, the nanoparticle surface becomes smoother, reaching a thermodynamic equilibrium. The Au@Ag nanoparticle growth process has a third, slower step where the nanoparticle surface charge density changes due to chemical reactions resulting in a decreasing SHG signal while the extinction spectrum remains constant. In another study, transient absorption spectroscopy is used to study the ultrafast dynamics of porphyrin- and zinc porphyrin-based colloidal nanomaterials for potential applications in light-harvesting devices. Porphyrin and zinc porphyrin dyes in water exhibit long-lived excited states on the order of several nanoseconds. However, these porphyrin excited-state lifetimes are significantly faster when in the nanoparticle environment due to energy transfer, enhanced intersystem crossing, and electronic delocalization. Finally, the excited-state heating and melting dynamics of aluminum thin film samples at different thicknesses are investigated using ultrafast pump-probe reflectivity with 800 nm light under varying laser pump pulse powers. The data reveal a dramatic change in the carrier

relaxation mechanism below and above 150 nm in thickness under varying laser powers due to the role of the characteristic heat penetration depth. Samples with thickness below this length scale show faster heating dynamics and a lower power threshold for melting. Overall, the synthesis, characterization, nonlinear spectroscopy, and ultrafast spectroscopy of a wide variety of nanomaterials are studied for the development of potential nanomedicine, optoelectronic, molecular sensing, and laser-based additive manufacturing applications.

Chapter 1. Introduction to Nanomaterials and Advanced Spectroscopic Techniques

1.1 Engineered Nanomaterials and Characterization

Low dimensional structures, such as nanostructured materials, nanoparticles, and thin films, have drawn significant research interest due to their unique chemical, optical, electronic, mechanical, and magnetic properties that can be utilized in areas such as electronics, photovoltaics, catalysis, materials engineering, and biologically-relevant applications.[1-2] Typically, nanomaterials are described as a type of material where the dimension of a single unit spans from a nanometer to several hundreds of nanometers, essentially creating an intermediate regime between atoms or molecules and bulk materials. As a result of reduced dimensionality, the properties of nanomaterials are often dramatically altered from the bulk counterparts caused by surface effects and quantum size effects.[3] One specific property that distinguishes nanomaterials is a very large surface to volume ratio.

In order to improve the applicability of nanomaterials, a detailed understanding of the general properties, surface properties, and stability is crucial. To date, tremendous advances have been achieved in the synthesis of nanomaterials with controllable sizes, shapes, compositions, architectures, and chemical functionalities.[2] Optical absorption and emission spectroscopies are widely-used, conventional characterization tools to investigate the optoelectronic properties of nanoparticles in colloidal suspensions or thin films. However, additional methods of spectroscopic analysis of nanomaterials can provide more insight relating to the photodynamics and surface chemistry in order to further develop the potential applications of nanomaterials and their associated emerging technologies. For example, time-domain techniques based on pulsed lasers enable

research on the optical and dynamic properties of nanomaterials. The utilization of the ultrafast lasers, where the laser pulse duration is on the sub-picosecond timescale, allows for advanced optical ultrafast spectroscopic measurements in the nanomaterial sample.[4] Analyzing the excited state dynamics and surface states of nanomaterials can also give mechanistic details regarding light-matter interactions at nanoscale dimensions.[5] Additionally, nonlinear spectroscopy provides detailed information on nanomaterial surfaces and the corresponding dynamics occurring at these interfaces. A primary focus of this thesis is the development of ultrafast and nonlinear spectroscopic techniques for the investigation of different types of nanomaterials.

1.2 Different Types of Nanomaterials

1.2.1 Plasmonic Nanomaterials

Metallic nanoparticles possess many unique chemical, electronic, and optical properties that make them promising candidates for applications in several fields such as photovoltaics,[6] catalysis,[7-8] sensing probes,[9] therapeutic agents,[10] and drug-delivery applications.[11] The optical properties of metallic nanoparticles such as gold and silver are characterized by their localized surface plasmon resonances (LSPRs) which are described as a collective oscillation of free electrons driven by incident electromagnetic radiation. Figure 1.1 shows a schematic illustration of a surface plasmon resonance of a metallic nanoparticle induced by an optical electromagnetic field. In this respect, particles much smaller than the wavelength of incident radiation have optical interactions which give rise to absorption, scattering, and coupling properties that depend on the nanoparticle's size, shape, composition, surrounding environment, and other possible interactions between nearby particles.[4-5] The plasmon resonances can cause significant

optical field enhancements leading to processes such as surface-enhanced Raman scattering (SERS), surface-enhanced fluorescence, and plasmon-exciton polariton resonance coupling.[12-15] Extensive research efforts devoted to metal nanoparticle plasmonics is largely motivated by developing improved synthesis routes together with advances in lithography techniques, sophisticated characterization tools, and advances in theoretical simulations and modeling.[3]

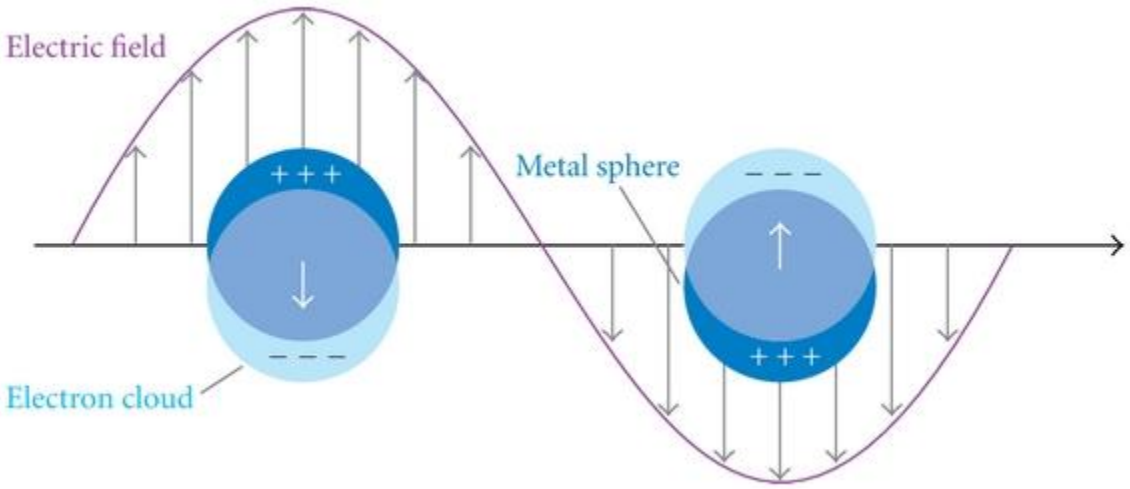

Figure 1.1. Electromagnetic field induced coherent localized oscillations of the electron cloud. [3]

Most of the metal nanoparticle plasmonics literature is dominated by gold and silver due to their strong LSPR bands in the visible region of the electromagnetic spectrum. Small spherical gold and silver nanoparticles of sizes of approximately 10 to 50 nm are characterized by single, relatively sharp, size-dependent plasmon bands. As the nanoparticles get larger, approaching the scale of 100 to 300 nm higher-order resonance terms such as quadrupole and octupole terms also contribute significantly to the overall absorption and scattering plasmon spectra. Other LSPR modes can appear

due to non-spherical shapes in anisotropic particles such as nanorods.[3, 16] Additionally, sharp surface features on metallic nanomaterials can produce intense electromagnetic radiation due to the contribution from the lightning rod effect providing a means for surface-enhanced spectroscopic methods.[17]

The applications that are related to LSPRs rely heavily on the ability to produce high-quality nanomaterials. Numerous methods have been reported for the synthesis of metallic nanoparticles, including chemical,[18-19] sonochemical,[20] microwave-assisted,[21] and photochemical routes.[22] The chemical colloidal synthesis method, where metal precursor material is reduced by a suitable reducing agent, is very advantageous due to its simplicity and its ability to form high-quality nanoparticles.[3] Additionally, the control of the nucleation and growth processes are possible by careful adjustment of reagent concentration in order to control the nanoparticle size while minimizing polydispersity. These strategies can be extended through the formation of core-shell structures, where a continuous shell of one material is grown to surround a nanoparticle core of another material. A general observation is the attenuation of the plasmon resonance of the core nanoparticle as the shell grows, leading to the dominance of the optical properties by the shell structure. The choice of shell material of these nanostructures depends critically on the end application and the desired functionality of final core-shell nanomaterial.[23-24] The versatility of these core-shell nanoparticles are due to an overall optical tunability over a broad wavelength range that is accessed through independent manipulation of the structure and composition of the core and shell separately.[25] For example, bare gold nanoparticles exhibit an extinction peak near 530 nm. However, after coating the gold core with a silver shell, the resulting gold-silver core-shell nanoparticle extinction peak

significantly blue shifts to around 420 nm, which is close to the LSPR band of a silver nanoparticle. The extinction spectrum of this core-shell nanocomposite can be further modified by adding an outer gold layer shell, which then moves the extinction peak to the near infrared region, providing exciting new opportunities in the field of nanomedicine, for example.[26-27]

Several techniques have been developed in recent years for single-particle measurements to reveal the inherent linear and nonlinear optical responses of nanoparticles.[28-29] In addition to having well-established synthetic protocols and characterization techniques, the development of an accurate theoretical understanding of the plasmonic spectra is essential for progress in metal nanoparticle plasmonics research. In this context, finite difference time domain (FDTD), discrete dipole approximation (DDA), multiple multipole method (MMP), multiple scattering techniques, transfer matrix approaches, plane wave expansions, and boundary element methods (BEM) are available as the most commonly used methods.[3] Significant and potentially transformative advances in the field of plasmonics and nanomaterials have been achieved through recent years, which can be applied in wide-ranging technologies. Advanced spectroscopic techniques play a major role in this research since these characterization tools can provide detailed information on light-matter interactions at the nanoscale.

1.2.2 NanoGUMBOS

Nanomaterials derived from organic and organometallic molecular compounds have also drawn special attention in fields such as nanomedicine, biosensing, and optoelectronics.[30-31] Solid-phase organic salts achieved by counter ion alteration are termed as a group of uniform materials based on organic salts (GUMBOS).[32] These materials are distinguishable from liquid state organic salts (or ionic liquids) in terms of their melting point, where GUMBOS show an extended range of melting points from 25 °C to 250 °C, compared to a lower melting point range (< 100 °C) displayed by ionic liquids. NanoGUMBOS are nanoparticles derived from GUMBOS, and are especially interesting when one of the molecular salts has large optical extinctions. In addition to providing new fundamental insight into molecular-based nanomaterials, the unique optoelectronic properties of nanoGUMBOS makes them promising candidates for next-generation photovoltaics,[33] bio-imaging,[34], and organic light emitting diodes.[35]

In order to maximize the potential of nanoGUMBOS for improved applications, a fundamental understanding of the excited-state relaxation dynamics is essential. This can be achieved by pump-probe spectroscopic measurements, such as transient absorption spectroscopy, which can provide information on mechanisms such as charge transfer, electron transfer, intermolecular energy transfer, fluorescence, singlet to triplet state transitions, vibrational and phonon-assisted relaxations, and hindered molecular conformational motions. Previously, our research group has reported on excited-state dynamics of colloidal ruthenium bipyridine–bis(pentafluoroethylsulfonyl) imide ($[Ru(BIPY)_3]$-$[BETI]_2$) nanoGUMBOS characterized by spectral shifts and size-dependent ultrafast relaxation dynamics.[36] A detailed analysis shows these crystalline

nanoGUMBOS exhibit long live phonon oscillations with frequencies that increase as nanoparticle size increases due to hydrophobic solvent interactions at the nanoparticle surface. More recently we investigated the excited-state relaxation dynamics of brilliant green–bis(pentafluoroethylsulfonyl)imide ([BG][BETI]) nanoGUMBOS which are characterized by longer lifetimes compared to the brilliant green molecular dye due to steric hindrance of the BG molecule in the nanoGUMBOS environment.[37] In general, future work is needed to better understand the complicated photodynamics of different types of nanoGUMBOS samples for advancing potential optoelectronic applications in these novel molecular-based nanomaterials.

1.2.3 Metallic Thin Films

In recent years, metallic thin films have been another area of intense interest due to their ability to provide versatile and multifaceted platforms for a broad range of applications in areas such as high reflective mirrors,[38] field-effect transistors,[39] hot-electron photochemistry,[40] and laser ablation for the processing of materials.[41] However, depositing high-quality metallic films with high purity and low surface roughness is challenging and requires expertise in controlling the underlying chemistry of the film deposition.[42] Using temperature-controlled sputtering techniques, chemical bath deposition, and epitaxial growth, metallic films ranging from tens of nanometers to the micrometer scale in thickness can be produced on top of suitable substrates.[42-43]

Metallic thin films also enable fundamental studies to be carried out involving laser-metal interactions on the nanoscale as a function of thickness. As the film thickness increases, the metal material become more bulk-like in property. Research on metallic thin films using different types of ultrafast laser heating, combined with theoretical models,

represent important progress for advancing laser-based manufacturing processes such as selective laser melting for additive manufacturing applications.[44-46] Important complementary characterizations of metallic thin films include measuring the optical response from variable-angle spectroscopic ellipsometry, allowing for the determination of real and imaginary parts of the dielectric constant.[47-48] Additionally, the electron and lattice dynamics of metallic thin films can be studied using ultrafast optical pump-probe reflectivity measurements, which will be described in more detail in later sections.[49-50]

1.3 Advanced Spectroscopic Techniques

1.3.1 Second Harmonic Generation

Nonlinear optical spectroscopies, which include second harmonic generation (SHG), sum frequency generation (SFG), third harmonic generation (THG), have been used for several decades to investigate chemical and physical processes in systems such as biological interfaces,[51-53] nanomaterials,[54-55] small molecules,[56] and complex materials.[57] These nonlinear optical techniques can reveal detailed information relating to the study of interfacial acid-base chemistry,[58] surface potential measurements,[59] molecular transport through lipid bilayers,[60-62] molecular orientation, structure, and energetics of interfacial processes,[56, 58, 63-64] and *in situ* growth of colloidal nanomaterials.[65-66]

SHG is a second-order nonlinear optical spectroscopy in which two photons at the frequency ω add coherently to generate a single photon at twice the frequency 2ω. This process is depicted schematically in Figure 1.2 Within the dipole approximation, the SHG signal from centrosymmetric and isotropic bulk media cancels out completely and is therefore not allowed. However, at interfaces, the local symmetry is broken and the SHG

signal is allowed, making SHG spectroscopy an excellent method for investigating interfacial phenomena. The SHG signal has contributions from the second-order and third-order nonlinear susceptibilities, $\chi^{(2)}$ and $\chi^{(3)}$, respectively. The $\chi^{(2)}$ term originates from the two-photon spectroscopy of the surface, while the $\chi^{(3)}$ term is a result of the electric field of the surface inducing a net polarization of nearby bulk molecules, for example in the solvent.[59] Additionally, the intensity of the radiated light is proportional to the absolute square of the effective second-order nonlinear susceptibility χ^2_{eff} and the strength of the incident light. The effective second-order nonlinear susceptibility is the sum of resonant and nonresonant contributions.

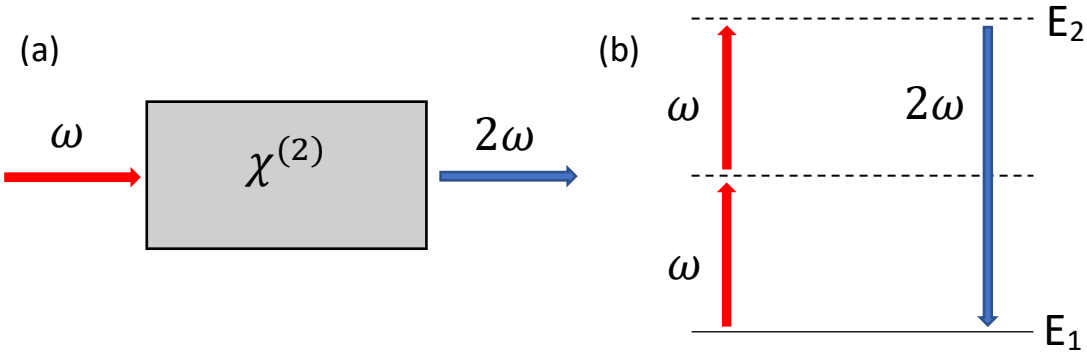

Figure 1.2. (a) Schematic of second harmonic generation from an isotropic material (b) Two-level system for second harmonic generation.

The second harmonic generation signal can also be enhanced in different plasmonic nanoparticles and nanoarchitectures due to increased surface optoelectronic fields. For example, the SHG response from gold and silver nanospheres, silver nanoprisms, gold nanocups, gold nanostars, and several lithographed nanoparticles have been reported, showing large effective second-order nonlinear susceptibilities, especially when the fundamental wavelength or SHG wavelength is resonant with the plasmonic

energy.67-68 In addition, by careful nanoengineering of plasmonic nanostructures, it is possible to produce areas on the surface called “hot spots” where multiple folds of enhancement in an electric field which can be obtained, which significantly increase the nonlinear optical signals generated.67 These plasmonic effects, combined with enhanced surface sensitivity, make SHG a powerful optical probe of metallic nanoparticle samples.

1.3.2 Ultrafast Transient Absorption Spectroscopy

Observation of ultrafast processes is critical for fully understanding dynamics that take place on picosecond or femtosecond timescales including molecular vibrations, atomic motion, absorption, scattering, and emission.[69] This highlights the importance of having ultrafast laser pulses, since the uncertainty in timing must be smaller than the timescale of the process being studied, requiring temporal resolution on the order of 10^{-15} s. Remarkable progress in laser technology and the introduction of Titanium:sapphire lasers have allowed researchers to resolve the ultrafast dynamics of different systems with this high temporal resolution.[70-71] For example, by using sub 100 fs laser pulses, one can take a snapshot of excited state relaxation dynamics of a system under investigation by taking advantage of pump-probe spectroscopic techniques with controlled and varied pump-probe temporal delays.[5, 72]

Ultrafast transient absorption spectroscopy (TAS) can provide detailed information about excited-state dynamics, including electron transfer, energy transfer, internal conversion, and intersystem crossing in a sample of interest.[70, 73-75] Samples such as dyes in solution and nanoparticles in colloidal suspension can be studied using this ultrafast spectroscopic technique. Figure 1.3 illustrates the key concept behind the typical pump-probe spectroscopy setup. In a typical transient absorption experiment, the

absorbance at a particular wavelength or over a range of wavelengths is measured as a function of the ultrafast pump-probe delay (t) after excitation by a pump pulse. In this regard, the difference absorption spectrum (ΔA) is calculated which is attributed to the change in the excited-state absorption spectrum minus the change in the ground-state absorption spectrum. The experimental data typically consists of multiple difference absorption spectra collected at various time delays between excitation pump and probe pulses at different wavelengths, which can be denoted as $\Delta A(\lambda, t)$. There are numerous contributing species for $\Delta A(\lambda, t)$ which results in different transient absorption signals. In general, a negative ΔA signal is primarily due to ground state depletion and stimulated emission. A positive signal is primarily attributed to excited-state absorption. Furthermore, global analysis of the wavelength-dependent time traces can be applied to separate various contributing chemical species and associated processes in a series of time-dependent transient absorption spectra.

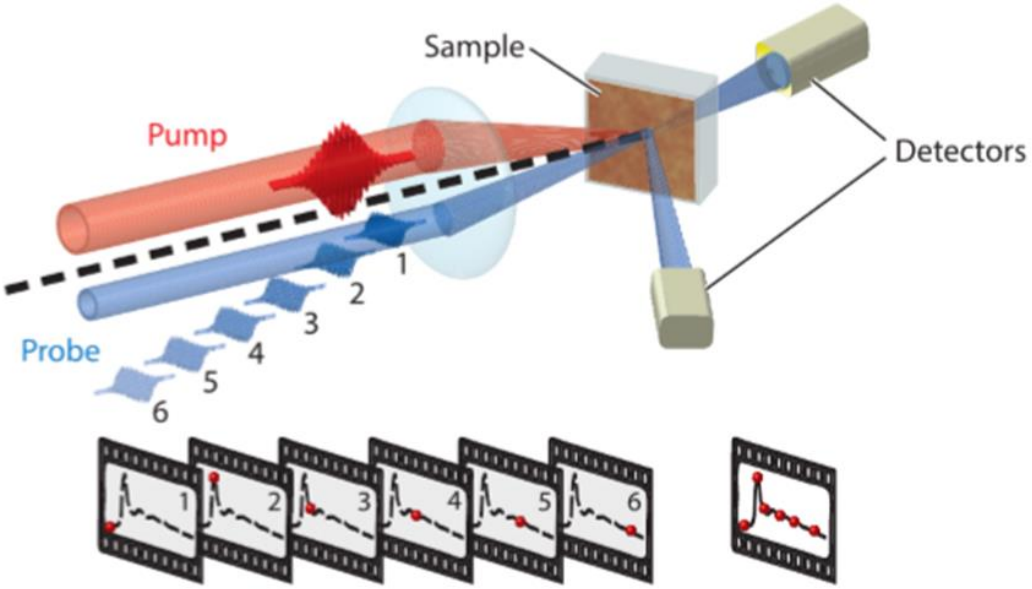

Figure 1.3. Schematic description of pump-probe spectroscopy setup. Snapshots of the transient state are taken to temporally resolve the nonequilibrium dynamics. [47]

1.3.3 Ultrafast Pump-Probe Reflectivity

Ultrafast pump-probe reflectivity (or transient reflectivity) is a foundational technique for studying excited state dynamics, interfacial transfer rates, recombination mechanisms, laser damage thresholds, heat-induced structural deformations, thermal transport mechanisms, and phase transitions of surfaces and thin-film materials.[71, 76-79] In a typical transient reflectivity experiment, the sample is excited with intense pump pulse and the change in reflectance is measured in reference to the nonexcited sample as a function of pump-probe time delay. The majority of pump-probe reflectivity studies on metallic thin films use laser powers which are far below the threshold of irreversible material damage, such that multiple scans can be acquired for a given laser condition to obtain reproducible results and statistical analysis of time traces.[49, 80-81] When laser powers are used that approach or exceed the damage threshold, additional characterizations are needed for combining the advantage of pump-probe reflectivity

studies with methods such as ellipsometry and microscopic tools under sample-scanning methods to gather pump-probe dynamics beyond the damage threshold.

The use of ultrashort femtosecond pulses to excite metals results in the formation of a non-Fermi distribution of conduction electrons.[82] This nonequilibrium gas then undergoes ballistic motion into deeper parts of the sample along with the development of a time-dependent electron temperature. Thermal equilibrium among hot electrons on ultrafast timescales is set by the collision between excited electrons and electrons around Fermi level, resulting in a temperature gradient with hot electrons diffusing into the bulk as a function of time.[75, 83] An important concept for the description of ultrafast laser heating of a metal sample is the two-temperature model, where the electron gas and metal lattice are considered as two coupled systems at their respective temperatures.[84] The hot electron bath in a colder lattice can be described by separate temperatures, T_e and T_l where T_e is electron temperature and T_l is lattice temperature, as described in Figure 1.4. Following femtosecond excitation, the electron population is subjected to ultrafast changes where the incident laser energy is absorbed and thermalized by the electrons. The phonon temperature of the lattice is then heated due to electron-phonon coupling which typically takes place on the picosecond temporal range. Additionally, energy dissipation to the surrounding takes place on the timescale of hundreds of picoseconds to nanosecond through the phonon-phonon coupling. The specific interactions of the laser and metal will depend on several factors such as the wavelength, laser power and pulse duration, real and imaginary dielectric constants, electron-phonon and phonon-phonon coupling strengths, and the thickness of the sample.

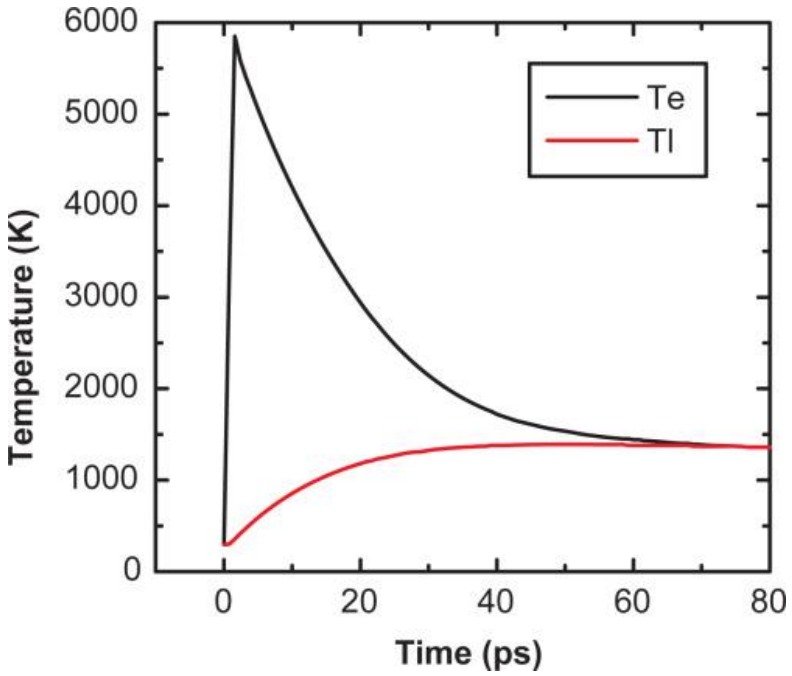

Figure 1.4. Schematic representation of variation of electron and lattice temperature after ultrafast laser excitation. [54]

1.4 *In Situ* Characterization of Nanomaterials

Precise, reproducible, and flexible control over the size and shape of metallic nanoparticles during synthesis is of great importance for providing new approaches in tailoring the chemical, structural, and plasmonic properties for a broad range of applications. Despite a large body of research devoted to understanding the optoelectronic properties of nanomaterials, the underlying reaction mechanisms and growth dynamics of nanomaterials are still far from being well understood. Research on the associated nanomaterial growth dynamics is needed for process parameter optimization in controlling nanoparticle synthesis and morphology in the field of nanoengineering. Therefore, a critical step is the development of *in situ* spectroscopic and microscopic tools for directly observing the nanomaterial growth process and related dynamics in greater detail.

Microscopic techniques such as transmission electron microscopy (TEM), scanning electron microscopy (SEM), and atomic force microscopy (AFM) are excellent tools to investigate surface nanostructures after completion of the formation reaction. When particle formation is taking place in colloidal suspension, these methods must be modified to include time-dependent measurements under sample conditions that are conducive for nanomaterial reactions under *in situ* measurement techniques. Several studies have focused on investigating the *in situ* growth of gold nanoparticles using methods such as small-angle X-ray scattering (SAXS), wide-angle X-ray scattering (WAXS), X-ray near-edge spectroscopy (XANES), and UV-Vis spectroscopy.[85-87] These technique have studied processes such as gold and silver nanoparticle growth and nucleation, and different core-shell growth processes in solution. However, this field of research is very new and only a small number of nanomaterials and their associated reaction dynamics have been investigated in detail.

Our research group has recently initiated a focused effort aimed at studying the real-time growth dynamics of different types of gold and silver plasmonic nanomaterials. Our first study focused on gold nanoparticles prepared through seed-mediated growth in aqueous colloidal solution.[65] More recently, our group extended this work to more complex nanoarchitectures such as bimetallic nanoparticles in core-shell configurations. We have observed significant differences between the growth dynamics of gold nanoparticles and gold-silver core-shell nanoparticles. The growth dynamics of gold-silver core-shell nanoparticles will be discussed in detail in Chapter 2.

Figure 1.5 shows the evolution of the extinction spectrum during the seed-mediated gold nanoparticle growth under five different seed concentrations, where all

other conditions are the same. The initial gold seed nanoparticles are 14 nm in diameter, while the final gold nanoparticles after the conclusion of the growth reactions are 92, 86, 73, 71, and 66 nm, corresponding to Figures 1.5 (a) to (e), respectively, as measured using TEM. The addition of sodium citrate and hydroquinone to a mixture of gold seeds and $HAuCl_4$ occurs at time zero, initiating the seed-mediated nanoparticle growth reaction dynamics. Before the addition of reducing agents, the extinction spectra have low intensities due to a contribution from small gold seeds together with the added gold chloride. Immediately after the addition of reducing agents, all five samples are characterized by a broad red-shifted spectrum which are attributed to sample polydispersity and surface roughness. As reaction progress, the extinction spectra become more narrow while also blue shifting, as described by the nanoparticle sample getting more monodisperse and the nanoparticle surfaces becoming more smooth. At longer times there is no change in the extinction spectra, indicating that the nanoparticles have reached thermodynamic stability and the completion of the growth reactions.

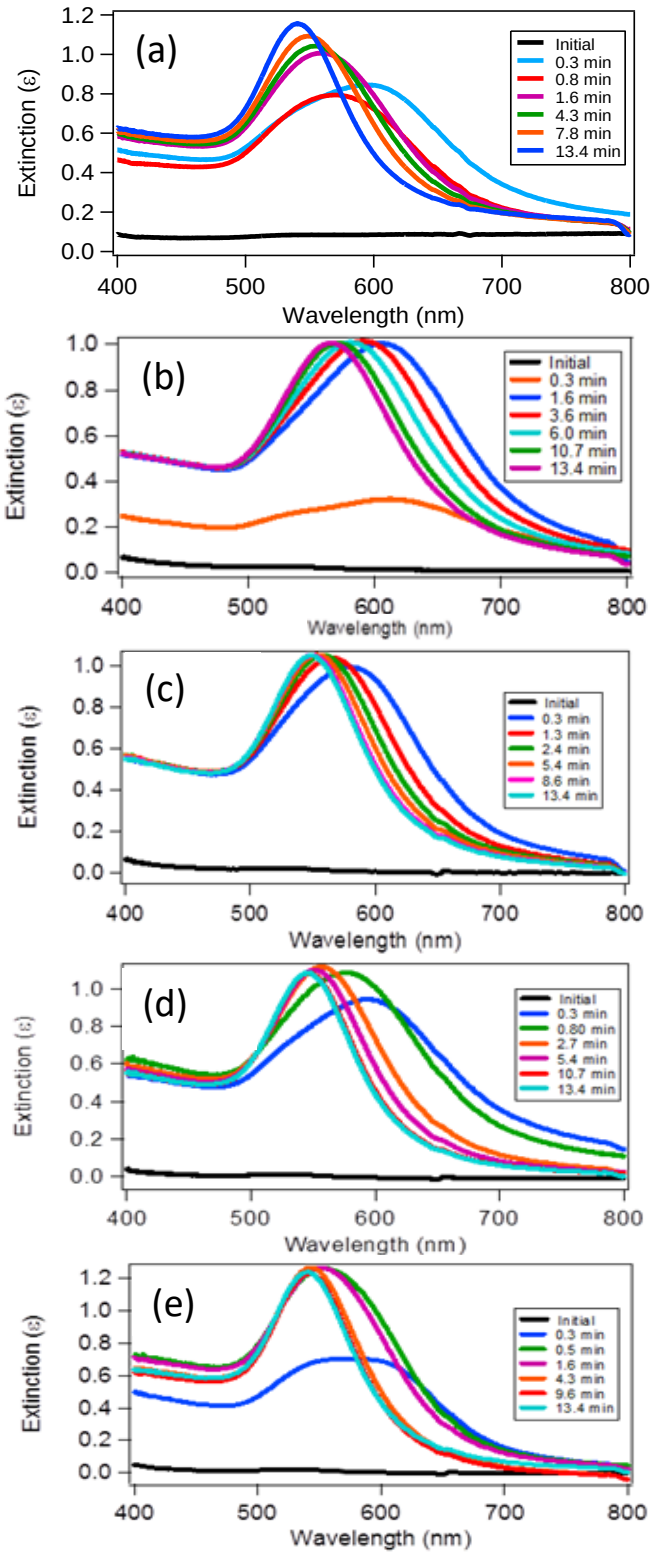

Figure 1.5. *In situ* extinction spectra of gold nanoparticles synthesized with (a) 25, (b) 30, (c) 35, (d) 40 and (e) 50 µL of precursor gold seeds at different times during the reactions. [43]

The seed-mediated growth dynamics of gold nanoparticles are also investigated in real-time using *in situ* SHG providing additional and complementary information. The temporal evolution of the SHG electric field for each nanoparticle sample is shown in Figure 1.6. The SHG intensity before time zero is very low because the gold seeds are all small in size. After the addition of reducing agents to the mixture, the SHG intensity increases significantly reaching a peak, then the SHG intensity decreases exponentially and finally reaches a minimum value. Each gold nanoparticle seed in solution grows into a larger gold nanoparticle from gold reduction at the surface. Under the same gold chloride and hydroquinone bulk concentrations, samples with lower gold seed concentrations grow into larger nanoparticles since more gold material is added per seed. Additionally, it is important to point out that the SHG signal for colloidal nanoparticles smaller than $\lambda/2$ typically scales as approximately r^6, where r is the nanoparticle radius.[88-89] The final SHG signals per nanoparticle of the seed-mediated nanoparticle growth is highest for the largest nanoparticle size and lowest for the smallest nanoparticle sizes, as expected. The stable and constant SHG signal after corresponding reaction times indicates the complete and stable formation of the nanoparticle sample for all five cases.

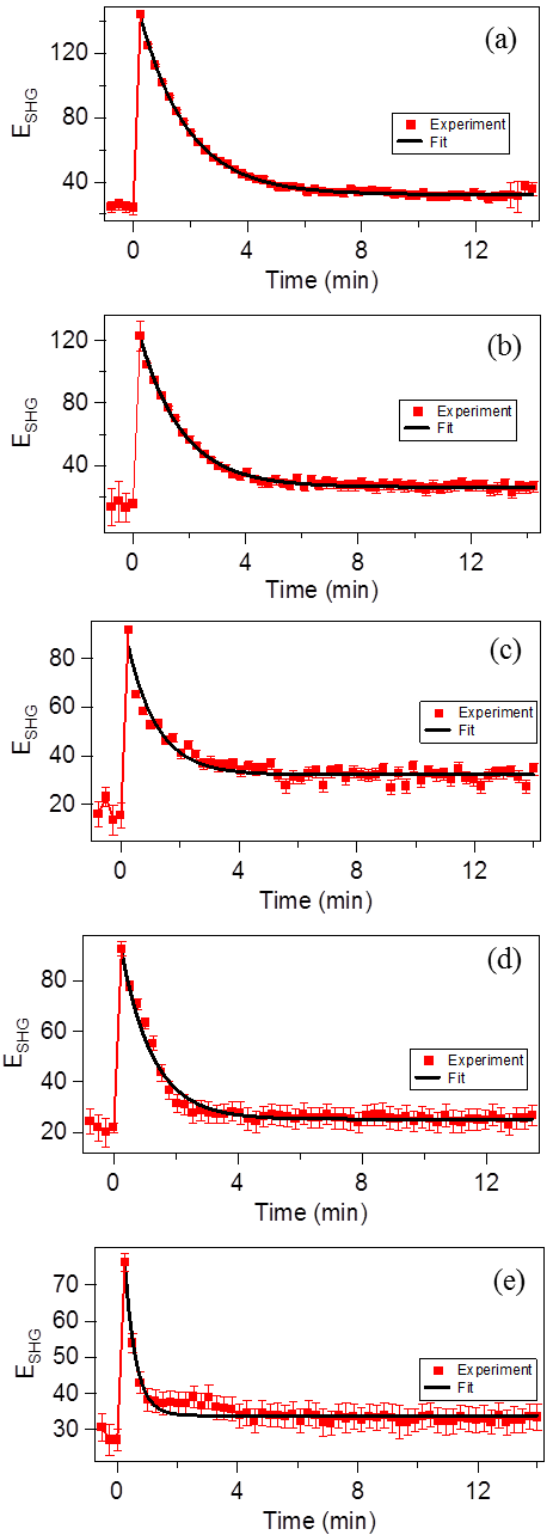

Figure 1.6. SHG electric field (red squares) as a function of reaction time of gold nanoparticles using (a) 25 µL, (b) 30 µL, (c) 35 µL, (d) 40 µL, and (e) 50 µL of precursor gold seeds, respectively, compared to the fits (black lines). [43]

Overall the gold nanoparticle *in situ* SHG and extinction spectroscopy results are consistent with a two-step growth process. During the first step of the nanoparticle growth reaction, rough and uneven surfaces are formed rapidly giving rise to plasmonic hot spots with corresponding broad, red-shifted plasmonic spectra. In the second step, the nanoparticle surface becomes more smooth, reaching a thermodynamic equilibrium. These results provide important information about the size-dependent nanoparticle reaction dynamics and the associated mechanisms, which cannot be obtained from traditional *ex-situ* techniques.

1.5 Scope of the Dissertation

This dissertation describes the use of nonlinear and ultrafast spectroscopic techniques for the investigations of real-time growth dynamics of gold-silver core-shell nanoparticles and the excited state relaxation dynamics of different nanomaterials. Chapter 2 describes research where nonlinear second harmonic generation and linear extinction spectroscopy is used to monitor the *in situ* growth dynamics of colloidal gold-silver core-shell nanoparticles. In Chapter 3, transient absorption spectroscopy is utilized as an advanced spectroscopic method to study the excited-state relaxation dynamics of porphyrin and zinc-porphyrin based nanomaterials. Porphyrin and zinc porphyrin dyes in water exhibit long-lived excited states on the order of several nanoseconds. However, these porphyrin excited-state lifetimes are significantly faster when in the nanoparticle environment due to energy transfer, enhanced intersystem crossing, and electronic delocalization. Finally, Chapter 4 describes research using ultrafast reflectivity as a spectroscopic tool to investigate the heating and melting dynamics of aluminum thin film samples under different powers and sample thicknesses as a part of the Consortium for

Innovation in Manufacturing and Materials (CIMM) collaboration. The ultrafast reflectivity results demonstrate that the dependence of heating and melting dynamics of aluminum thin film samples can be described by the two-temperature model with large changes in the melting threshold and electron-phonon coupling as the thin film thickness decreases below the heat penetration depth. Overall, the synthesis, characterization, nonlinear spectroscopy, and ultrafast spectroscopy of a wide variety of nanomaterials are studied in this thesis dissertation for the development of potential applications in nanomedicine, optoelectronics, molecular sensing, and laser-based additive manufacturing.

1.6 Notes

1. Mourdikoudis, S.; Pallares, R. M.; Thanh, N. T., Characterization Techniques for Nanoparticles: Comparison and Complementarity Upon Studying Nanoparticle Properties. *Nanoscale* **2018,** *10*, 12871-12934.

2. Burda, C.; Chen, X.; Narayanan, R.; El-Sayed, M. A., Chemistry and Properties of Nanocrystals of Fifferent Shapes. *Chem. Rev* **2005,** *105*, 1025-1102.

3. Jones, M. R.; Osberg, K. D.; Macfarlane, R. J.; Langille, M. R.; Mirkin, C. A., Templated Techniques for the Synthesis and Assembly of Plasmonic Nanostructures. *Chem. Rev* **2011,** *111*, 3736-3827.

4. Hartland, G. V., Optical Studies of Dynamics in Noble Metal Nanostructures. *Chem. Rev* **2011,** *111* (6), 3858-3887.

5. Hodak, J. H.; Martini, I.; Hartland, G. V., Spectroscopy and Dynamics of Nanometer-Sized Noble Metal Particles. *J. Phys. Chem. B* **1998,** *102*, 6958-6967.

6. Kamat, P. V., Meeting the Clean Energy Demand: Nanostructure Architectures for Solar Energy Conversion. *J. Phys. Chem . C* **2007,** *111*, 2834-2860.

7. Abeyweera, S. C.; Rasamani, K. D.; Sun, Y., Ternary Silver Halide Nanocrystals. *Acc. Chem. Res* **2017,** *50*, 1754-1761.

8. Kamat, P., Photophysical, Photochemical and Photocatalytic Aspects of Metal Nanoparticles. *J. Phys. Chem. B* **2002,** *106*, 7729-7744.

9. Haes, A. J.; Van Duyne, R. P., A Nanoscale Optical Biosensor: Sensitivity and Selectivity of an Approach Based on the Localized Surface Plasmon Resonance

Spectroscopy of Triangular Silver Nanoparticles. *J. Am. Chem. Soc* **2002,** *124*, 10596-10604.

10. El-Sayed, I. H.; Huang, X.; El-Sayed, M. A., Surface Plasmon Resonance Scattering and Absorption of Anti-EGFR Antibody Conjugated Gold Nanoparticles in Cancer Diagnostics: Applications in Oral Cancer. *Nano Lett.* **2005,** *5*, 829-834.

11. Prigodich, A. E.; Lee, O.-S.; Daniel, W. L.; Seferos, D. S.; Schatz, G. C.; Mirkin, C. A., Tailoring DNA Structure to Increase Target Hybridization Kinetics on Surfaces. *J. Am. Chem. Soc* **2010,** *132*, 10638-10641.

12. Nikoobakht, B.; Wang, J.; El-Sayed, M. A., Surface-Enhanced Raman Scattering of Molecules Adsorbed on Gold Nanorods: Off-Surface Plasmon Resonance Condition. *Chem. Phys. Lett* **2002,** *366*, 17-23.

13. Alvarez-Puebla, R.; Cui, B.; Bravo-Vasquez, J.-P.; Veres, T.; Fenniri, H., Nanoimprinted SERS-Active Substrates with Tunable Surface Plasmon Resonances. *J. Phys. Chem . C* **2007,** *111*, 6720-6723.

14. Nie, S.; Emory, S. R., Probing Single Molecules and Single Nanoparticles by Surface-Enhanced Raman Scattering. *Science* **1997,** *275*, 1102-1106.

15. Meyer, S. A.; Le Ru, E. C.; Etchegoin, P. G., Combining Surface Plasmon Resonance (SPR) Spectroscopy with Surface-Enhanced Raman Scattering (SERS). *Anal. Chem* **2011,** *83*, 2337-2344.

16. Ghosh Chaudhuri, R.; Paria, S., Core/Shell Nanoparticles: Classes, Properties, Synthesis Mechanisms, Characterization, and Applications. *Chem. Rev* **2011,** *112*, 2373-2433.

17. Liao, P.; Wokaun, A., Lightning Rod Effect in Surface Enhanced Raman Scattering. *J. Chem. Phys.* **1982,** *76*, 751-752.

18. Zarick, H. F.; Boulesbaa, A.; Talbert, E. M.; Puretzky, A.; Geohegan, D.; Bardhan, R., Ultrafast Excited-State Dynamics in Shape and Composition Controlled Gold–Silver Bimetallic Nanostructures. *J. Phys. Chem . C* **2017,** *121*, 4540-4547.

19. Lu, L.; Wang, H.; Zhou, Y.; Xi, S.; Zhang, H.; Hu, J.; Zhao, B., Seed-Mediated Growth of Large, Monodisperse Core–Shell Gold–Silver Nanoparticles with Ag-Like Optical Properties. *ChemComm* **2002,** 144-145.

20. Anandan, S.; Grieser, F.; Ashokkumar, M., Sonochemical Synthesis of Au− Ag Core− Shell Bimetallic Nanoparticles. *J. Phys. Chem . C* **2008,** *112*, 15102-15105.

21. Tsuji, M.; Miyamae, N.; Lim, S.; Kimura, K.; Zhang, X.; Hikino, S.; Nishio, M., Crystal Structures and Growth Mechanisms of Au@ Ag Core−Shell Nanoparticles Prepared by the Microwave−Polyol Method. *Cryst. Growth Des.* **2006,** *6*, 1801-1807.

22. Gonzalez, C. M.; Liu, Y.; Scaiano, J., Photochemical Strategies for the Facile Synthesis of Gold−Silver Alloy and Core−Shell Bimetallic Nanoparticles. *J. Phys. Chem . C* **2009,** *113*, 11861-11867.

23. Hsu, S.-W.; Rodarte, A. L.; Som, M.; Arya, G.; Tao, A. R., Colloidal Plasmonic Nanocomposites: From Fabrication to Optical Function. *Chem. Rev* **2018,** *118*, 3100-3120.

24. Cortie, M. B.; McDonagh, A. M., Synthesis and Optical Properties of Hybrid and Alloy Plasmonic Nanoparticles. *Chem. Rev* **2011,** *111*, 3713-3735.

25. Li, J.-F.; Zhang, Y.-J.; Ding, S.-Y.; Panneerselvam, R.; Tian, Z.-Q., Core–Shell Nanoparticle-Enhanced Raman Spectroscopy. *Chem. Rev* **2017,** *117*, 5002-5069.

26. Karam, T. E.; Smith, H. T.; Haber, L. H., Enhanced Photothermal Effects and Excited-State Dynamics of Plasmonic Size-Controlled Gold–Silver–Gold Core–Shell–Shell Nanoparticles. *J. Phys. Chem . C* **2015,** *119*, 18573-18580.

27. Kumal, R. R.; Abu-Laban, M.; Hamal, P.; Kruger, B.; Smith, H. T.; Hayes, D. J.; Haber, L. H., Near-Infrared Photothermal Release of siRNA from the Surface of Colloidal Gold–Silver–Gold Core–Shell–Shell Nanoparticles Studied with Second-Harmonic Generation. *J. Phys. Chem . C* **2018,** *122*, 19699-19704.

28. Devkota, T.; Chakraborty, D.; Yu, K.; Beane, G.; Sader, J. E.; Hartland, G. V., On the Measurement of Relaxation Times of Acoustic Vibrations in Metal Nanowires. *Phys. Chem. Chem. Phys.* **2018,** *20*, 17687-17693.

29. Beane, G.; Devkota, T.; Brown, B. S.; Hartland, G. V., Ultrafast Measurements of the Dynamics of Single Nanostructures: A Review. *Rep. Prog. Phys.* **2018,** *82*, 016401.

30. Yang, K.; Xu, H.; Cheng, L.; Sun, C.; Wang, J.; Liu, Z., In vitro and In Vivo Near-Infrared Photothermal Therapy of Cancer using Polypyrrole Organic Nanoparticles. *Adv. Mater.* **2012,** *24*, 5586-5592.

31. Petkau, K.; Kaeser, A.; Fischer, I.; Brunsveld, L.; Schenning, A. P., Pre and Postfunctionalized Self Assembled π-Conjugated Fluorescent Organic Nanoparticles for Dual Targeting. *J. Am. Chem. Soc* **2011,** *133*, 17063-17071.

32. Warner, I. M.; El-Zahab, B.; Siraj, N., Perspectives on Moving Ionic Liquid Chemistry into the Solid Phase. *Anal. Chem* **2014,** *86*, 7184-7191.

33. Jordan, A. N.; Das, S.; Siraj, N.; de Rooy, S. L.; Li, M.; El-Zahab, B.; Chandler, L.; Baker, G. A.; Warner, I. M., Anion-Controlled Morphologies and Spectral Features of Cyanine-Based NanoGUMBOS–An Improved Photosensitizer. *Nanoscale* **2012,** *4*, 5031-5038.

34. Bwambok, D. K.; El-Zahab, B.; Challa, S. K.; Li, M.; Chandler, L.; Baker, G. A.; Warner, I. M., Near-Infrared Fluorescent NanoGUMBOS for Biomedical Imaging. *ACS Nano* **2009,** *3*, 3854-3860.

35. Siraj, N.; Hasan, F.; Das, S.; Kiruri, L. W.; Steege Gall, K. E.; Baker, G. A.; Warner, I. M., Carbazole-Derived Group of Uniform Materials Based on Organic Salts: Solid State Fluorescent Analogues of Ionic Liquids for Potential Applications in Organic-Based Blue Light-Emitting Diodes. *J. Phys. Chem . C* **2014,** *118*, 2312-2320.

36. Karam, T. E.; Siraj, N.; Warner, I. M.; Haber, L. H., Anomalous Size-Dependent Excited-State Relaxation Dynamics of NanoGUMBOS. *J. Phys. Chem . C* **2015,** *119*, 28206-28213.

37. Karam, T. E.; Siraj, N.; Zhang, Z.; Ezzir, A. F.; Warner, I. M.; Haber, L. H., Ultrafast and Nonlinear Spectroscopy of Brilliant Green-Based NanoGUMBOS with Enhanced Near-Infrared Emission. *J. Chem. Phys.* **2017,** *147*, 144701.

38. Qiu, T.; Tien, C., Femtosecond Laser Heating of Multi-Layer Metals—I. Analysis. *Int. J. Heat Mass Transf.* **1994,** *37*, 2789-2797.

39. Majumdar, A.; Fushinobu, K.; Hijikata, K., Effect of Gate Voltage on Hot-Electron and Hot Phonon Interaction and Transport in a Submicrometer Transistor. *J. Appl. Phys.* **1995,** *77*, 6686-6694.

40. Gadzuk, J., ResonanceAassisted Hot Electron Femtochemistry at Surfaces. *Phys. Rev. Lett.* **1996,** *76*, 4234.

41. Wellershoff, S.-S.; Hohlfeld, J.; Güdde, J.; Matthias, E., The Role of Electron–Phonon Coupling in Femtosecond Laser Damage of Metals. *Appl. Phys. A* **1999,** *69*, S99-S107.

42. McPeak, K. M.; Jayanti, S. V.; Kress, S. J.; Meyer, S.; Iotti, S.; Rossinelli, A.; Norris, D. J., Plasmonic Films Can Easily Be Better: Rules and Recipes. *ACS Photonics* **2015,** *2*, 326-333.

43. McPeak, K. M.; Le, T. P.; Britton, N. G.; Nickolov, Z. S.; Elabd, Y. A.; Baxter, J. B., Chemical Bath Deposition of ZnO Nanowires at Near Neutral pH Conditions Without Hexamethylenetetramine (HMTA): Understanding the Role of HMTA in ZnO Nanowire Growth. *Langmuir* **2011,** *27*, 3672-3677.

44. Whiteside, P.; Chininis, J.; Hunt, H., Techniques and Challenges for Characterizing Metal Thin Films with Applications in Photonics. *Coatings* **2016,** *6*, 35.

45. Wang, Q.; Morrow, J. D.; Ma, C.; Duffie, N. A.; Pfefferkorn, F. E., Surface Prediction Model for Thermocapillary Regime Pulsed Laser Micro Polishing of Metals. *J. Manuf. Process* **2015,** *20*, 340-348.

46. Oh, H.; Lee, J.; Seo, M.; Baek, I. U.; Byun, J. Y.; Lee, M., Laser-Induced Dewetting of Metal Thin Films for Template-Free Plasmonic Color Printing. *ACS Appl. Mater. Interfaces* **2018,** *10*, 38368-38375.

47. Yoneda, H.; Morikami, H.; Ueda, K.-i.; More, R. M., Ultrashort-Pulse Laser Ellipsometric Pump-Probe Experiments on Gold Targets. *Phys. Rev. Lett.* **2003,** *91*, 075004.

48. Rapp, S.; Kaiser, M.; Schmidt, M.; Huber, H. P., Ultrafast Pump-Probe Ellipsometry Setup for the Measurement of Transient Optical Properties During Laser Ablation. *Opt. Express* **2016,** *24*, 17572-17592.

49. Norris, P. M.; Caffrey, A. P.; Stevens, R. J.; Klopf, J. M.; McLeskey Jr, J. T.; Smith, A. N., Femtosecond Pump–Probe Nondestructive Examination of Materials. *Rev. Sci. Instrum.* **2003,** *74*, 400-406.

50. Sabbah, A.; Riffe, D. M., Femtosecond Pump-Probe Reflectivity Study of Silicon Carrier Dynamics. *Phys. Rev. B* **2002,** *66*, 165217.

51. Kumal, R. R.; Nguyenhuu, H.; Winter, J. E.; McCarley, R. L.; Haber, L. H., Impacts of Salt, Buffer, and Lipid Nature on Molecular Adsorption and Transport in Liposomes as Observed by Second Harmonic Generation. *J. Phys. Chem . C* **2017,** *121*, 15851-15860.

52. Fearon, A. D.; Stokes, G. Y., Thermodynamics of Indomethacin Adsorption to Phospholipid Membranes. *J. Phys. Chem. B* **2017,** *121*, 10508-10518.

53. Liu, J.; Subir, M.; Nguyen, K.; Eisenthal, K. B., Second Harmonic Studies of Ions Crossing Liposome Membranes in Real Time. *J. Phys. Chem. B* **2008,** *112*, 15263-15266.

54. Turkpence, D.; Akguc, G. B.; Bek, A.; Tasgin, M. E., Engineering Nonlinear Response of Nanomaterials Using Fano Resonances. *J. Opt* **2014,** *16*, 105009.

55. Ray, P. C., Size and Shape Dependent Second Order Nonlinear Optical Properties of Nanomaterials and Their Application in Biological and Chemical Sensing. *Chem. Rev* **2010,** *110*, 5332-5365.

56. Dominguez-Juarez, J. L.; Kozyreff, G.; Martorell, J., Whispering Gallery Microresonators for Second Harmonic Light Generation from a Low Number of Small Molecules. *Nat. Commun* **2011,** *2*, 254.

57. Örtegren, J.; Wantke, K.-D.; Motschmann, H.; Möhwald, H., A Study of Kinetic Molecular Exchange Processes in the Medium Frequency Range by Surface SHG on an Oscillating Bubble. *J. Colloid Interface Sci* **2004,** *279*, 266-276.

58. Darlington, A. M.; Gibbs-Davis, J. M., Bimodal or Trimodal? The Influence of Starting pH on Site Identity and Distribution at the Low Salt Aqueous/Silica Interface. *J. Phys. Chem . C* **2015,** *119*, 16560-16567.

59. Kumal, R. R.; Karam, T. E.; Haber, L. H., Determination of the Surface Charge Density of Colloidal Gold Nanoparticles Using Second Harmonic Generation. *J. Phys. Chem . C* **2015,** *119*, 16200-16207.

60. Roke, S.; Gonella, G., Nonlinear Light Scattering and Spectroscopy of Particles and Droplets in Liquids. *Annu. Rev. Phys. Chem* **2012,** *63*, 353-378.

61. Hou, Y.; Chen, S.-L.; Gan, W.; Ma, X.; Yuan, Q., Understanding the Dynamic Behavior of an Anti-cancer Drug-Doxorubicin on a Lipid Membrane Using Multiple Spectroscopic Techniques. *J. Phys. Chem. B* **2019,** *123*, 3756−3762.

62. Hamal, P.; Nguyenhuu, H.; Subasinghege Don, V.; Kumal, R. R.; Kumar, R.; McCarley, R. L.; Haber, L. H., Molecular Adsorption and Transport at Liposome Surfaces Studied by Molecular Dynamics Simulations and Second Harmonic Generation Spectroscopy. *J. Phys. Chem. B* **2019,** *123,* 7722-7730.

63. Doughty, B.; Ma, Y.-Z.; Shaw, R. W., Probing Interfacial Electronic States in CdSe Quantum Dots Using Second Harmonic Generation Spectroscopy. *J. Phys. Chem . C* **2015,** *119*, 2752-2760.

64. Doughty, B.; Rao, Y.; Kazer, S. W.; Kwok, S. J.; Turro, N. J.; Eisenthal, K. B., Binding of the Anti-Cancer Drug Daunomycin to DNA Probed by Second Harmonic generation. *J. Phys. Chem. B* **2013,** *117*, 15285-15289.

65. Khoury, R. A.; Ranasinghe, J. C.; Dikkumbura, A. S.; Hamal, P.; Kumal, R. R.; Karam, T. E.; Smith, H. T.; Haber, L. H., Monitoring the Seed-Mediated Growth of Gold Nanoparticles Using in Situ Second Harmonic Generation and Extinction Spectroscopy. *J. Phys. Chem . C* **2018,** *122*, 24400-24406.

66. Sauerbeck, C.; Haderlein, M.; Schürer, B.; Braunschweig, B. r.; Peukert, W.; Klupp Taylor, R. N., Shedding Light on the Growth of Gold Nanoshells. *ACS Nano* **2014,** *8*, 3088-3096.

67. Butet, J.; Brevet, P.-F.; Martin, O. J., Optical Second Harmonic Generation in Plasmonic Nanostructures: From Fundamental Principles to Advanced Applications. *ACS Nano* **2015,** *9*, 10545-10562.

68. Thyagarajan, K.; Rivier, S.; Lovera, A.; Martin, O. J., Enhanced Second Harmonic Generation from Double Resonant Plasmonic Antennae. *Opt. Express* **2012,** *20*, 12860-12865.

69. Zhang, J.; Averitt, R., Dynamics and Control in Complex Transition Metal Oxides. *Annu. Rev. Mater. Res.* **2014,** *44*, 19-43.

70. Berera, R.; van Grondelle, R.; Kennis, J. T., Ultrafast Transient Absorption Spectroscopy: Principles and Application to Photosynthetic Systems. *Photosynth. Res.* **2009,** *101*, 105-118.

71. Knowles, K. E.; Koch, M. D.; Shelton, J. L., Three Applications of Ultrafast Transient Absorption Spectroscopy of Semiconductor Thin Films: Spectroelectrochemistry, Microscopy, and Identification of Thermal Contributions. *J. Mater. Chem. C* **2018,** *6*, 11853-11867.

72. Link, S.; El-Sayed, M. A., Spectral Properties and Relaxation Dynamics of Surface Plasmon Electronic Oscillations in Gold and Silver Nanodots and Nanorods. *J. Phys. Chem. B* **1999,** *103*, 8410-8426.

73. Ohkita, H.; Cook, S.; Astuti, Y.; Duffy, W.; Tierney, S.; Zhang, W.; Heeney, M.; McCulloch, I.; Nelson, J.; Bradley, D. D., Charge Carrier Formation in Polythiophene/Fullerene Blend Films Studied by Transient Absorption Spectroscopy. *J. Am. Chem. Soc* **2008,** *130*, 3030-3042.

74. Karam, T. E.; Khoury, R. A.; Haber, L. H., Excited-State Dynamics of Size-Dependent Colloidal TiO2-Au Nanocomposites. *J. Chem. Phys.* **2016,** *144*, 124704.

75. Farm, W.; Storz, R.; Tom, H.; Bokor, J., Direct Measurement of Nonequilibrium Electron-Energy Distributions in Sub-Picosecond Laser-Heated Gold Films. *Surf. Sci.* **1993,** *283*, 221-225.

76. Domke, M.; Nobile, L.; Rapp, S.; Eiselen, S.; Sotrop, J.; Huber, H. P.; Schmidt, M., Understanding Thin Film Laser Ablation: The Role of the Effective Penetration Depth and the Film Thickness. *Phys. Procedia* **2014,** *56*, 1007-1014.

77. Kandyla, M.; Shih, T.; Mazur, E., Femtosecond Dynamics of the Laser-Induced Solid-to-Liquid Phase Transition in Aluminum. *Phys. Rev. B* **2007,** *75*, 214107.

78. Bonse, J.; Bachelier, G.; Siegel, J.; Solis, J., Time and Space Resolved Dynamics of Melting, Ablation, and Solidification Phenomena Induced by Femtosecond Laser Pulses in Germanium. *Phys. Rev. B* **2006,** *74*, 134106.

79. He, X.; Punpongjareorn, N.; Wu, C.; Davydov, I. A.; Yang, D.-S., Ultrafast Carrier Dynamics of CdTe: Surface Effects. *J. Phys. Chem . C* **2016,** *120*, 9350-9356.

80. Hopkins, P. E.; Norris, P. M., Contribution of Ballistic Electron Transport to Energy Transfer During Electron-Phonon Nonequilibrium in Thin Metal Films. *J. Heat. Transfer* **2009,** *131*, 043208.

81. Xu, X.; Yang, F.; Li, X.; Gao, Y., Non-Equilibrium Heat Transport of Copper-Silver Alloy Films by Femtosecond Laser with Double Pump Beams. *Optik* **2019,** *176*, 114-118.

82. Fann, W.; Storz, R.; Tom, H.; Bokor, J., Electron Thermalization in Gold. *Phys. Rev. B* **1992,** *46*, 13592.

83. Sun, C.-K.; Vallée, F.; Acioli, L.; Ippen, E.; Fujimoto, J., Femtosecond-Tunable Measurement of Electron Thermalization in Gold. *Phys. Rev. B* **1994,** *50*, 15337.

84. Wang, B.; Gallais, L., A Theoretical Investigation of the Laser Damage Threshold of Metal Multi-Dielectric Mirrors for High Power Ultrashort Applications. *Opt. Express* **2013,** *21*, 14698-14711.

85. Abécassis, B.; Testard, F.; Spalla, O.; Barboux, P., Probing In Situ the Nucleation and Growth of Gold Nanoparticles by Small-Angle X-ray Scattering. *Nano Lett.* **2007,** *7*, 1723-1727.

86. Polte, J.; Herder, M.; Erler, R.; Rolf, S.; Fischer, A.; Würth, C.; Thünemann, A. F.; Kraehnert, R.; Emmerling, F., Mechanistic Insights into Seeded Growth Processes of Gold Nanoparticles. *Nanoscale* **2010,** *2*, 2463-2469.

87. Polte, J. r.; Ahner, T. T.; Delissen, F.; Sokolov, S.; Emmerling, F.; Thünemann, A. F.; Kraehnert, R., Mechanism of Gold Nanoparticle Formation in the Classical Citrate Synthesis Method Derived from Coupled In Situ XANES and SAXS Evaluation. *J. Am. Chem. Soc* **2010,** *132*, 1296-1301.

88. Eisenthal, K. B., Second Harmonic Spectroscopy of Aqueous Nano and Microparticle Interfaces. *Chem. Rev* **2006,** *106*, 1462-1477.

89. Dadap, J. I.; Shan, J.; Eisenthal, K. B.; Heinz, T. F., Second Harmonic Rayleigh Scattering from a Sphere of Centrosymmetric Material. *Phys. Rev. Lett.* **1999,** *83*, 4045.

Chapter 2. Monitoring the Growth Dynamics of Colloidal Gold-Silver Core-Shell Nanoparticles Using *in Situ* Second Harmonic Generation and Extinction Spectroscopy

2.1 Introduction

The study of plasmonic nanoparticles is a field of intense research due to their potential applications in nanomedicine, photothermal therapy, molecular sensing, catalysis, and photovoltaics.[1-14] Gold and silver nanoparticles have localized surface plasmon resonances (LSPRs) which are characterized by the coherent oscillations of free electrons at the nanoparticle surface caused by incident illumination, leading to enhanced optical absorption and scattering processes.[15] Bimetallic nanoparticles in core-shell configurations have emerged as a new class of plasmonic nanoparticles due to the improved optoelectronic tunability by adjusting their overall size, shape, and composition, as well as their individual core and shell sizes.[16-18] Core-shell architectures composed of gold and silver are especially attractive for nanomedicine, photothermal therapy, and noninvasive bioimaging as a consequence of their biocompatibility and large plasmonic response.[12, 19-21] For further development of core-shell nanoparticle applications, a detailed understanding of the mechanisms and kinetics of nanoparticle shell formation is needed, which can help provide new approaches in tailoring the chemical, structural, and plasmonic properties for the desired nanomaterial technologies.

Several methods have been developed for the synthesis of gold-silver core-shell nanoparticles including procedures that rely on chemical,[12, 22-25] microwave-assisted,[26] photochemical,[27, 28] and sonochemical routes.[29] In chemical synthesis strategies, Ag^+ is typically reduced on the surface of a colloidal core gold nanoparticle for independent control of both the gold core size as well as the silver shell thickness. The usage of a mild

reducing agent, such as ascorbic acid (AA), facilitates the reduction of Ag^+ selectively onto the colloidal gold nanoparticle surface while preventing the formation of free silver nanoparticles.[12, 18] Analytical techniques such as transmission electron microscopy (TEM), scanning electron microscopy, atomic force microscopy, dynamic light scattering, and extinction spectroscopy are important tools for the *ex situ* characterization of core-shell nanoparticles after the synthesis is complete.[8, 12, 13, 17, 30]

In order to investigate the growth dynamics of nanomaterials in real time, *in situ* characterization techniques have been developed that perform time-dependent measurements as the nanoparticle formation occurs under varying reaction conditions. For example, the nucleation and growth of silver nanoparticles in aqueous solution was studied under varying electron beam currents using *in situ* scanning transmission electron microscopy.[31] Additionally, *in situ* TEM was used to investigate different pathways of silver shell growth around a cubic gold nanoparticle core in aqueous solution using the reducing agent AA with different capping agent concentrations.[32] The nucleation and growth of silver nanoparticles by sodium borohydride reduction in water was studied using *in situ* extinction spectroscopy combined with *in situ* small angle X-ray scattering.[33] The formation of gold nanoshells onto silica nanoparticles were investigated using *in situ* extinction spectroscopy combined with *in situ* second harmonic scattering measurements.[34] In our recent work, we studied the seed-mediated growth dynamics of colloidal gold nanoparticles under chemical reduction using *in situ* second harmonic generation (SHG) and *in situ* extinction spectroscopy.[35] These different *in situ* techniques provide key insights into nanoparticle synthesis reactions and core-shell growth processes, leading to improved nanoscale engineering.

Second harmonic generation is a surface-sensitive nonlinear optical technique in which two photons of frequency ω interact coherently to generate a photon with twice the frequency at 2ω.[36-41] For centrosymmetric materials and bulk solutions, SHG only occurs at an interface where the inversion symmetry is broken. Therefore, SHG spectroscopy is a powerful method for investigating the colloidal nanoparticle surface and the corresponding surface chemistry during *in situ* nanoparticle growth reactions. The SHG electric field E_{SHG} originates from the second-order and third-order nonlinear susceptibilities, $\chi^{(2)}$ and $\chi^{(3)}$, respectively, with

$$E_{SHG} = \sqrt{I_{SHG}} = \chi^{(2)} E_\omega E_\omega + \chi^{(3)} E_\omega E_\omega \phi_0 \qquad 2.1$$

where E_ω is the incident optical electric field at frequency ω, ϕ_0 is the electrostatic potential at the nanoparticle surface, and I_{SHG} is the SHG intensity.[4, 36-38] The $\chi^{(2)}$ term for SHG is due to the two-photon resonant and non-resonant spectroscopy of the sample, while the $\chi^{(3)}$ term for SHG arises from the nanoparticle electrostatic surface potential causing a net polarization of the bulk solvent. Previous work on SHG has investigated a large variety of samples including biological interfaces,[42-45] interfacial acid-base chemistry,[46] surface potential measurements,[4, 47] TiO_2 microparticles,[48] and metallic, plasmonic nanoparticles composed of gold, silver, and gold-silver alloys.[49-55] Our recent study of seed-mediated growth dynamics of colloidal gold nanoparticles using *in situ* SHG spectroscopy demonstrated a size-dependent nanoparticle growth lifetime which is dominated by plasmonic hot spots and a surface morphology that becomes more smooth and uniform as a function of reaction time.[35]

In this chapter, *in situ* SHG combined with *in situ* extinction spectroscopy is used to study the growth dynamics of colloidal gold-silver core-shell nanoparticles. The silver

shells are grown by reduction of Ag^+ onto 14 nm gold seed nanoparticles using AA in water under three different reaction concentrations to produce Au@Ag nanoparticles of final sizes ranging from 51 to 78 nm in diameter. The time-dependent SHG signals and extinction spectra are analyzed to elucidate the mechanisms of the silver shell growth process and to determine the characteristic nanoparticle growth lifetimes as a function of the shell thickness. The extinction spectroscopy results show that the nanoparticle growth lifetime increases as the shell thickness increases. Additionally, the *in situ* SHG time traces exhibit biexponential behavior where faster lifetimes are in excellent agreement with the lifetimes obtained from the extinction measurements and the slower lifetimes are attributed to additional surface reactions that change the nanoparticle surface charge densities. The *in situ* results also display large SHG enhancements at early stages in the shell growth process caused by plasmonic hot spots from rough, uneven nanoparticle surfaces that become more smooth and uniform as the reaction proceeds. The final extinction spectra are compared to FDTD calculations, showing general agreement, with the plasmon peak red shifting and increasing in spectral width as the silver shell thickness increases. The *in situ* SHG and extinction spectroscopy measurements provides valuable information regarding colloidal nanoparticle core-shell growth processes for developing controlled plasmon-enhanced nanomaterial technologies.

2.2 Experimental Section

2.2.1 Synthesis of Gold-Silver Core-Shell Nanoparticles

The gold-silver core-shell nanoparticles are prepared following a modified procedure which has been described previously.[8, 12] Gold chloride, sodium citrate, silver nitrate, L-ascorbic acid, potassium iodide, and sodium hydroxide are purchased from Sigma Aldrich and used without further purification. The gold seed nanoparticles are first synthesized by adding 900 µL of 34 mM sodium citrate to 30 mL of 290 µM gold chloride in ultrapure water under boiling conditions with vigorous stirring.[6, 56, 57] The solution undergoes a color change from pale yellow to bright red after 10 min, resulting in the formation of 13.8 ± 1.0 nm gold seed nanoparticles, as described in greater detail in the Appendix A. Gold-silver core-shell nanoparticles are prepared by reducing Ag^+ onto the gold seed nanoparticles in solution using ultrapure water under three different seed concentrations.[58] A volume of 17.5, 22.5, or 27.5 *µ*L of the prepared gold seed nanoparticle solution is added to an aqueous solution of 0.15 mM $AgNO_3$ and 0.30 *µ*M of KI in a total volume of 2.5 mL. These constitute the three different reaction conditions which result in the three different final gold-silver core-shell nanoparticle samples. A rapid addition of 5.0 *µ*L of 100 mM ascorbic acid and 6.25 *µ*L of 100 mM NaOH initiates the silver shell growth at the colloidal surface of the gold seed nanoparticles. These three gold-silver core-shell nanoparticle reactions are all performed in a quartz cuvette under constant stirring while being monitored spectroscopically by *in situ* SHG and extinction spectroscopy, as described below.

2.2.2 *In Situ* Second Harmonic Generation and Extinction Spectroscopy Setup

The experimental setup for *in situ* SHG spectroscopy consists of an ultrafast laser system, an optical setup, and a high-sensitivity charge-coupled device (CCD) spectroscopy detector connected to monochromator spectrograph, as described previously.[4, 6, 35] The output beam from a titanium:sapphire laser system with 2.7 W average power and 75 fs pulses centered at 800 nm at a repetition rate of 80 MHz is attenuated to 600 mW using a neutral density filter and is focused into a 1 cm by 1 cm quartz cuvette containing the colloidal nanoparticle sample under investigation. Optical filters are used to remove any residual SHG signal from the laser beam before the sample and to remove the fundamental 800 nm light after the sample while transmitting the SHG, which is collected in the forward direction and refocused into spectroscopy detector. Additionally, a low-intensity broadband tungsten filament lamp is placed orthogonal to the path of the laser beam, collimated using a pair of lenses and focused into the quartz cuvette, using a fiber-optic spectrometer detector for the *in situ* extinction spectroscopy. For each trial, the gold seeds, $AgNO_3$, and KI are added in ultrapure water for baseline measurements prior to the addition of AA and NaOH, which initialize the reaction at time zero. A home-built data acquisition program collects 6 *in situ* SHG spectra and 6 background spectra using a computer-controlled beam block, followed by 10 *in situ* extinction spectra, in repeating iterations for time-dependent SHG and extinction spectroscopy with statistical analysis. The SHG acquisition times are 0.2 s for the first 50 s, followed by 1 s for the remainder of each reaction, and the extinction acquisition times are 0.5 s. A schematic diagram of the *in situ* SHG and extinction spectroscopy setup is shown in the Appendix A.

2.2.3 Finite-Difference Time-Domain Calculations

The extinction spectra of single gold-silver core-shell nanoparticles of various sizes in water are calculated using a classical finite-difference time-domain (FDTD) approach, as described previously,[59] in collaboration with Dr. Lopata's research group at LSU. The FDTD approach provides solutions to Maxwell's equations for the plasmonic nanoparticle using discretized grids in space and time with spatial- and frequency-dependent permittivity and permeability fit to the bulk experimental values.[59-61] For each calculation, the grid space is 20 au = 1.06 nm and the time step was chosen to be 0.067 au = 1.62×10^{-3} fs such that the Courant-Friedrichs-Lewy stability condition equals to 0.8. The total running time is set as 1500 au = 36.3 fs. The FDTD calculated extinction spectra allow for interpreting the observed experimental spectra features, as well as confirming the nanoparticle geometries. See the Appendix A for more details.

2.3 Results and Discussion

After each gold-silver core-shell nanoparticle synthesis, the final nanoparticle size distribution is characterized by transmission electron microscopy using a survey of more than 200 nanoparticles for each sample. The resulting nanoparticle size histograms are fitted using log-normal distributions for each core-shell nanoparticle sample, as shown in the Appendix A. Figure 2.1 shows representative TEM images for the core-shell nanoparticle samples prepared using 27.5, 22.5, and 17.5 µL of precursor gold seeds, resulting in final sizes of, 51.0 ± 7.1, 65.8 ± 9.2, and 77.6 ± 8.6 nm, respectively, shown in order of increasing nanoparticle size. All gold-silver core-shell nanoparticles are observed to be relatively monodisperse and spherical in shape. By decreasing the amount of gold nanoparticles seeds added to the reaction, more Ag^+ is available per seed,

resulting in larger silver shell thicknesses after the reaction is complete, in an analogous manner to previous work on seed-mediated gold nanoparticles.[35, 56]

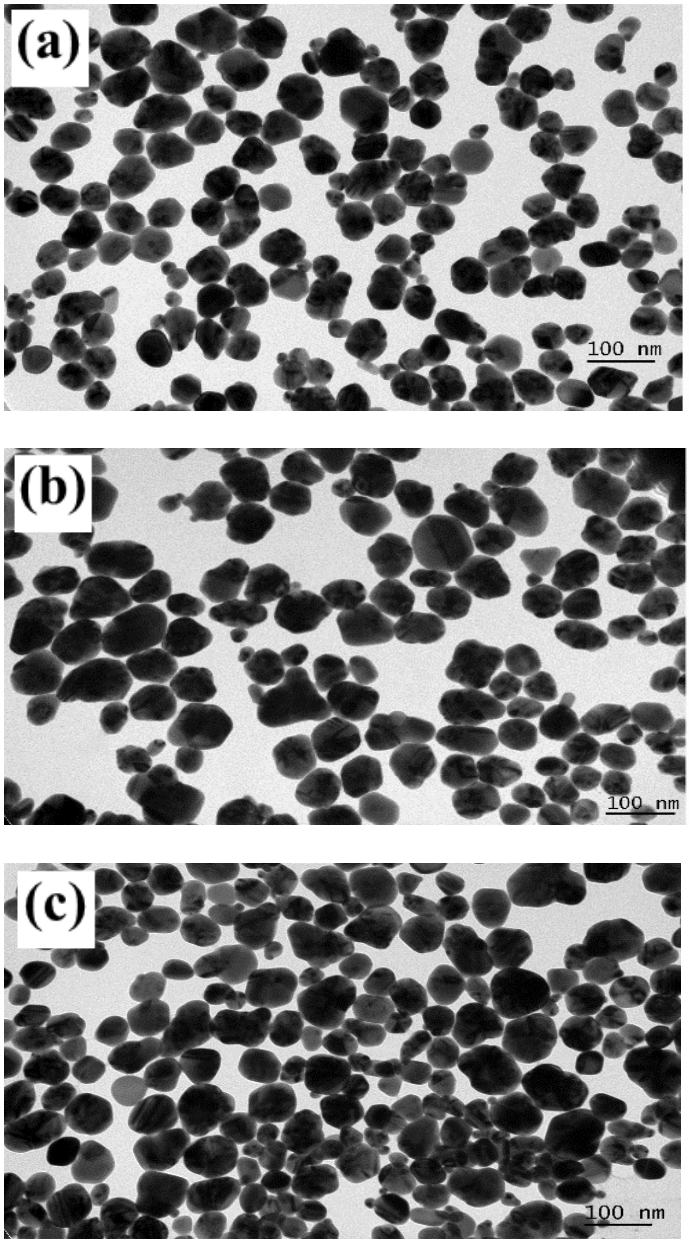

Figure 2.1. Representative TEM images of gold-silver core-shell nanoparticles with average sizes of (a) 51.1 ± 7.1, (b) 65.8 ± 9.2, and (c) 77.7 ± 8.6 nm, prepared using 27.5, 22.5, and 17.5 μL of precursor gold seeds, respectively. All Au@Ag nanoparticles have a gold core of diameter 13.8 ± 1.0 nm.

The growth dynamics of each colloidal core-shell nanoparticle sample are monitored in real time by both *in situ* extinction spectroscopy and *in situ* SHG measurements. Representative extinction spectra for the gold-silver core-shell nanoparticle samples using 27.5, 22.5, and 17.5 µL of added gold precursor seeds at different reactions times are shown in Figure 2.2. The initial extinction spectra correspond to the sample of gold seeds together with the $AgNO_3$ and KI before to the addition of AA and NaOH.[54, 62] Immediately, after the addition of the reducing agent AA, a broad plasmonic peak centered near 420 nm is observed. As the nanoparticle reaction continues in time, the plasmonic peak rapidly increases in intensity, while slightly blue shifting and narrowing in spectral width. After approximately 20 s, all the gold-silver core-shell nanoparticle samples reach a stable configuration, and the extinction spectra are observed to remain constant over the rest of the *in situ* extinction measurements. The peak wavelengths of the final extinction spectra are 419 nm, 424 nm, and 428 nm for the 51 nm, 66 nm, and 78 nm Au@Ag samples, respectively, demonstrating a trend of a red-shifting plasmon peak as the silver shell increases in thickness. The full width at half maxima (FWHM) obtained from these final extinction spectra are 111 nm, 135 nm, and 150 nm for the 51 nm, 66 nm, and 78 nm Au@Ag samples, respectively, showing a trend of increasing spectral width as the silver shell thickness increases.

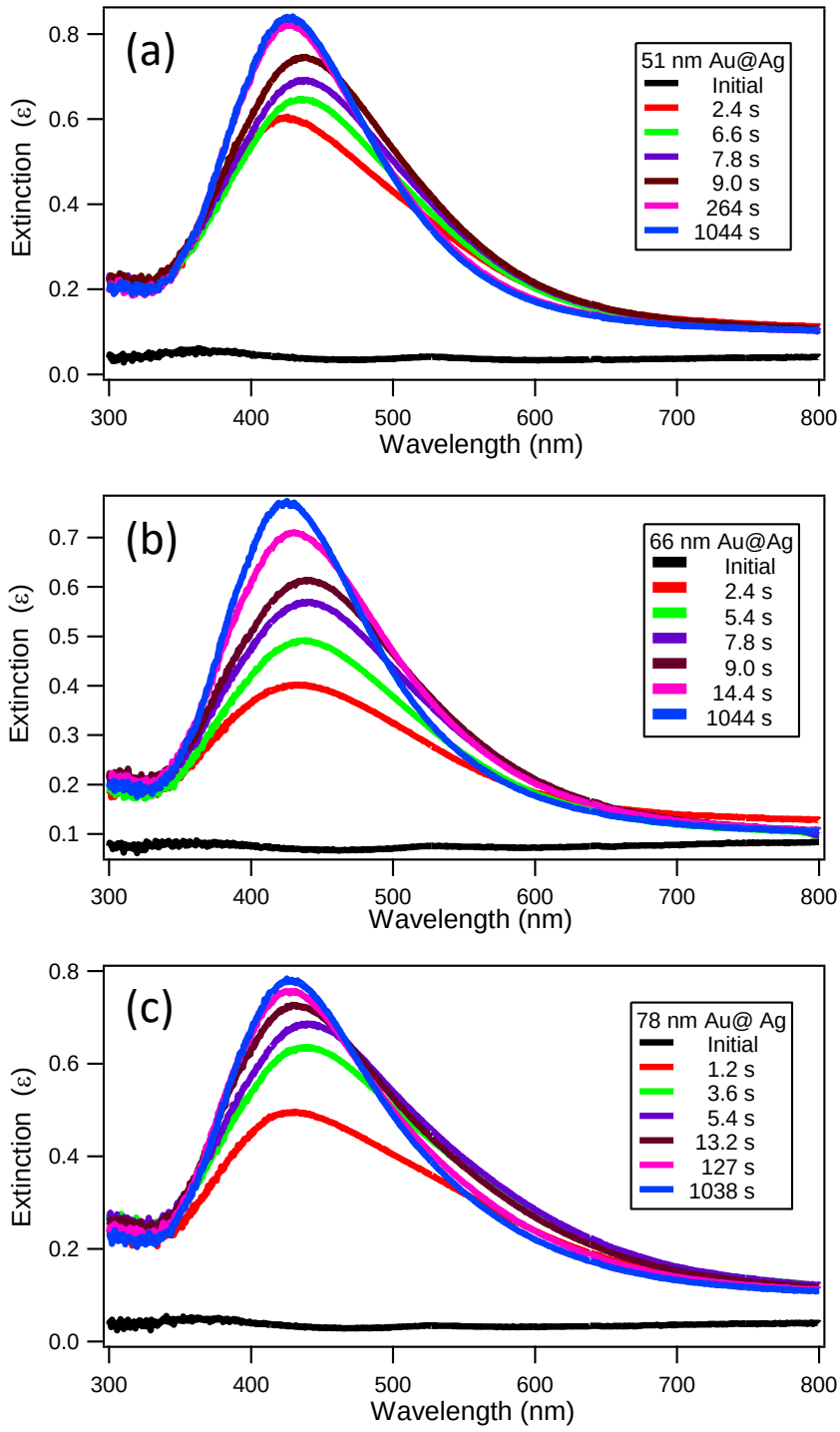

Figure 2.2. *In situ* extinction spectra of gold-silver core-shell nanoparticles synthesized using (a) 27.5, (b) 22.5, and (c) 17.5 μL of precursor gold seeds, respectively, at different times during the reactions. All Au@Ag nanoparticles have a gold core of diameter 13.8 nm.

To better characterize the *in situ* extinction spectroscopy of the nanoparticle reaction dynamics, the extinction peak intensities are fit as a function of time for each core-shell nanoparticle sample. The extinction peak time traces are fit using an exponential function given by the equation $\varepsilon(t) = A\, e^{-t/\tau_{ext}} + B$, where t is the reaction time after addition of the reducing agent, τ_{ext} is the extinction growth lifetime, A is the amplitude, and B is the offset extinction value. The corresponding fits for each core-shell nanoparticle sample are shown in Figure 2.3 and the fitting parameters are tabulated in the Appendix A. The extinction growth lifetime increases as the final nanoparticle diameter increases with values of 5.2 ± 0.2 s, 5.3 ± 0.2 s, and 6.2 ± 0.1 s for the 51.0 nm, 65.8 nm, and 77.7 nm gold-silver core-shell nanoparticles, respectively. All Au@Ag nanoparticle samples investigated here have a 13.8 nm gold core, as determined by TEM measurements. These lifetimes can be best understood as the time it takes for the silver shells to grow around the gold seed nanoparticles to form the final gold-silver core-shell nanoparticle architectures. After the colloidal core-shell nanoparticle structures are formed according to these characteristic extinction growth lifetimes, the extinction spectra and intensities remain constant for the entire duration of the experiment, as shown in the insets of Figure 2.3. These constant extinction spectra after the nanoparticle growth dynamics are complete indicate that the final core-shell nanoparticles remain very stable in colloidal suspension. Subsequent extinction spectroscopy measurements show that these core-shell nanoparticles are stable for at least several days in aqueous colloidal suspension after the nanoparticle synthesis is complete.

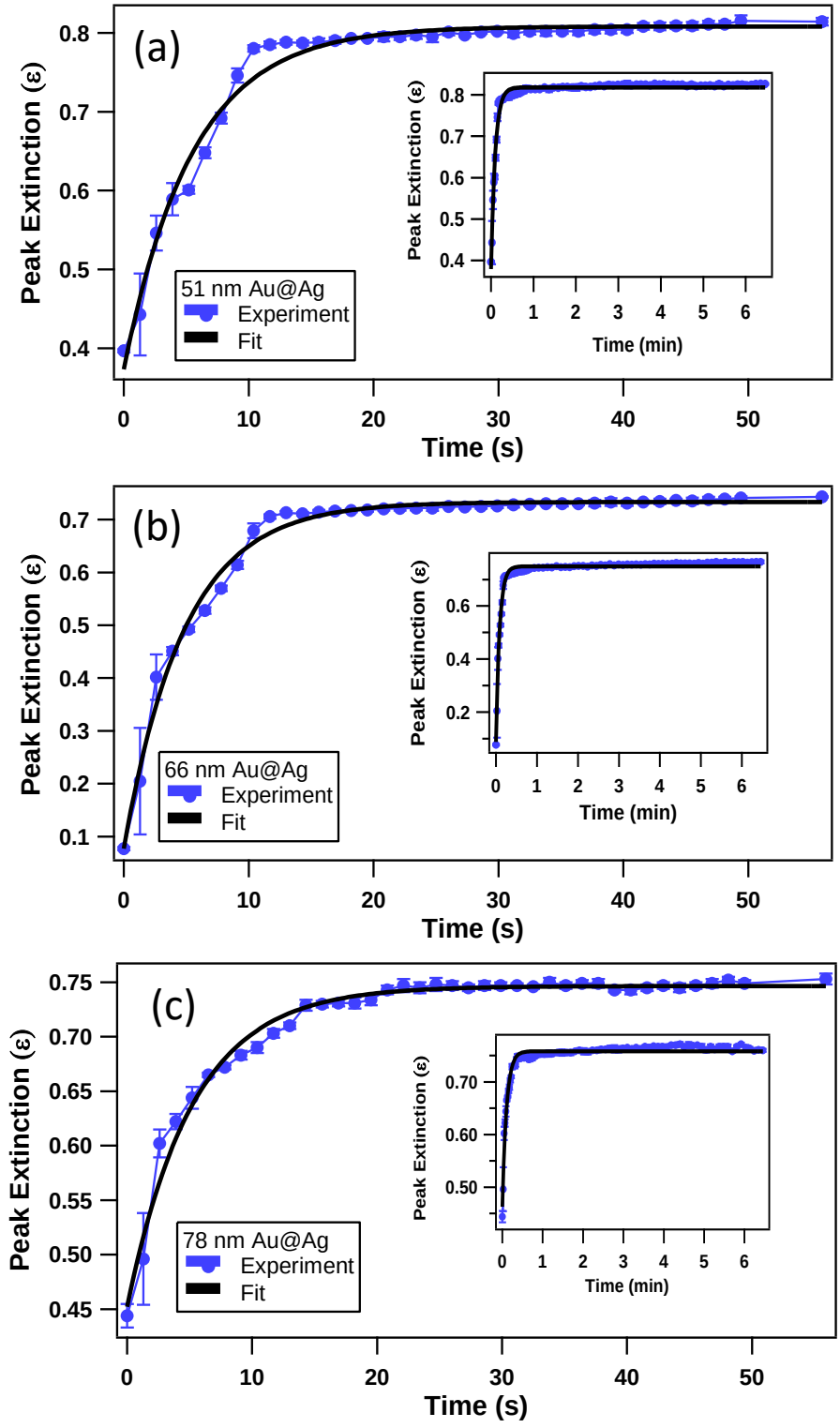

Figure 2.3. Peak extinctions (blue circles) as a function of time for gold-silver core-shell nanoparticles using (a) 27.5, (b) 22.5, and (c) 17.5 μL of precursor gold seeds, respectively, compared to the fits (black lines).

For additional analysis, the final extinction spectrum of each gold-silver core-shell nanoparticle sample is directly compared to the corresponding spectra generated using FDTD calculations. The extinction spectra for 9 different gold-silver core-shell nanoparticle sizes are calculating using FDTD, where each Au@Ag nanoparticle has a spherical gold core of diameter 13.8 nm and different spherical silver shell thicknesses. The 9 different silver shell thicknesses used for these calculations are 12.0, 13.7, 18.6, 23.0, 27.0, 29.0, 32.0, 35.0, and 37.0 nm, which result in total core-shell diameters ranging from 37.8 nm to 87.8 nm, respectively. Additional details and results regarding the FDTD calculations of the gold-silver core-shell nanoparticle extinction spectra are provided in the Appendix A. The experimental extinction spectra are first compared to the normalized calculated spectra for single core-shell nanoparticles, using shell thicknesses of 18.6 nm, 27 nm, and 32 nm, to closely match the average sizes of the corresponding Au@Ag nanoparticles, respectively. The blue curves in Figure 2.4 show the computed FDTD spectra for these nanoparticle geometries. In general, the spectra show trends of increasing peak intensities, red-shifted peak wavelengths, and increasing full widths at half maximum as the silver shell thickness increases, in general agreement with the experimental results. These calculated spectra from single Au@Ag nanoparticles have peak wavelengths of 410 nm, 424 nm, and 449 nm respectively, showing general agreement with the experimental results; however, the experimental extinction spectra show greater spectral widths and a lower degree of spectral red shifting than the single nanoparticle calculated spectra.

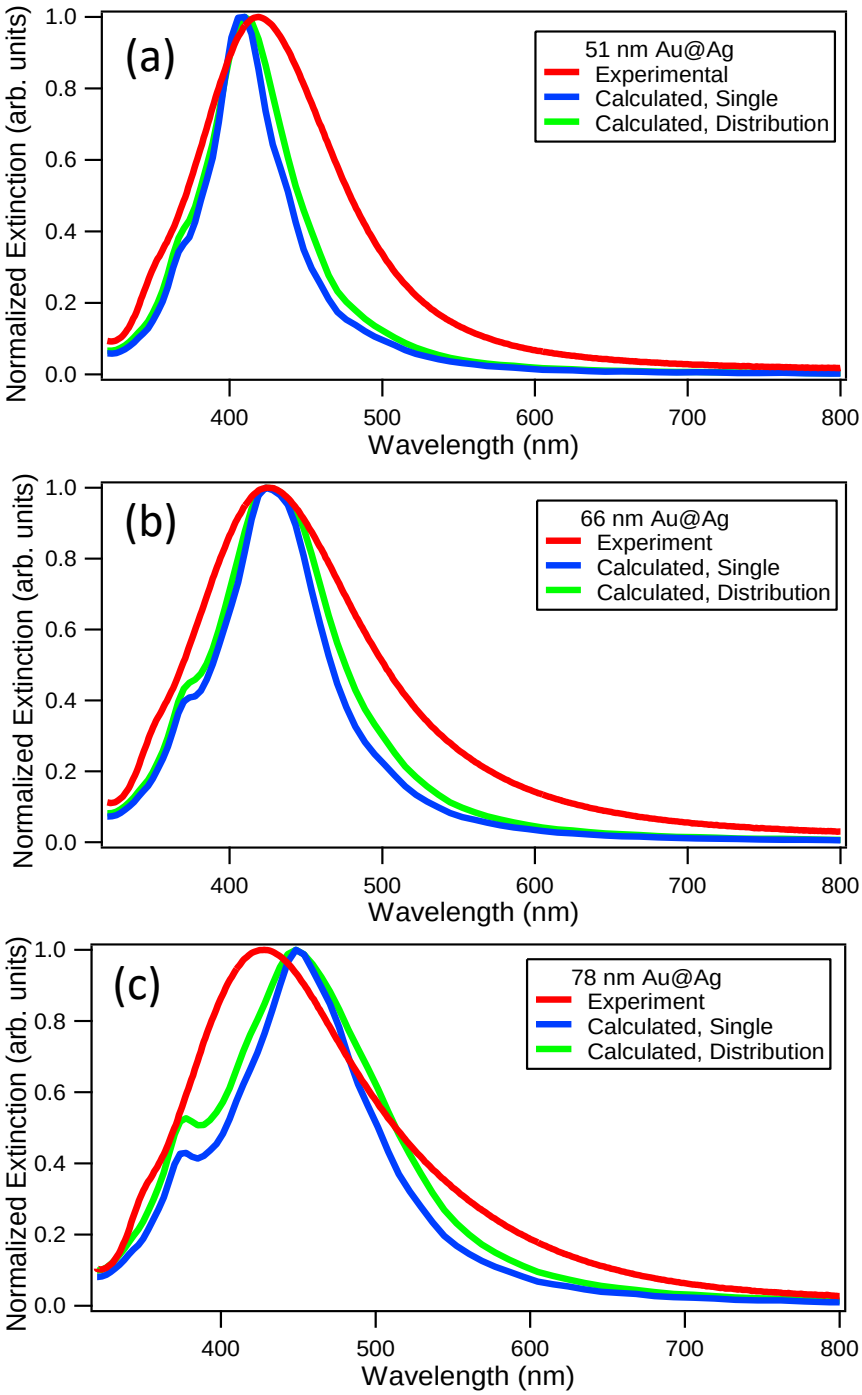

Figure 2.4. Normalized final extinction spectra (red line) of gold-silver core-shell nanoparticles prepared using (a) 27.5, (b) 22.5, and (c) 17.5 μL of precursor gold seeds, respectively, compared to corresponding spectra calculated using an FDTD approach from a single Au@Ag particle (blue line) and from a distribution of sizes (green line). The discrepancies between experiment and FDTD spectra are likely due to polydispersity in nanoparticle shapes and surface/interfacial roughness.

To analyze the influence of nanoparticle size distribution, the extinction spectra using a distribution of sizes are calculated, taking the five closest sizes for each Au@Ag nanoparticle sample with corresponding weighting to match the size distributions from the TEM measurements. These calculated spectra from distributions of Au@Ag nanoparticles, displayed as green curves in Figure 2.4, show increased spectral widths compared to the corresponding single nanoparticles. However, the experimental spectra still have greater spectral widths and lower amounts of red shifting as compared to the calculated spectra. From these simulations, we conclude that polydispersity in the nanoparticle sizes only play a small role in the observed experimental spectral broadening. Instead, the broadening is likely due to polydispersity in shape and surface morphology, as well as possible imperfections at the buried gold-silver core-shell interface.

In situ SHG spectroscopy provides a powerful and complementary tool to understand the nanoparticle growth dynamics, especially due to the surface sensitivity of the technique.[34, 35] Representative *in situ* SHG spectra for the Au@Ag sample prepared using 17.5 µL of gold seeds at selected reaction times are shown if Figure 2.5. Additional *in situ* SHG spectra for the Au@Ag sample prepared using 22.5 and 27.5 µL of gold seeds are shown in the Appendix A. The addition of AA and NaOH to the mixture of gold seeds, $AgNO_3$, and KI is designated as time zero, initiating the nanoparticle growth dynamics of the silver shell around the gold core, as described previously. The lower level of noise in the last SHG spectrum is a consequence of five-times longer acquisition times. The time-dependent SHG electric field during the silver shell growth is shown in Figure 2.6 for the three different gold-silver core-shell nanoparticle samples. The SHG signal is corrected

to account for the time-dependent linear extinction response using the equation, $I_{SHG,corr} = I_{SHG} \exp(\frac{1}{2}\varepsilon_{800} + \frac{1}{4}\varepsilon_{400})$, where I_{SHG}, ε_{800}, and ε_{400} represent the measured SHG intensity, the extinction at 800 nm, and the extinction at 400 nm, respectively.[34] The time-dependent SHG electric field is calculated from the square root of the integrated SHG signal, where $E_{SHG} = \sqrt{I_{SHG,corr}}$. The SHG intensity before time zero is very low because the gold nanoparticle seeds are small in size and have a lower degree of resonance enhancement at the SHG wavelength. After the addition of the reducing agent AA to the solution, the SHG intensity increases rapidly, reaching a peak intensity which is then followed by a biexponential decay as a function of time, where the relative intensities and corresponding lifetimes are different for each sample.

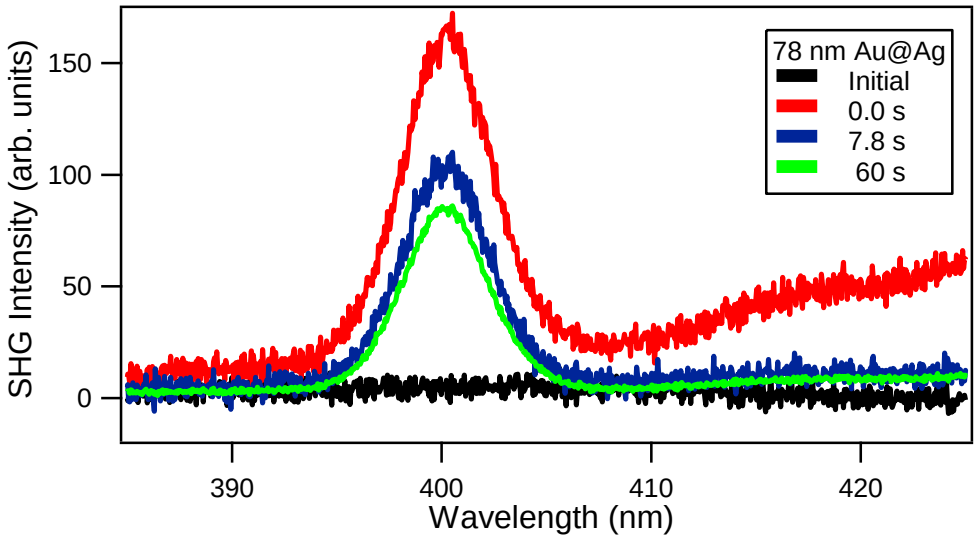

Figure 2.5. SHG spectra for gold-silver core-shell nanoparticles prepared using 17.5 μL of precursor gold seeds at different times during the reaction.

The SHG electric-field time traces are fit using a biexponential function given by $E_{SHG}(t) = A_1 e^{-t/\tau_1} + A_2 e^{-t/\tau_2} + B_{SHG}$, where t is the reaction time after addition of the reducing agent, τ_1 and τ_2 are the associated growth lifetimes, A_1 and A_2 are the corresponding amplitudes, and B_{SHG} is the offset SHG value. The corresponding fits are shown in Figure 2.6 and fitting parameters are tabulated in the Appendix A. Here, τ_1 and τ_2 are denoted as the fast SHG lifetime and the slow SHG lifetime, respectively. The fast SHG lifetime τ_1 increases as the final nanoparticle diameter increases with the values of 4.6 ± 0.5 s, 6.4 ± 0.2 s, and 10.0 ± 0.4 s for the final nanoparticle sizes of 51.0 nm, 65.8 nm, and 77.7 nm, respectively. Similarly, the slow SHG lifetime τ_2 also increases as the final nanoparticle diameter increases with values of 175 ± 9 s, 239 ± 17 s, and 268 ± 10 s for the final nanoparticle sizes of 51.0 nm, 65.8 nm, and 77.7 nm, respectively. The final SHG electric field per nanoparticle can be estimated by dividing B_{SHG} by the nanoparticle concentration, assuming each seed nanoparticle grows into a core-shell nanoparticle. This gives an estimated final SHG electric field measured per nanoparticle of (2.1 ± 0.2) × 10^{-8}, (2.8 ± 0.02) × 10^{-8}, and (3.9 ± 0.3) × 10^{-8} for the 51 nm, 66 nm, and 78 nm Au@Ag nanoparticles, respectively, in arbitrary units, showing increasing SHG signal as the nanoparticle size increases, in agreement with previous SHG studies of different types of nanoparticles.[35, 40, 62, 63] In addition, the SHG intensities of the Au@Ag nanoparticles have large plasmonic resonance enhancement at the second harmonic frequency.[64]

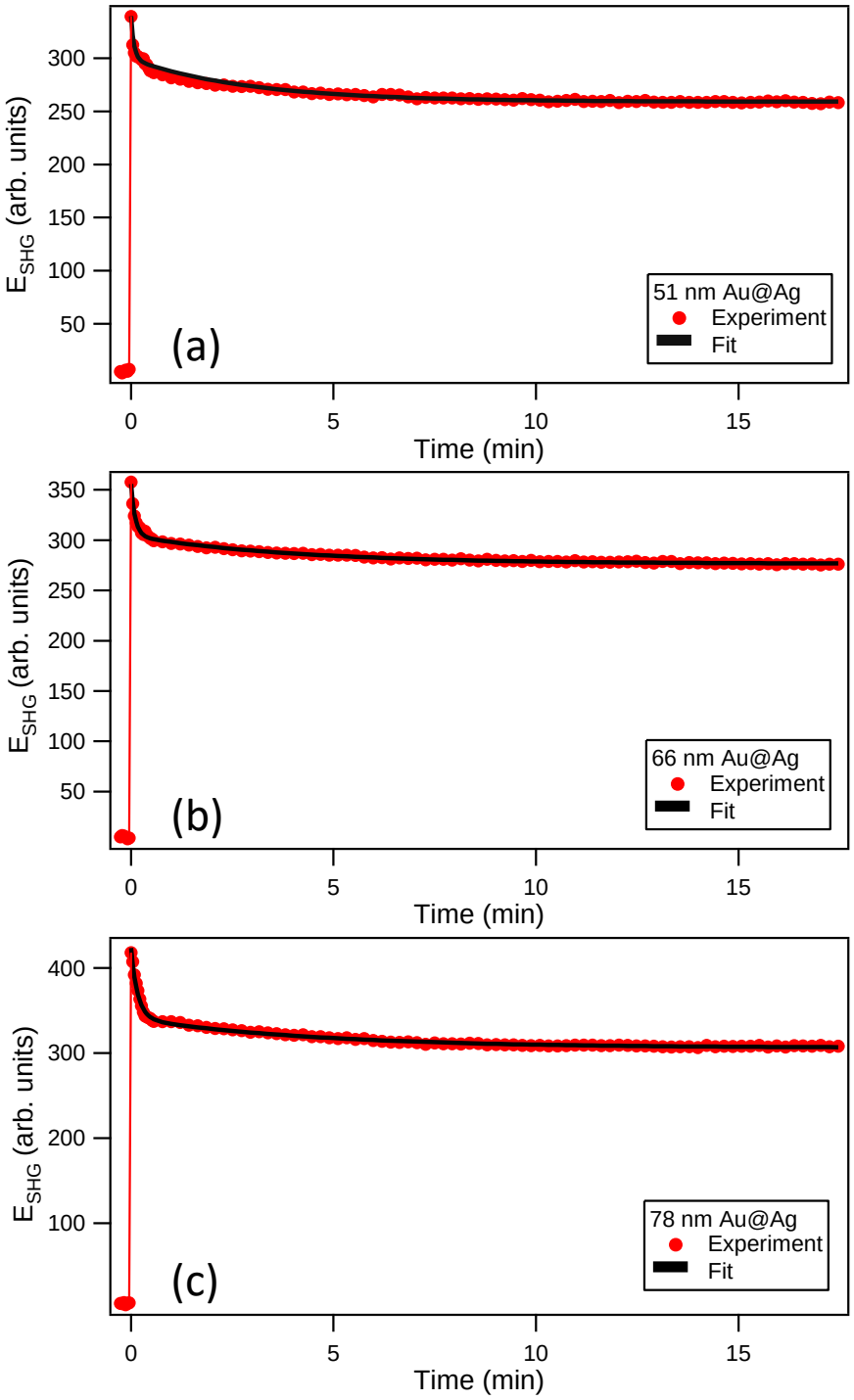

Figure 2.6. SHG electric field (red circles) as a function of reaction time during gold-silver core-shell nanoparticle reaction using (a) 27.5, (b) 22.5, and (c) 17.5 μL of precursor gold seeds, respectively, compared to the corresponding fits (black lines).

A comparison of these SHG lifetimes to the corresponding extinction growth lifetimes provides insight into the silver shell growth dynamics. The extinction growth lifetime τ_{ext} as a function the final nanoparticle diameter is shown in Figure 2.7(a). The fast SHG lifetime τ_1 and the slow SHG lifetime τ_2 are plotted as a function of the final nanoparticle diameter in the Figure 2.7(b) and (c), respectively. The fast SHG lifetimes are approximately equal to the corresponding extinction growth lifetimes, so τ_1 is also attributed to the timescale of the silver shell growth, where slight deviations between τ_1 and τ_{ext} are caused by the different associated optical processes, with τ_1 having enhanced surface sensitivity. However, the slow SHG lifetimes τ_2 occurs over much longer timescales, with the SHG signal continuing to decrease significantly even as the extinction spectrum and intensity remain constant. Therefore, the slow SHG lifetime τ_2 is attributed to changes in the nanoparticle surface charge density caused by the $\chi^{(3)}$ effect.[4, 36, 37] Ascorbic acid plays a major role as the reducing agent of Ag^+ at the nanoparticle surface and it can exist as both a carboxylic acid or an ascorbate anion conjugate base in various forms, with pH-dependent reactivity.[8, 12, 65, 66] As the reaction proceeds, ascorbic acid is converted to dehydroascorbic acid for the reduction of two Ag^+ ions, releasing two protons.[65] Excess ascorbate anions at the surface can then react back to ascorbic acid or leave the surface, resulting in a decreased surface charge density and a decreased SHG signal from the $\chi^{(3)}$ term. However, more work is needed to fully characterize the nanoparticle surface chemistry and the corresponding surface charge density during the nanoparticle shell growth reaction.

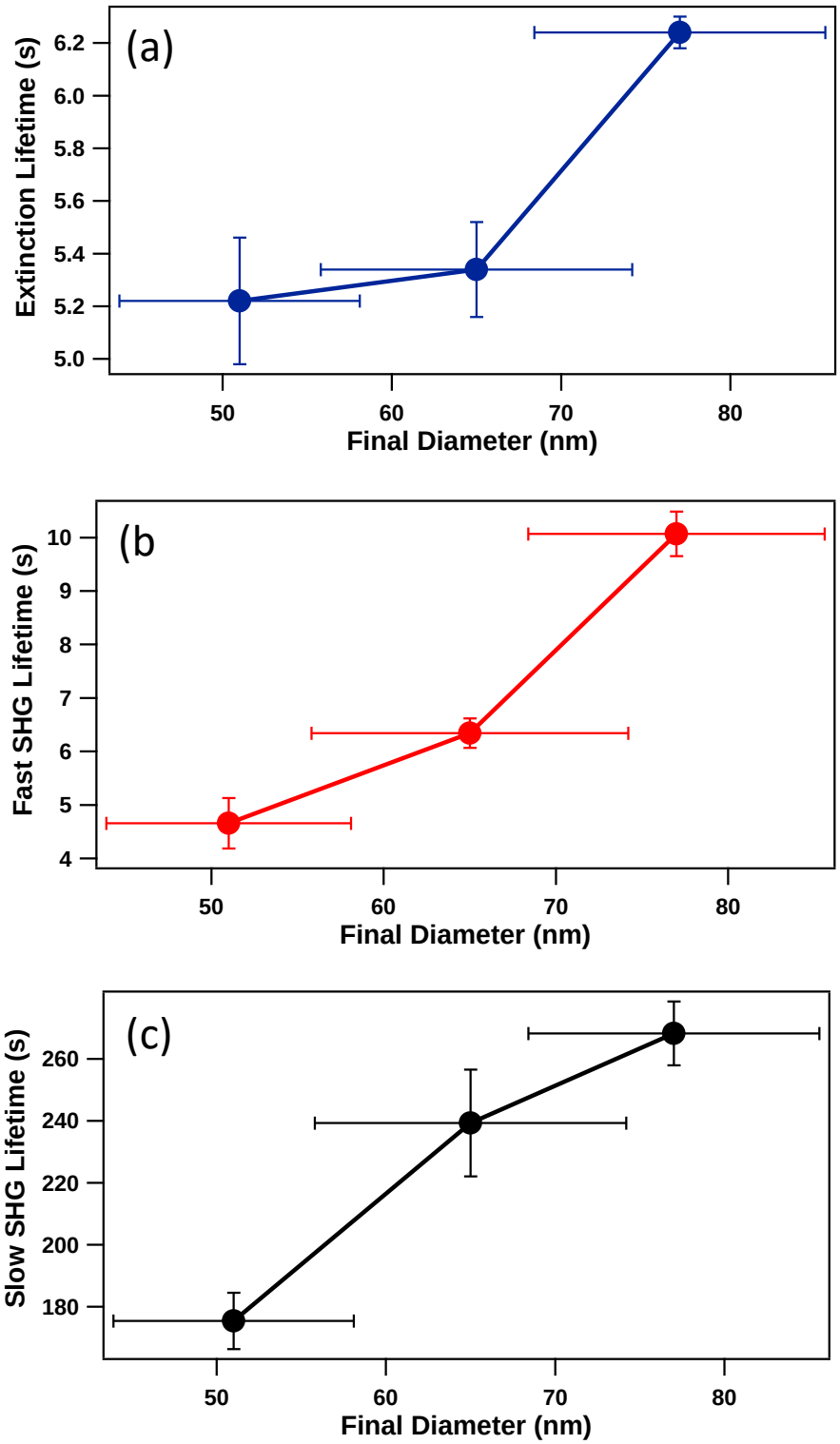

Figure 2.7. The measured (a) extinction growth lifetime, (b) fast SHG lifetime, and (c) slow SHG lifetime as a function of final core-shell nanoparticle diameter.

By analyzing both the *in situ* SHG and extinction spectroscopy together, with comparison to the FDTD calculations, a more extensive understanding of the gold-silver core-shell growth process is obtained. The results of the *in situ* SHG and extinction measurements of the Au@Ag nanoparticle growth dynamics can be described using a three-step model. The sudden rise in SHG signal immediately after the addition of AA constitutes the first step which is attributed to a period of rapid growth in shell size where the nanoparticle surface has a rough, uneven morphology characterized by nanoclustered domains or porous substructures. These bumpy surfaces generate increased SHG intensities due to plasmonic hot spots, similar to previous *in situ* SHG measurements from gold nanoparticle growth reactions.[34, 35] This first step occurs on a timescale that is faster than our current experimental temporal resolution. In the second step, the silver shell continues to grow and the nanoparticle surface becomes more smooth over time, where the decrease in plasmonic hot spots causes the overall SHG signal to decrease. This second step has characteristic lifetimes corresponding to τ_1 and τ_{ext}, where the *in situ* extinction spectra blue shifts and narrows over time, consistent with this picture,[35, 67] and where the shell growth lifetime increases with increasing nanoparticle size, in agreement with similar studies.[35, 68] Finally in the third step, the overall Au@Ag nanoparticle size remains constant and the corresponding extinction spectrum also remains constant, but additional nanoparticle surface chemistry reactions continue such that the surface charge density decreases causing the SHG signal to decrease from the $\chi^{(3)}$ effect on timescales of τ_2. Together, *in situ* SHG and extinction spectroscopy provides complementary information to study the dynamics of different

processes involved in size-dependent gold-silver core-shell nanoparticle growth reactions in solution for potential advances in nanoscale engineering.

2.4 Conclusion

In situ second harmonic generation and extinction spectroscopy is used to investigate the size-dependent growth dynamics of gold-silver core-shell nanoparticles in water. The *in situ* extinction spectra show rapid peak intensity increases upon the addition of ascorbic acid as the reducing agent to solutions of 14 nm colloidal gold seed nanoparticles and silver cations, with characteristic silver shell growth lifetimes of approximately 5 to 6 s. The nanoparticle growth reactions result in stable core-shell nanoparticles that vary in size from approximately 51 to 78 nm in diameter, depending on the initial seed concentration. The *in situ* SHG results show an abrupt increase followed by a biexponential decrease, where the faster SHG lifetimes are on the same timescale as the changes in extinction spectroscopy, corresponding to the shell growth process, while the slower SHG lifetimes of approximately 3 to 5 min are attributed to changes in the nanoparticle surface charge density. The final extinction spectra are compared to finite-difference time-domain calculations, displaying general agreement, where the plasmon peak increases in intensity, red shifts, and increases in spectral width as the silver shell increases in thickness. Based on the FDTD results, the broader experimental spectra are likely caused by distributions in non-spherical morphologies and surface/interfacial roughness, as opposed to polydispersity in size. The overall core-shell nanoparticle growth reaction is consistent with a three-step model, where the silver shell first grows abruptly with a large degree of plasmonic hot spots due to a rough, uneven surface, followed by continued growth with accompanying surface smoothening, followed

by a final step where the nanoparticle core-shell structure remains fixed in size but surface reactions continue which decrease the surface charge density leading to the final, stable colloidal Au@Ag nanoparticle sample. These *in situ* SHG and extinction spectroscopy results, combined with FDTD calculations, provide a sensitive method for studying of the real-time growth dynamics of colloidal gold-silver core-shell nanoparticles and similar hybrid core-shell structures that can be utilized in developing advanced plasmonic nanomaterial applications.

2.5 Notes

1. Haes, A. J.; Van Duyne, R. P., A Nanoscale Optical Biosensor: Sensitivity and Selectivity of an Approach Based on the Localized Surface Plasmon Resonance Spectroscopy of Triangular Silver Nanoparticles. *J. Am. Chem. Soc.* **2002,** *124*, 10596-10604.

2. Sperling, R. A.; Gil, P. R.; Zhang, F.; Zanella, M.; Parak, W. J., Biological Applications of Gold Nanoparticles. *Chem. Soc. Rev.* **2008,** *37*, 1896-1908.

3. Huang, X.; El-Sayed, I. H.; Qian, W.; El-Sayed, M. A., Cancer Cell Imaging and Photothermal Therapy in the Near-Infrared Region by Using Gold Nanorods. *J. Am. Chem. Soc.* **2006,** *128*, 2115-2120.

4. Kumal, R. R.; Karam, T. E.; Haber, L. H., Determination of the Surface Charge Density of Colloidal Gold Nanoparticles Using Second Harmonic Generation. *J. Phys. Chem. C* **2015,** *119*, 16200-16207.

5. Kamat, P. V., Meeting the Clean Energy Demand: Nanostructure Architectures for Solar Energy Conversion. *J. Phys. Chem. C* **2007,** *111*, 2834-2860.

6. Karam, T. E.; Haber, L. H., Molecular Adsorption and Resonance Coupling at the Colloidal Gold Nanoparticle Interface. *J. Phys. Chem. C* **2013,** *118*, 642-649.

7. Kumal, R. R.; Landry, C. R.; Abu-Laban, M.; Hayes, D. J.; Haber, L. H., Monitoring the Photocleaving Dynamics of Colloidal MicroRNA-Functionalized Gold Nanoparticles Using Second Harmonic Generation. *Langmuir* **2015,** *31*, 9983-9990.

8. Kumal, R. R.; Abu-Laban, M.; Hamal, P.; Kruger, B.; Smith, H. T.; Hayes, D. J.; Haber, L. H., Near-Infrared Photothermal Release of siRNA from the Surface of Colloidal Gold–Silver–Gold Core–Shell–Shell Nanoparticles Studied with Second-Harmonic Generation. *J. Phys. Chem. C* **2018,** *122*, 19699-19704.

9. Link, S.; El-Sayed, M. A., Shape and Size Dependence of Radiative, Non-Radiative and Photothermal Properties of Gold Nanocrystals. *Int. Rev. Phys. Chem.* **2000,** *19*, 409-453.

10. El-Sayed, I. H.; Huang, X.; El-Sayed, M. A., Surface Plasmon Resonance Scattering and Absorption of Anti-EGFR Antibody Conjugated Gold Nanoparticles in Cancer Diagnostics: Applications in Oral Cancer. *Nano Lett.* **2005,** *5*, 829-834.

11. Prigodich, A. E.; Lee, O.-S.; Daniel, W. L.; Seferos, D. S.; Schatz, G. C.; Mirkin, C. A., Tailoring DNA Structure to Increase Target Hybridization Kinetics on Surfaces. *J. Am. Chem. Soc.* **2010,** *132*, 10638-10641.

12. Karam, T. E.; Smith, H. T.; Haber, L. H., Enhanced Photothermal Effects and Excited-State Dynamics of Plasmonic Size-Controlled Gold–Silver–Gold Core–Shell–Shell Nanoparticles. *J. Phys. Chem. C* **2015,** *119*, 18573-18580.

13. Ho-Wu, R.; Sahu, P. K.; Wu, N.; Chen, T.; Yu, C.; Xie, J.; Goodson III, T., Understanding the Optical Properties of Au@ Ag Bimetallic Nanoclusters Through Time-Resolved and Nonlinear Spectroscopy. *J. Phys. Chem. C* **2018,** *122*, 24368-24379.

14. Abeyweera, S. C.; Rasamani, K. D.; Sun, Y., Ternary Silver Halide Nanocrystals. *Acc. Chem. Res.* **2017,** *50*,1754-1761.

15. Zhao, T.; Steves, M.; Chapman, B. S.; Tracy, J. B.; Knappenberger, K. L., Quantification of Interface-Dependent Plasmon Quality Factors Using Single-Beam Nonlinear Optical Interferometry. *Anal. Chem.* **2018**, *90*, 13702-13707

16. DeSantis, C. J.; Weiner, R. G.; Radmilovic, A.; Bower, M. M.; Skrabalak, S. E., Seeding Bimetallic Nanostructures as a New Class of Plasmonic Colloids. *J. Phys. Chem. Lett.* **2013,** *4*, 3072-3082.

17. Weiner, R. G.; Kunz, M. R.; Skrabalak, S. E., Seeding a New Kind of Garden: Synthesis of Architecturally Defined Multimetallic Nanostructures by Seed-Mediated Co-Reduction. *Acc. Chem. Res.* **2015,** *48*, 2688-2695.

18. Gilroy, K. D.; Ruditskiy, A.; Peng, H.-C.; Qin, D.; Xia, Y., Bimetallic Nanocrystals: Syntheses, Properties, and Applications. *Chem. Rev.* **2016,** *116*, 10414-10472.

19. Ye, X.; Shi, H.; He, X.; Wang, K.; Li, D.; Qiu, P., Gold Nanorod-Seeded Synthesis of Au@ Ag/Au Nanospheres with Broad and Intense Near-Infrared Absorption for Photothermal Cancer Therapy. *J. Mater. Chem. B* **2014,** *2*, 3667-3673.

20. Vickers, E. T.; Garai, M.; Bonabi Naghadeh, S.; Lindley, S.; Hibbs, J.; Xu, Q.-H.; Zhang, J. Z., Two-Photon Photoluminescence and Photothermal Properties of Hollow Gold Nanospheres for Efficient Theranostic Applications. *J. Phys. Chem. C* **2017,** *122*, 13304-13313.

21. Lindley, S. A.; Zhang, J. Z., Bumpy Hollow Gold Nanospheres for Theranostic Applications: Effect of Surface Morphology on Photothermal Conversion Efficiency. *ACS Appl. Nano Mater.* **2019,** *2*, 1072-1081.

22. Zarick, H. F.; Boulesbaa, A.; Talbert, E. M.; Puretzky, A.; Geohegan, D.; Bardhan, R., Ultrafast Excited-State Dynamics in Shape and Composition Controlled Gold–Silver Bimetallic Nanostructures. *J. Phys. Chem. C* **2017,** *121*, 4540-4547.

23. Lu, L.; Wang, H.; Zhou, Y.; Xi, S.; Zhang, H.; Hu, J.; Zhao, B., Seed-Mediated Growth of Large, Monodisperse Core–Shell Gold–Silver Nanoparticles with Ag-like Optical Properties. *Chem. Commun.* **2002,** 144-145.

24. Norris, C. B.; Joseph, P. R.; Mackiewicz, M. R.; Reed, S. M., Minimizing Formaldehyde Use in the Synthesis of Gold−Silver Core−Shell Nanoparticles. *Chem. Mater.* **2010,** *22*, 3637-3645.

25. Lu, L.; Burkey, G.; Halaciuga, I.; Goia, D. V., Core–Shell Gold/Silver Nanoparticles: Synthesis and Optical Properties. *J. Colloid Interface Sci.* **2013,** *392*, 90-95.

26. Tsuji, M.; Miyamae, N.; Lim, S.; Kimura, K.; Zhang, X.; Hikino, S.; Nishio, M., Crystal Structures and Growth Mechanisms of Au@ Ag Core−Shell Nanoparticles Prepared by the Microwave−Polyol Method. *Crystal growth & design* **2006,** *6*, 1801-1807.

27. Gonzalez, C. M.; Liu, Y.; Scaiano, J., Photochemical Strategies for the Facile Synthesis of Gold− Silver Alloy and Core−Shell Bimetallic Nanoparticles. *J. Phys. Chem. C* **2009,** *113*, 11861-11867.

28. McGilvray, K. L.; Fasciani, C.; Bueno-Alejo, C. J.; Schwartz-Narbonne, R.; Scaiano, J. C., Photochemical Strategies for the Seed-Mediated Growth of Gold and Gold–Silver Nanoparticles. *Langmuir* **2012,** *28*, 16148-16155.

29. Anandan, S.; Grieser, F.; Ashokkumar, M., Sonochemical Synthesis of Au− Ag Core− Shell Bimetallic Nanoparticles. *J. Phys. Chem. C* **2008,** *112*, 15102-15105.

30. Ghosh Chaudhuri, R.; Paria, S., Core/Shell Nanoparticles: Classes, Properties, Synthesis Mechanisms, Characterization, and Applications. *Chem. Rev.* **2011,** *112*, 2373-2433.

31. Woehl, T. J.; Evans, J. E.; Arslan, I.; Ristenpart, W. D.; Browning, N. D., Direct In Situ Determination of the Mechanisms Controlling Nanoparticle Nucleation and Growth. *ACS Nano* **2012,** *6*, 8599-8610.

32. Tan, S. F.; Chee, S. W.; Lin, G.; Bosman, M.; Lin, M.; Mirsaidov, U.; Nijhuis, C. A., Real-Time Imaging of the Formation of Au–Ag Core–Shell Nanoparticles. *J. Am. Chem. Soc.* **2016,** *138*, 5190-5193.

33. Polte, J. r.; Tuaev, X.; Wuithschick, M.; Fischer, A.; Thuenemann, A. F.; Rademann, K.; Kraehnert, R.; Emmerling, F., Formation Mechanism of Colloidal Silver Nanoparticles: Analogies and Differences to the Growth of Gold Nanoparticles. *ACS Nano* **2012,** *6*, 5791-5802.

34. Sauerbeck, C.; Haderlein, M.; Schürer, B.; Braunschweig, B. R.; Peukert, W.; Klupp Taylor, R. N., Shedding Light on the Growth of Gold Nanoshells. *ACS Nano* **2014,** *8*, 3088-3096.

35. Khoury, R. A.; Ranasinghe, J. C.; Dikkumbura, A. S.; Hamal, P.; Kumal, R. R.; Karam, T. E.; Smith, H. T.; Haber, L. H., Monitoring the Seed-Mediated Growth of Gold Nanoparticles Using in Situ Second Harmonic Generation and Extinction Spectroscopy. *J. Phys. Chem. C* **2018,** *122*, 24400-24406.

36. Hayes, P. L.; Malin, J. N.; Jordan, D. S.; Geiger, F. M., Get Charged Up: Nonlinear Optical Voltammetry for Quantifying the Thermodynamics and Electrostatics of Metal Cations at Aqueous/Oxide Interfaces. *Chem. Phys. Lett.* **2010,** *499*, 183-192.

37. Yan, E. C.; Liu, Y.; Eisenthal, K. B., New Method for Determination of Surface Potential of Microscopic Particles by Second Harmonic Generation. *J. Phys. Chem. B* **1998,** *102*, 6331-6336.

38. Eisenthal, K. B., Second Harmonic Spectroscopy of Aqueous Nano and Microparticle Interfaces. *Chem. Rev.* **2006,** *106*, 1462-1477.

39. Shen, Y., Surface Properties Probed by Second Harmonic and Sum Frequency Generation. *Nature* **1989,** *337*, 519.

40. Jen, S.-H.; Gonella, G.; Dai, H.-L., The Effect of Particle Size in Second Harmonic Generation from the Surface of Spherical Colloidal Particles. I: Experimental Observations. *J. Phys. Chem. A* **2009,** *113*, 4758-4762.

41. Song, Z.; Sarkar, S.; Vogt, A. D.; Danzer, G. D.; Smith, C. J.; Gualtieri, E. J.; Simpson, G. J., Kinetic Modeling of Accelerated Stability Testing Enabled by Second Harmonic Generation Microscopy. *Anal. Chem.* **2018,** *90*, 4406-4413.

42. Kumal, R. R.; Nguyenhuu, H.; Winter, J. E.; McCarley, R. L.; Haber, L. H., Impacts of Salt, Buffer, and Lipid Nature on Molecular Adsorption and Transport in Liposomes As Observed by Second Harmonic Generation. *J. Phys. Chem. C* **2017,** *121*, 15851-15860.

43. Nguyen, T. T.; Sly, K. L.; Conboy, J. C., Comparison of the Energetics of Avidin, Streptavidin, NeutrAvidin, and Anti-Biotin Antibody Binding to Biotinylated Lipid Bilayer Examined by Second Harmonic Generation. *Anal. Chem.* **2011,** *84*, 201-208.

44. Fearon, A. D.; Stokes, G. Y., Thermodynamics of Indomethacin Adsorption to Phospholipid Membranes. *J. Phys. Chem. B* **2017,** *121*, 10508-10518.

45. Liu, J.; Subir, M.; Nguyen, K.; Eisenthal, K. B., Second Harmonic Studies of Ions Crossing Liposome Membranes in Real Time. *J. Phys. Chem. B* **2008,** *112*, 15263-15266.

46. Darlington, A. M.; Gibbs-Davis, J. M., Bimodal or Trimodal? The Influence of Starting pH on Site Identity and Distribution at the Low Salt Aqueous/Silica Interface. *J. Phys. Chem. C* **2015,** *119*, 16560-16567.

47. Dreier, L. B.; Bernhard, C.; Gonella, G.; Backus, E. H.; Bonn, M., Surface Potential of a Planar Charged Lipid–Water Interface. What Do Vibrating Plate Methods, Second Harmonic and Sum Frequency Measure? *J. Phys. Chem. Lett.* **2018,** *9*, 5685-5691.

48. Liu, Y.; Dadap, J.; Zimdars, D.; Eisenthal, K. B., Study of Interfacial Charge-Transfer Complex on TiO2 Particles in Aqueous Suspension by Second Harmonic Generation. *J. Phys. Chem. B* **1999,** *103*, 2480-2486.

49. Jin, R.; Jureller, J. E.; Ki, H. Y.; Scherer, N. F., Correlating Second Harmonic Optical Responses of Single Ag Nanoparticles with Morphology. *J. Am. Chem. Soc.* **2005,** *127*, 12482-12483.

50. Vance, F. W.; Lemon, B. I.; Hupp, J. T., Enormous Hyper-Rayleigh Scattering from Nanocrystalline Gold Particle Suspensions. *J. Phys. Chem. B* **1998,** *102*, 10091-10093.

51. Hao, E.; Schatz, G.; Johnson, R.; Hupp, J., Hyper-Rayleigh Scattering from Silver Nanoparticles. *J. Chem. Phys.* **2002,** *117*, 5963-5966.

52. Russier-Antoine, I.; Benichou, E.; Bachelier, G.; Jonin, C.; Brevet, P., Multipolar Contributions of the Second Harmonic Generation from Silver and Gold Nanoparticles. *J. Phys. Chem. C* **2007,** *111*, 9044-9048.

53. Bachelier, G.; Butet, J.; Russier-Antoine, I.; Jonin, C.; Benichou, E.; Brevet, P.-F., Origin of Optical Second Harmonic Generation in Spherical Gold Nanoparticles: Local Surface and Nonlocal Bulk Contributions. *Phys. Rev. B* **2010,** *82*, 235403.

54. Haber, L. H.; Kwok, S. J.; Semeraro, M.; Eisenthal, K. B., Probing the Colloidal Gold Nanoparticle/Aqueous Interface with Second Harmonic Generation. *Chem. Phys. Lett.* **2011,** *507*, 11-14.

55. Gan, W.; Gonella, G.; Zhang, M.; Dai, H.-L., Reactions and Adsorption at the Surface of Silver Nanoparticles Probed by Second Harmonic Generation. *J. Chem. Phys.* **2011,** *134*, 041104.

56. Perrault, S. D.; Chan, W. C., Synthesis and Surface Modification of Highly Monodispersed, Spherical Gold Nanoparticles of 50− 200 nm. *J. Am. Chem. Soc.* **2009,** *131*, 17042-17043.

57. Brown, K. R.; Walter, D. G.; Natan, M. J., Seeding of Colloidal Au Nanoparticle Solutions. 2. Improved Control of Particle Size and Shape. *Chem. Mater.* **2000,** *12*, 306-313.

58. Samal, A. K.; Polavarapu, L.; Rodal-Cedeira, S.; Liz-Marzán, L. M.; Pérez-Juste, J.; Pastoriza-Santos, I., Size Tunable Au@ Ag Core–Shell Nanoparticles: Synthesis and Surface-Enhanced Raman Scattering Properties. *Langmuir* **2013,** *29*, 15076-15082.

59. Smith, H. T.; Karam, T. E.; Haber, L. H.; Lopata, K., Capturing Plasmon–Molecule Dynamics in Dye Monolayers on Metal Nanoparticles Using Classical Electrodynamics with Quantum Embedding. *J. Phys. Chem. C* **2017,** *121*, 16932-16942.

60. Coomar, A.; Arntsen, C.; Lopata, K. A.; Pistinner, S.; Neuhauser, D., Near-field: A Finite-Difference Time-Dependent Method for Simulation of Electrodynamics on Small Scales. *J. Chem. Phys.* **2011,** *135*, 084121.

61. Lopata, K.; Neuhauser, D., Multiscale Maxwell–Schrödinger Modeling: A Split Field Finite-Difference Time-Domain Approach to Molecular Nanopolaritonics. *J. Chem. Phys.* **2009,** *130*, 104707.

62. Roke, S.; Gonella, G., Nonlinear Light Scattering and Spectroscopy of Particles and Droplets in Liquids. *Annu. Rev. Phys. Chem.* **2012,** *63*, 353-378.

63. Dadap, J. I.; Shan, J.; Eisenthal, K. B.; Heinz, T. F., Second Harmonic Rayleigh Scattering from a Sphere of Centrosymmetric Material. *Phys. Rev. Lett.* **1999,** *83*, 4045.

64. Abid, J.-P.; Nappa, J.; Girault, H. H.; Brevet, P.-F., Pure Surface Plasmon Resonance Enhancement of the First Hyperpolarizability of Gold Core Silver Shell Nanoparticles. *J. Chem. Phys.* **2004,** *121*, 12577-12582.

65. Patra, S.; Sen, D.; Pandey, A. K.; Bahadur, J.; Mazumder, S.; Ramagiri, S. V.; Bellare, J. R.; Roth, S. V.; Santoro, G.; Yu, S., Time Resolved Growth of Membrane Stabilized Silver NPs and their Catalytic Activity. *RSC Adv.* **2014,** *4*, 59379-59386.

66. Qin, Y.; Ji, X.; Jing, J.; Liu, H.; Wu, H.; Yang, W., Size Control Over Spherical Silver Nanoparticles by Ascorbic Acid Reduction. *Colloids Surf., A* **2010,** *372*, 172-176.

67. Wang, Y.; Camargo, P. H.; Skrabalak, S. E.; Gu, H.; Xia, Y., A facile, water-based synthesis of highly branched nanostructures of silver. *Langmuir* **2008,** *24*, 12042-12046.

68. Jana, N. R.; Gearheart, L.; Murphy, C. J., Evidence for Seed-Mediated Nucleation in the Chemical Reduction of Gold Salts to Gold Nanoparticles. *Chem. Mater.* **2001,** *13*, 2313-2322.

Chapter 3. Efficient Photoinduced Energy Transfer in Porphyrin-Based Nanomaterials

3.1 Introduction

The synthesis, characterization, and ultrafast dynamics of porphyrin- and zinc porphyrin-based nanomaterials are reported. Spherical nanoparticles composed of a group of uniform materials based on organic salts (nanoGUMBOS) are prepared from either porphyrin or zinc porphyrin with trihexyl(tetradecyl)phosphonium in aqueous colloidal suspension with sizes of approximately 50 nm in diameter. The ultrafast excited-state dynamics of the porphyrin and zinc porphyrin nanoGUMBOS in water are measured using transient absorption spectroscopy with 400 nm excitation and the results are compared to corresponding measurements of the porphyrin molecular dyes in water. Porphyrin and zinc porphyrin have long-lived excited states arising from the intersystem crossing of the S_1 state to the triplet T_1 These excited-state lifetimes are significantly faster in the corresponding porphyrin-based nanoGUMBOS as compared to the porphyrin molecules due to intermolecular energy transfer, electronic delocalization, and the altered chemical environment of the nanomaterials. Additionally, these results show that porphyrin-based nanoGUMBOS are promising nanomaterials for light-harvesting solar cells and optoelectronics.

Organic and organometallic nanomaterials have drawn great interest due to their many potential applications including photothermal cancer therapy,[1-2] biosensing,[3] and optoelectronics.[4] A group of uniform materials based on organic salts or GUMBOS represents an emerging class of organic and organometallic materials that provides a wide range of controllable chemical, physical, and optoelectronic characteristics.[5] Colloidal nanoparticles prepared from GUMBOS are given the term of nanoGUMBOS and

are extraordinary due to their facile synthesis, highly tunable photophysical properties, and their extended list of applications in biomedical imaging,[6] antibiotics,[7-8] cancer therapy,[9] molecular sensing,[10-12] organic light-emitting diodes,[13-14] and photovoltaics.[15] Recently, porphyrin-based nanoGUMBOS were investigated and shown to be promising candidates as photosensitizers for dye sensitized solar cells and optoelectronics.[16] However, a better understanding of the fundamental photophysical properties of these nanomaterials is needed for the design and optimization of new light-harvesting and optoelectronic devices.

Previously, we investigated the ultrafast excited-state dynamics of different types of nanoGUMBOS using transient absorption spectroscopy.[17-18] In one study, we reported the observation of tunable intermolecular energy transfer in crystalline ruthenium bipyridine−bis(pentafluoroethylsulfonyl)imide ($[Ru(bipy)_3]$-$[BETI]_2$) nanoGUMBOS in colloidal suspension in water.[17] Size-dependent relaxation dynamics were observed in the nanoGUMBOS, characterized by decay dynamics similar to the $Ru(bipy)_3Cl_2$ dye with an added relaxation pathway from intermolecular energy transfer.[17] Additionally, size-dependent phonon oscillations were observed, where the phonon frequency increases as the nanoparticle size increases. This anomalous phonon trend suggests a very low coupling between electronic and phonon degrees of freedom and a strong hydrophobic interaction with the aqueous solvent.[17] In a second study, brilliant green–bis(pentafluoroethylsulfonyl)imide ([BG][BETI]) nanoGUMBOS demonstrated slower relaxation dynamics compared to the BG molecular dye due to steric hindrance of the torsional degrees of freedom of the phenyl rings around the central carbon in the nanoGUMBOS environment, while also displaying enhanced nonlinear optical signals.[18]

Understanding the excited-state dynamics of different porphyrin-based nanoGUMBOS is essential for the development and optimization of various optoelectronic applications. In this respect, porphyrin nanoGUMBOS provide a new route for the synthesis of highly-tunable functional organic nanomaterial applications with enhanced photonics properties.

Porphyrin molecular dyes are particularly attractive due to their optical and chemical tunability as well as their highly efficient electron transfer in donor-acceptor configurations, making them promising candidates for advanced dye sensitized solar cells and optoelectronic devices.[19-22] Additionally, porphyrin dyes can be easily altered by changing the central hydrogen atoms in the heterocyclic structure with different metal ions such as Zn^{2+}, Co^{2+}, and Cu^{2+}. These M-porphyrin-based dyes can be used for the development of artificial light-harvesting antennae that mimic photosynthesis by transferring the absorbed photon energy to a reaction center.[23] For example, zinc porphyrin-sensitized solar cells with a cobalt(II/III)-based redox electrolyte previously recorded an excellent conversion efficiency of 12.3%.[19] Several porphyrin-based synthetic strategies have been utilized for photovoltaics including configurations based on arrays,[24-25] dimers,[26] dendrimers,[27] controlled aggregation,[28] and supramolecular assemblies.[29-30] These synthetic strategies require strong absorbance in the visible region and enhanced electron transfer for efficient photovoltaic designs.[31-32] Porphyrin hexamers have also been studied due to their near-infrared luminescence for organic light emitting diodes.[33] The unique chemical and optical properties of porphyrins lead to an extensive list of potential applications including photodynamic therapy,[34-37] catalysis,[38-41] and optoelectronics.[19, 42] The excited-state dynamics of porphyrin molecular dyes have been studied using various ultrafast pump-probe spectroscopic techniques.[43-47] Additionally,

the excited-state relaxation processes and interfacial energy transfer mechanisms of porphyrin dyes in solution and attached at substrates have been investigated with ultrafast spectroscopy.[21, 26, 28] The emerging field of molecular-based nanomaterials, such as nanoGUMBOS, provides the ability to study how molecular photophysical properties are altered as individual molecules are restructured into size-controlled nanomaterials for potential enhanced optoelectronic applications.[16-18]

In this chapter, we report on the investigations of the excited-state relaxation dynamics of colloidal [M-TCPP][P66614]$_4$ nanoGUMBOS, with M = H_2 and Zn, using ultrafast pump-probe time-resolved transient absorption spectroscopy with pump pulse excitation at 400 nm and white light continuum femtosecond probe pulses. The transient absorption results obtained for the nanoGUMBOS are compared to corresponding results acquired from aqueous solutions of the M–porphyrin molecular dyes. In the nanoGUMBOS samples, additional efficient energy transfer relaxation pathways are observed leading to significantly shorter excited-state lifetimes. In addition, the excited-state dynamics of [Zn-TCPP][P66614]$_4$ nanoGUMBOS are remarkably faster compared to the molecular dye due to increase of the electronic delocalization caused by the metal center, causing enhanced energy transfer in the excited-state relaxation dynamics. These results show that these nanoGUMBOS are highly attractive for designing new, efficient light harvesting nanomaterials. The use of organic or organometallic nanoparticles of this type in solar cell devices is advantageous due to their large surface to volume ratios leading to expected increased energy conversion efficiencies. These transient absorption spectroscopy studies provide a fundamental understanding of the ultrafast processes

controlling photodynamics and energy transfer for advancing potential applications in molecular-based optoelectronic nanomaterials.

3.2 Experimental Section

3.2.1 NanoGUMBOS Synthesis

Meso-tetra(4-carboxyphenyl)porphyrin (H_2-TCPP) and zinc (II) meso-tetra(4-carboxyphenyl)porphyrin (Zn–TCPP) in acid form were purchased from Frontier Scientific. Trihexyl(tetradecyl)phosphonium chloride ([P66614][Cl]) was purchased from Sigma-Aldrich. The GUMBOS are synthesized using a metathesis reaction carried out in a binary solvent mixture, as reported previously,[16] in collaboration with Dr. Warner's research group at LSU. Briefly, H_2-TCPP or Zn–TCPP is neutralized using an excess of aqueous sodium hydroxide to obtain water soluble tetrasodium salt in 10% excess. The other reactant [P66614][Cl] is dissolved in dichloromethane (DCM). The two solutions are then mixed and stirred for 40 hours. After the reaction is complete, the product is washed several times with water followed by the removal of the DCM by rotary evaporation under reduced pressure. The residual water is removed by freeze drying and the final yield of the [M-TCPP][P66614]$_4$ GUMBOS product is approximately 96%. NanoGUMBOS are synthesized via reprecipitation of the GUMBOS in water by adding 50 µL of a 1 mM GUMBOS stock ethanolic solution into 5 mL of water under sonication for 30 minutes. The reaction scheme of the [M-TCPP][P66614]$_4$ GUMBOS is shown in Figure 3.1. The reprecipitation of [M-TCPP][P66614]$_4$ in water produces spherical nanoparticles with an average sizes of 49 ± 25 nm for the [H_2-TCPP][P66614]$_4$ nanoGUMBOS and 52 ± 15 nm for the [Zn-TCPP][P66614]$_4$ nanoGUMBOS. Representative transmission electron

microscopy (TEM) images of $[H_2\text{-TCPP}][P66614]_4$ and [Zn-TCPP] $[P66614]_4$ nanoGUMBOS are shown in Figures 3.2 (a) and (b), respectively.

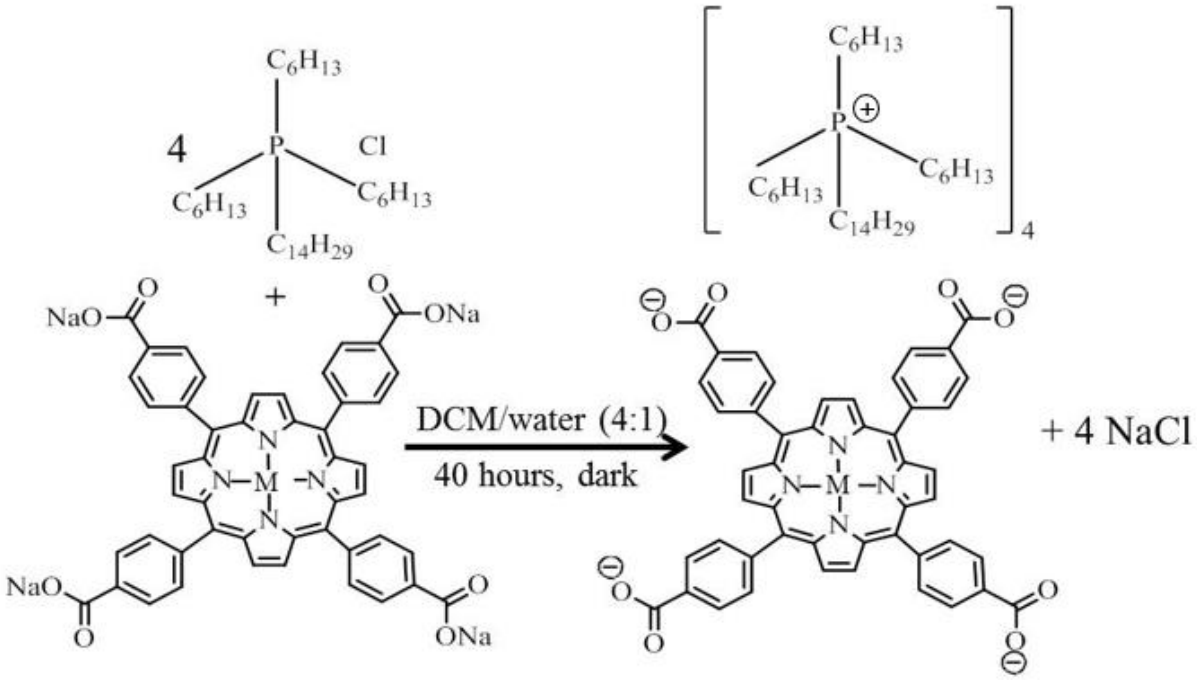

Figure 3.1. Reaction scheme of the synthesis of $[M\text{-TCPP}][P66614]_4$ GUMBOS.

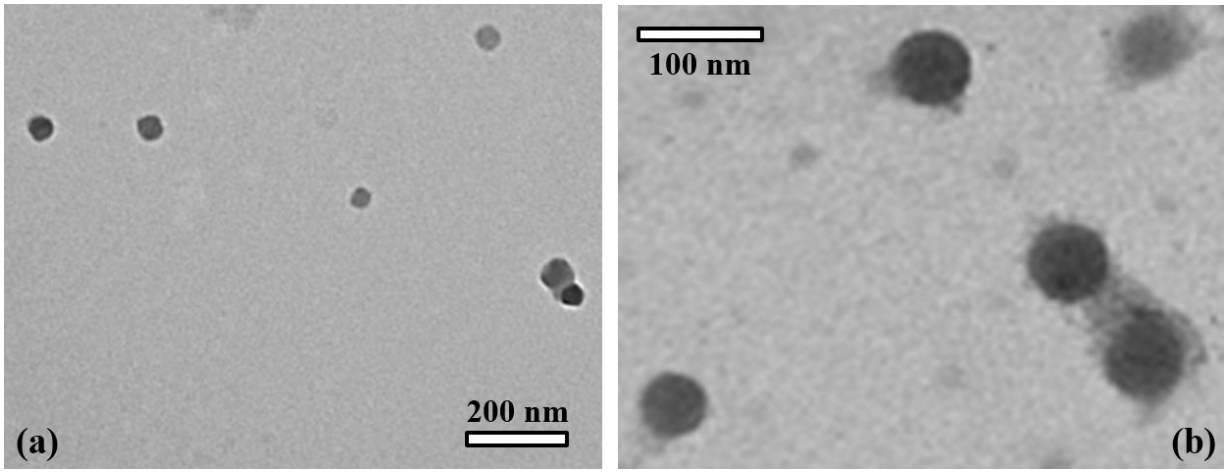

Figure 3.2. TEM images of (a) 49 nm $[H_2\text{-TCPP}][P66614]_4$ nanoGUMBOS and (b) 52 nm $[Zn\text{-TCPP}][P66614]_4$ nanoGUMBOS.

3.2.2 Transient Absorption

Ultrafast transient absorption spectroscopy is a powerful technique for the investigation of excited-state relaxation dynamics of molecules and nanomaterials.[17-18] Our home-built transient absorption setup consists of an ultrafast laser system, an optical setup, and a fiber optic spectrometer detector. The experimental setup for the transient absorption spectroscopy is shown in Figure B.1 of the Appendix. The laser pulses are generated by a Titanium:sapphire laser system that produces 75 fs pulses centered at 800 nm with a 10 kHz repetition rate and an average power of 0.7 mJ/pulse. The initial laser beam is separated into pump and probe beams using a beam splitter. The 400 nm pump pulse beam is generated by frequency doubling by focusing the beam into a nonlinear beta barium borate crystal. An optical filter is then used to remove any 800 nm residual light yielding an excitation power of 0.16 μJ/pulse. The probe pulses are focused into a fused quartz flow cell containing water to generate the femtosecond white light probe pulses. The pump and probe beams are refocused to a spatial overlap in the sample which is contained in a 3 mm fused quartz flow cell. The pump-probe optical delay is controlled using a retroreflector on a computer-controlled translation stage for the pump beam. Background spectra, with the probe only are subtracted from the pump-probe spectra using an automated beam block for each pump-probe time delay. Several spectral scans are acquired for each sample studied, and the transient absorption spectra are acquired several times for statistical analysis.

3.3. Results and Discussion

The extinction and fluorescence spectra of the H_2-TCPP and Zn-TCPP molecular dyes and the corresponding nanoGUMBOS are first measured for direct analysis and

comparison. Figure 3.3. (a) shows the extinction spectra of H_2-TCPP molecular dye and [H_2-TCPP] [P66614]$_4$ nanoGUMBOS, with the Soret band corresponding to the S_0–S_2 transition[48] centered at 413 nm and 421 nm for H_2-TCPP dye and [H_2-TCPP][P66614]$_4$ nanoGUMBOS, respectively. The extinction spectra of Zn-TCPP molecular dye and [Zn-TCPP][P66614]$_4$ nanoGUMBOS are shown in Figure 3.3. (b), with the Soret band centered at 420 nm and 435 nm for Zn-TCPP dye and [Zn-TCPP][P66614]$_4$ nanoGUMBOS, respectively. A red shift and broadening of the Soret band is observed in both [H_2-TCPP][P66614]$_4$ and [Zn-TCPP][P66614]$_4$ nanoGUMBOS, which is attributed to a flattening of the porphyrin molecules in the nanoGUMBOS environment.[16, 49] The Q bands, arising from the lower-energy S_0–S_1 transition, are centered after 500 nm for both dyes and both nanoGUMBOS samples. Due to the lower symmetry of porphyrin, The Q bands splits into different components of unequal energies Q_x and Q_y with 5 different absorption peaks for H_2-TCPP centered around 518, 550, 598, and 653 nm.[50-51] [H_2-TCPP][P66614]$_4$ nanoGUMBOS show higher intensity Q bands at wavelengths centered around 518, 553, 596 and 653 nm, which are very similar to the H_2-TCPP molecular dye. The Q bands centered around 565 and 608 nm are degenerate in the D_{4h} symmetry for Zn-TCPP. In [Zn-TCPP] [P66614]$_4$ nanoGUMBOS, a slight red shift in Q bands with greater intensity is observed at 569 and 611 nm.

The fluorescence peaks observed in the molecular dyes and the nanoGUMBOS are from the $Q_x(0,0)$ and $Q_x(0,1)$ transitions.[43-44] The dominant relaxation channel of this Q_x transition is through intersystem crossing to T_1 state, which has a very long lifetime on the order of microseconds to milliseconds.[52] Figure 3.4 (a) shows the fluorescence spectra of H_2-TCPP molecular dye in water and [H_2-TCPP] [P66614]$_4$ nanoGUMBOS in

water. The H_2-TCPP dye has a high intensity fluorescence band centered at 640 nm and a lower intensity band centered at 720 nm. In the case of [H_2-TCPP][P66614]$_4$ nanoGUMBOS, the lower-wavelength band is enhanced and red-shifted to 660 nm, while the higher-wavelength band is red-shifted to 725 nm. The fluorescence spectra of Zn-TCPP molecular dye in water and [Zn-TCPP][P66614]$_4$ nanoGUMBOS in water are shown in Figure 3.4 (b). The Zn-TCPP dye has a high intensity fluorescence band centered at 610 nm and a lower intensity band centered at 660 nm. In the case of [H_2-TCPP][P66614]$_4$ nanoGUMBOS, the lower-wavelength band is quenched and red-shifted to 625 nm, while the higher-wavelength band is enhanced and red-shifted to 680 nm. The absorbance and luminescence bands of H_2-TCPP and Zn-TCPP are red-shifted in the nanoGUMBOS compared to the corresponding free dye molecule in water due to the presence of the four bulky hydrophobic P66614 cations, leading to the formation of loosely packed aggregates in the nanoGUMBOS.[53]

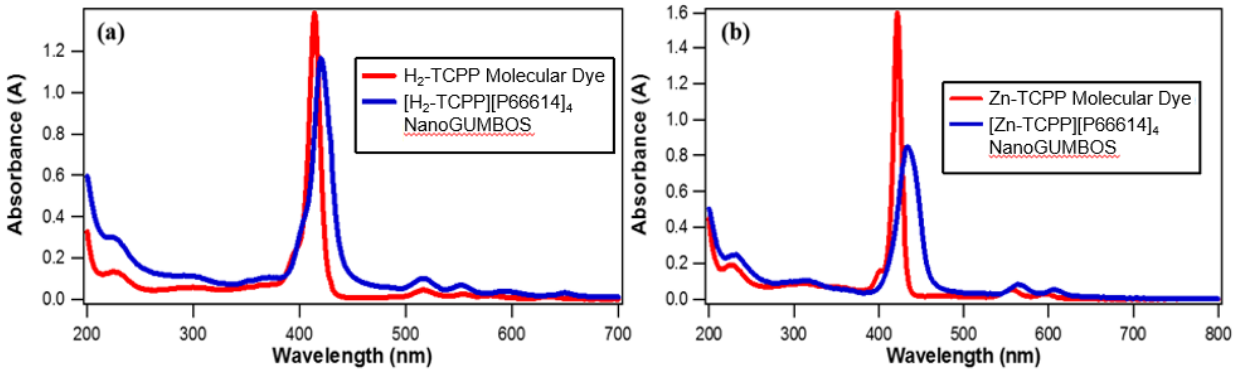

Figure 3.3. Absorbance spectra of (a) (red line) 10 μM H_2-TCPP molecular dye and (blue line) 10 μM [H_2-TCPP][P66614]$_4$ nanoGUMBOS, and (b) (red line) 10 μM Zn-TCPP molecular dye and (blue line) 10 μM [Zn-TCPP][P66614]$_4$ nanoGUMBOS.

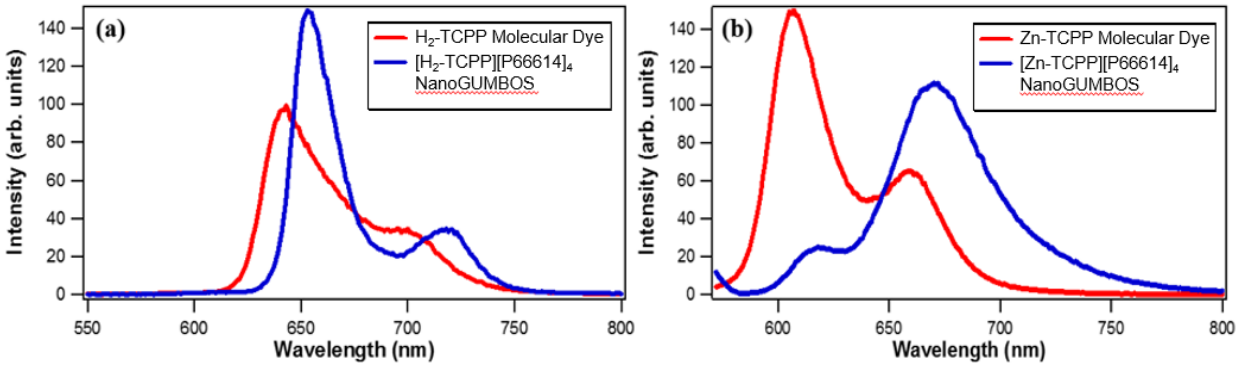

Figure 3.4. Fluorescence spectra of (a) (red line) 10 μM H_2-TCPP molecular dye in water and (blue line) 10 μM [H_2-TCPP][P66614]$_4$ colloidal nanoGUMBOS after excitation at 420 nm, and (b) (red line) 10 μM Zn-TCPP molecular dye in water and (blue line) 10 μM [Zn-TCPP][P66614]$_4$ colloidal nanoGUMBOS after excitation at 420 nm.

The ultrafast excited-state dynamics of different samples of the M-TCPP molecular dyes are measured using transient absorption spectroscopy with 400 nm excitation pulses and the results are compared to the nanoGUMBOS samples. Figure 3.5 (a) shows transient absorption spectra of 20 μM aqueous H_2-TCPP. A negative band centered at 422 nm is due to depletion of the ground state population, followed by a broad positive spectrum after 425 nm from excited-state absorption. An isosbestic point separating the ground state depletion band and the excited-state absorption region is observed at 424 nm. Representative time profiles of the transient absorption spectra of aqueous H_2-TCPP integrated at 422 nm and 430 nm are shown in Figure 3.5 (b). These time profiles change rapidly upon excitation due to S_2 to S_1 state internal conversion, then S_1 to triplet T_1 state intersystem crossing, both of which occur on faster timescales than the current experimental temporal resolution.[44] After these rapid transitions occur after time zero, the time profiles remain relatively constant due to the very long lifetime of the T_1 triplet state,

which is significantly longer than the optical pump-probe time delays used in the experiment.[44]

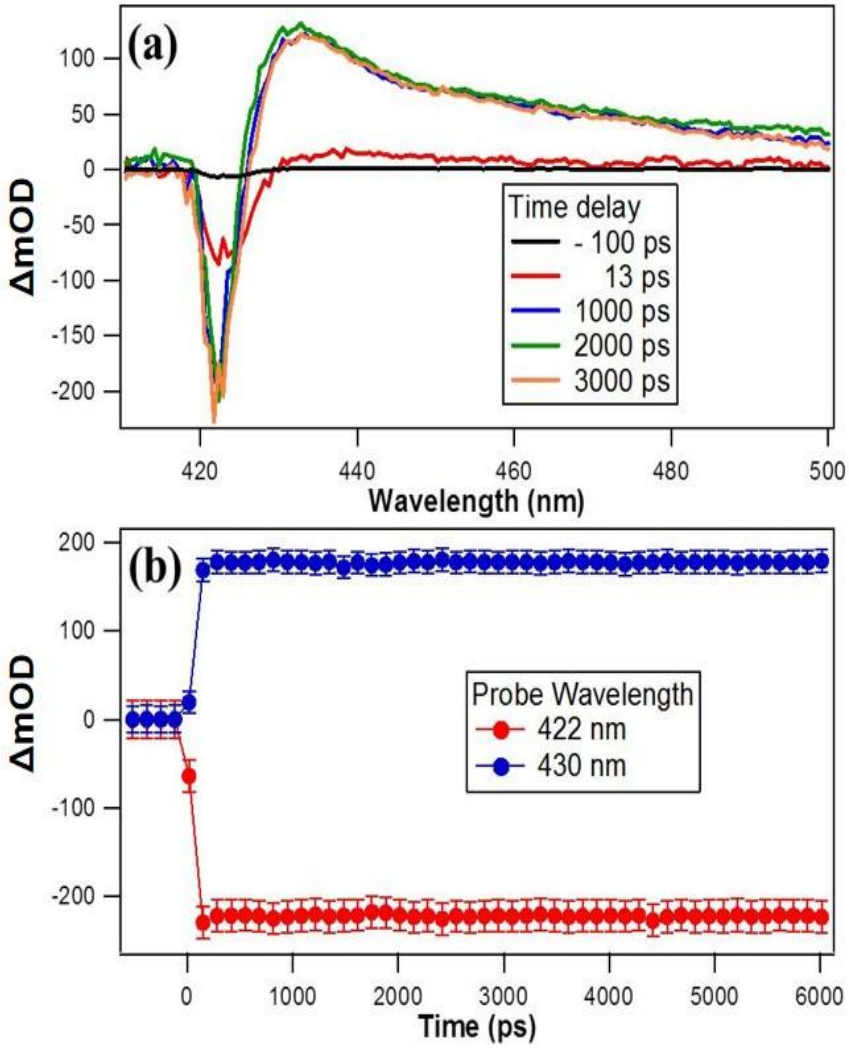

Figure 3.5. (a) Transient absorption spectra of 20 μM H_2-TCPP molecular dye in water at different time delays using 400 nm excitation. (b) Time profiles of the transient absorption spectra of aqueous H_2-TCPP molecular dye. The time-dependent signals are measured at 422 nm and 430 nm.

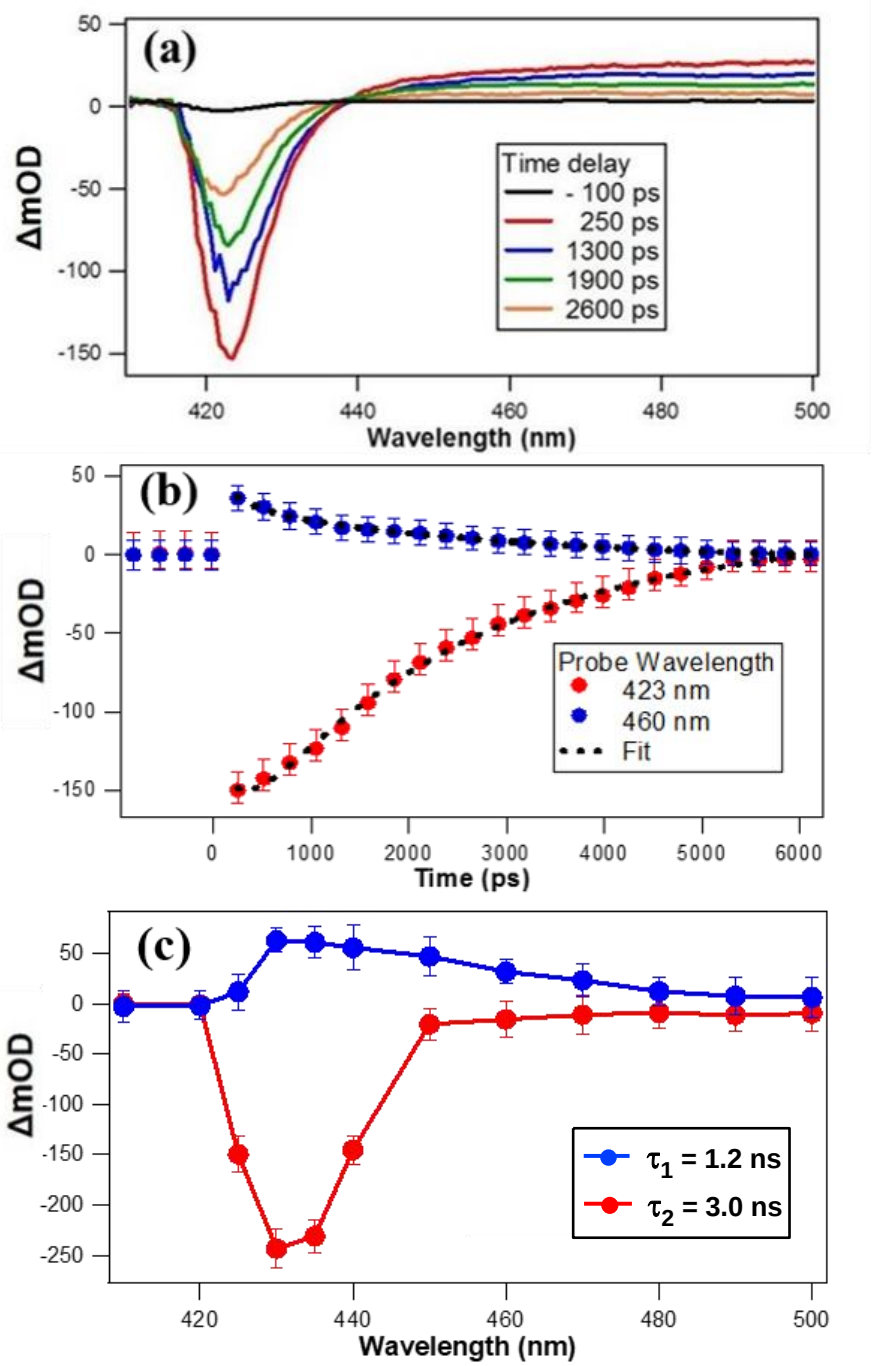

Figure 3.6. (a) Transient absorption spectra of colloidal $[H_2\text{-TCPP}][P66614]_2$ nanoGUMBOS at different time delays using 400 nm excitation. (b) Time profiles of the transient absorption spectra of colloidal $[H_2\text{-TCPP}][P66614]_2$ nanoGUMBOS. The time-dependent signals are measured at 423 nm and 460 nm. (c) Decay spectra obtained using a sum of exponential fits of time-dependent transient absorption spectra of colloidal $[H_2\text{-TCPP}][P66614]_2$ nanoGUMBOS.

The excited-state dynamics of [H_2-TCPP][P66614]$_4$ nanoGUMBOS are studied and compared to those obtained from H_2-TCPP molecular dye in order to understand aspects of the photophysical changes occurring due to the altered nanoGUMBOS environment. Figure 3.6 (a) displays the transient absorption spectra of colloidal [H_2-TCPP][P66614]$_4$ nanoGUMBOS at different time delays using 400 nm excitation pulses. A negative depletion band is centered at 423 nm followed by a broad positive spectrum from excited-state absorption after 440 nm. The two spectral features are separated by an isosbestic point at 438 nm. Representative time profiles of the transient absorption spectra of colloidal [H_2-TCPP][P66614]$_4$ nanoGUMBOS integrated at 423 nm and 460 nm are shown in Figure 3.6 (b). As shown in Figure 3.6 (c), the experimental data are fit with a global analysis technique using a sum of exponential functions.[17-18, 54] The equation used in the global analysis fit is of the form $I(t) = y_0 + \sum_{i=1}^{n} A_i \exp\left(-\frac{t}{\tau_i}\right)$, where n is the number of lifetimes required to accurately fit the time profiles obtained from the transient absorption spectra. Two lifetimes are required to accurately fit the temporal evolution of the transient signal over the wavelength range of the experiment with lifetimes of τ_1 = 1.2 ± 0.1 ns and τ_2 = 3.0 ± 0.1 ns. The transient absorption results demonstrate that the excited-state dynamics of the [H_2-TCPP][P66614]$_4$ nanoGUMBOS are significantly faster than those of the aqueous H_2-TCPP dye. In the nanoparticle, H_2-TCPP acts as an efficient energy donor and acceptor, with this pathway greatly enhanced due to the closely-packed nanoGUMBOS environment. In the [H_2-TCPP][P66614]$_4$ nanoGUMBOS, the shorter lifetime of τ_1 is attributed to energy transfer, while the longer lifetime of τ_2 is ascribed to relaxation of the S_1 state (Q_x state) through intersystem crossing to the T_1 triplet state.[44] The decay spectrum corresponding to the enhanced intersystem crossing in the [H_2-

TCPP][P66614]$_4$ nanoGUMBOS is dominated by ground-state depletion, as shown in Figure 3.6 (c), while the decay spectrum corresponding to energy transfer in dominated by excited-state absorption. The excited-state dynamics of the porphyrin are observed to be significantly faster in the nanoGUMBOS than in the molecular dye alone, which is caused by the combination of energy transfer and enhanced intersystem crossing in the nanomaterial environment, leading to dramatically altered photophysical properties of the nanoGUMBOS.[55-56]

The effect of a zinc center on the excited-state dynamics of aqueous Zn-TCPP and colloidal [Zn-TCPP][P66614]$_4$ nanoGUMBOS are also investigated. Figure 3.7 (a) shows the transient absorption spectra of aqueous Zn-TCPP molecular dye at different time delays using 400 nm excitation pulses. A negative ground-state depletion band is centered at 426 nm, followed by a positive broad spectrum after 435 nm due to excited-state absorption. The two spectral regions are separated by an isosbestic point at 433 nm. Representative time traces from the transient absorption spectra integrated at 428 nm and 450 nm are shown is Figure 3.7 (b). Analysis of these time traces demonstrates that these relaxation dynamics are described using a single lifetime of τ_3 = 2.0 ± 0.2 ns. This lifetime is attributed to the relaxation of the S_1 state (Q_x state) to the triplet T_1 state through intersystem crossing. Previous studies on the up-conversion fluorescence spectroscopy of the similar dye molecule, zinc tetraphenylporphyrin (ZnTPP), in benzene observed a similar lifetime of 1.7 ns.[43] In our measurements, the slightly different zinc-porphyrin molecular structure in the different highly-polar aqueous solvent cause a longer relaxation lifetime for this intersystem crossing transition. Here, the presence of the Zn

metal center significantly decreases this lifetime in the Zn-TCPP molecular dye as compared to the H_2-TCPP molecular dye due to electronic delocalization.

The transient absorption of the Zn-TCPP molecular dye is also studied under higher temporal resolution, using smaller pump-probe time delay steps, with all other experimental conditions the same. Representative transient absorption spectra under higher temporal resolution are shown in Figure 3.7 (c), where the relative intensity of the ground-state depletion is greater than the corresponding spectra shown in Figure 3.7 (b) at longer delay times. The time profile of Zn-TCPP molecular dye in water at short time delays integrated at 425 nm is shown in Figure 3.7 (d) and can be fit with a single exponential function with a lifetime τ_4 = 75 ± 2 ps, which is attributed to the vibrational relaxation of the S_1 excited-state population, after the internal conversion from the S_2 state.[43-44] Previous transient absorption studies on the similar dye molecule ZnTPP in benzene and dichoromethane measured lifetimes of vibrational relaxation of the S_1 state to be approximately 12 ps and 38 ps, respectively, where the solvent interaction was found to play an important role in these dynamics.[43] Here, the slightly different molecular of structure of Zn-TCPP in the different solvent of water shows a significantly longer lifetime where an overall trend of increasing lifetimes for solvents of increasing polarity is observed. The internal conversion from the excited S_2 to S_1 states, which is expected to occur on timescales of approximately 1 ps,[43] is faster than the current experimental temporal resolution conditions employed.

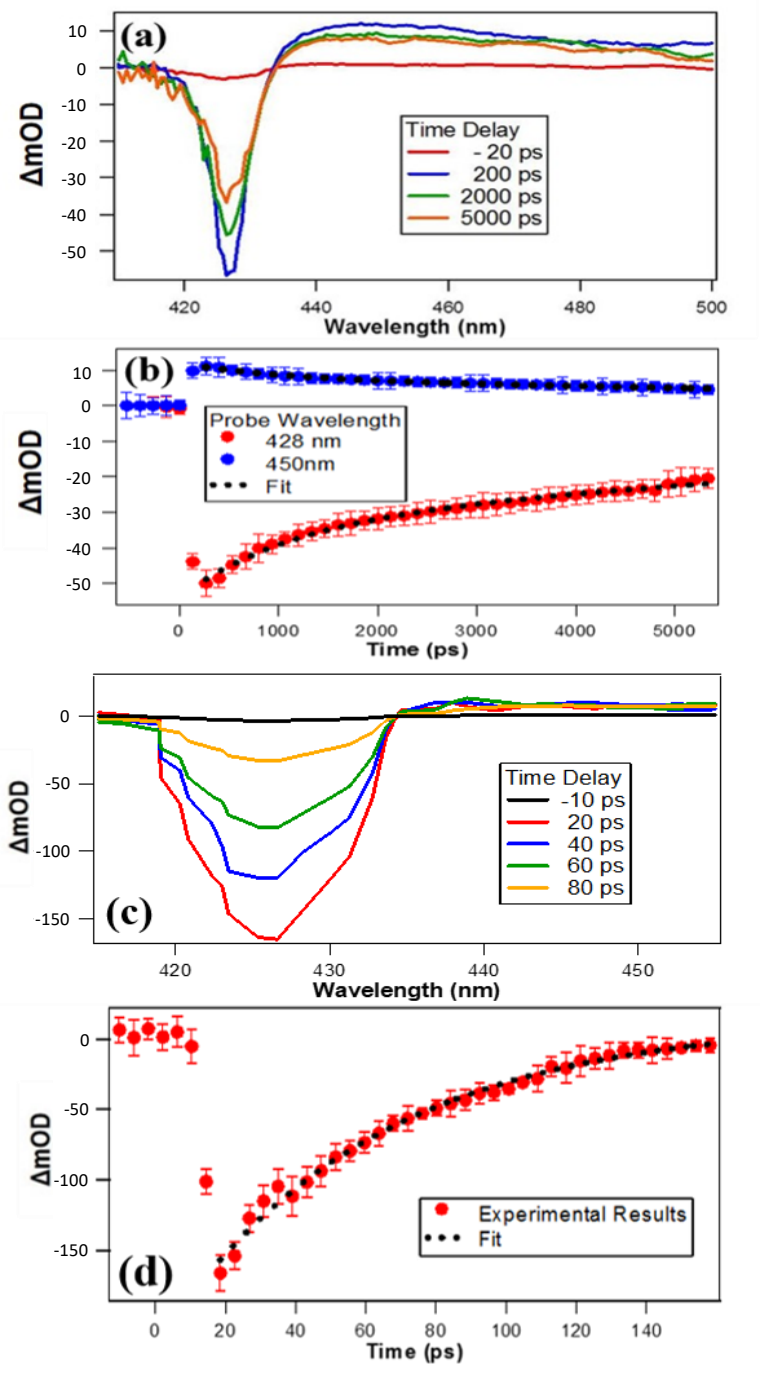

Figure 3.7. (a) Transient absorption spectra of 20 µL aqueous Zn-TCPP molecular dye at different time delays using 400 nm excitation. (b) Time profiles of the transient absorption spectra of aqueous Zn-TCPP molecular dye. The time-dependent signals are measured at 428 nm and 450 nm. (c) Transient absorption spectra of 20 µL aqueous Zn-TCPP molecular dye at different time delays at short time steps using 400 nm excitation. (d) Time profiles of Zn-TCPP molecular dye at short time delays integrated at 425 nm

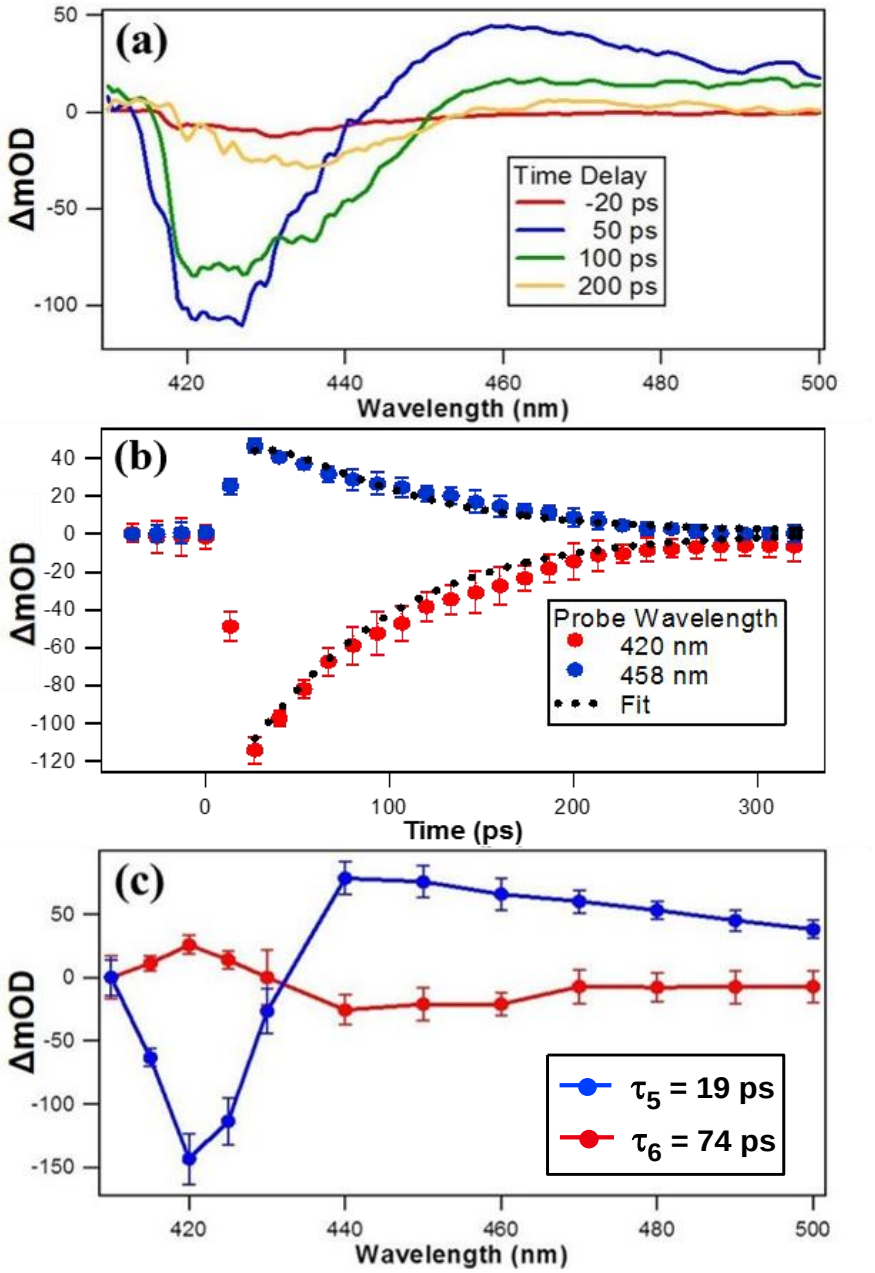

Figure 3.8. (a) Transient absorption spectra of colloidal [Zn-TCPP][P66614]$_4$ nanoGUMBOS at different time delays using 400 nm excitation. (b) Time profiles of the transient absorption spectra of colloidal [Zn-TCPP][P66614]$_4$ nanoGUMBOS. The time-dependent signals are measured at 428 nm and 450 nm. (c) Decay spectra obtained using a sum of exponential fits of time-dependent transient absorption spectra of colloidal [Zn-TCPP][P66614]$_4$ nanoGUMBOS.

Additionally, transient absorption spectroscopy measurements are performed on the colloidal [Zn-TCPP][P66614]$_4$ nanoGUMBOS. Figure 3.8 (a) shows the transient absorption spectra of colloidal [Zn-TCPP][P66614]$_4$ nanoGUMBOS at different time delays using 400 nm excitation. A ground-state depletion band is centered at 425 nm, followed by a broad excited-state absorption spectrum after 450 nm. The time-dependent transient absorption spectra integrated at 420 nm and 458 nm are shown in Figure 3.8 (b). The corresponding decay spectra from the global analysis of the time profiles are shown in Figure 3.8 (c). The time profiles are fit using a sum of two exponential functions with lifetimes τ_5 = 19 ± 1 ps and τ_6 = 74 ± 6 ps. The faster lifetime τ_5 is attributed to intersystem crossing of the S_1 state to the T_1 state, since the corresponding decay spectrum is dominated by ground-state depletion near 420 nm, with the transient absorption spectra approximately equal to zero to within experimental uncertainty after the decay of this τ_5 signal. The slower lifetime τ_6 is ascribed primarily to intermolecular energy transfer between Zn-TCPP in the nanoGUMBOS environment, because this lifetime and corresponding decay spectrum is not observed in the Zn-TCPP molecular dye alone in water. Here, the presence of the intermolecular energy transfer pathway also increases the rate of relaxation of the S_1 state in the nanoGUMBO material caused by a larger degree of electronic delocalization in the nanoGUMBOS environment. In contrast to the decay spectrum of energy transfer in the [H_2-TCPP][P66614]$_4$ nanoGUMBOS, which is dominated by excited-state absorption, the decay spectrum of energy transfer in the [Zn-TCPP][P66614]$_4$ nanoGUMBOS has both positive excited-state absorption character near 420 nm and negative ground-state depletion character near 450 nm. These transient absorption results of porphyrin and zinc-porphyrin molecular dyes and

the comparisons to the corresponding nanoGUMBOS provide key information on altered photodynamic properties in molecular-based nanomaterials for enhancing energy transfer and excited-state relaxation in potential optoelectronic applications.

3.4 Conclusion

The ultrafast relaxation dynamics of colloidal porphyrin- and zinc porphyrin-based nanomaterials are studied using transient absorption spectroscopy, showing dramatically faster lifetimes and altered spectra as compared to the corresponding parent dye molecules in water. $[H_2\text{-TCPP}][P66614]_4$ and $[Zn\text{-TCPP}][P66614]_4$ nanoGUMBOS are prepared using a metathesis reaction, resulting in stable 50 nm nanospheres in stable aqueous colloidal suspension. Transient absorption spectroscopy of H_2-TCPP and Zn-TCPP molecular dyes in water upon 400 nm excitation display long-lived excited states from intersystem crossing of the S_1 state to the triplet T_1 state. The corresponding nanoGUMBOS show dramatically faster relaxation dynamics with an additional pathway due to intermolecular energy transfer in the altered nanoGUMBOS environment, which is characterized by close-packing aggregates of the porphyrin and P66614 molecular ions. In addition, the Zn-porphyrin nanGUMBOS demonstrate very efficient relaxation dynamics and energy transfer caused by increased electronic delocalization from the Zn metal center. This highly-efficient energy transfer pathway is very promising for potential applications in photovoltaics and optoelectronics. These studies also provide fundamental insight on ultrafast photodynamics for advancing technology utilizing molecular-based nanomaterials.

3.5 Notes

1. Yang, K.; Xu, H.; Cheng, L.; Sun, C.; Wang, J.; Liu, Z., In Vitro and In Vivo Near-Infrared Photothermal Therapy of Cancer Using Polypyrrole Organic Nanoparticles. *Adv. Mater.* **2012,** *24*, 5586-5592.

2. Yang, J.; Choi, J.; Bang, D.; Kim, E.; Lim, E. K.; Park, H.; Suh, J. S.; Lee, K.; Yoo, K. H.; Kim, E. K., Convertible Organic Nanoparticles for Near-Infrared Photothermal Ablation of Cancer Cells. *Angew. Chem. int ed* **2011,** *50*, 441-444.

3. Petkau, K.; Kaeser, A.; Fischer, I.; Brunsveld, L.; Schenning, A. P., Pre and Postfunctionalized Self-Assembled π-Conjugated Fluorescent Organic Nanoparticles for Dual Targeting. *J. Am. Chem. Soc.* **2011,** *133*, 17063-17071.

4. An, B.-K.; Kwon, S.-K.; Jung, S.-D.; Park, S. Y., Enhanced Emission and Its Switching in Fluorescent Organic Nanoparticles. *J. Am. Chem. Soc.* **2002,** *124*, 14410-14415.

5. Warner, I. M.; El-Zahab, B.; Siraj, N., Perspectives on Moving Ionic Liquid Chemistry Into the Solid Phase. *Anal. Chem.* **2014,** *86*, 7184-7191.

6. Bwambok, D. K.; El-Zahab, B.; Challa, S. K.; Li, M.; Chandler, L.; Baker, G. A.; Warner, I. M., Near-Infrared Fluorescent NanoGUMBOS for Biomedical Imaging. *ACS Nano* **2009,** *3*, 3854-3860.

7. Cole, M. R.; Li, M.; Jadeja, R.; El-Zahab, B.; Hayes, D.; Hobden, J. A.; Janes, M. E.; Warner, I. M., Minimizing Human Infection from Escherichia Coli O157: H7 Using GUMBOS. *J. Antimicrob. Chemother.* **2013,** *68*, 1312-1318.

8. Cole, M. R.; Li, M.; El-Zahab, B.; Janes, M. E.; Hayes, D.; Warner, I. M., Design, Synthesis, and Biological Evaluation of β-Lactam Antibiotic-Based Imidazolium-and Pyridinium-Type Ionic Liquids. *Chem. Biol. Drug Des.* **2011,** *78*, 33-41.

9. Magut, P. K.; Das, S.; Fernand, V. E.; Losso, J.; McDonough, K.; Naylor, B. M.; Aggarwal, S.; Warner, I. M., Tunable Cytotoxicity of Rhodamine 6G Via Anion Variations. *J. Am. Chem. Soc.* **2013,** *135*, 15873-15879.

10. Das, S.; Magut, P. K.; de Rooy, S. L.; Hasan, F.; Warner, I. M., Ionic Liquid-Based Fluorescein Colorimetric pH Nanosensors. *RSC Adv.* **2013,** *3*, 21054-21061.

11. Lu, C.; Das, S.; Magut, P. K.; Li, M.; El-Zahab, B.; Warner, I. M., Irradiation Induced Fluorescence Enhancement in PEGylated Cyanine-Based NIR Nano and Mesoscale GUMBOS. *Langmuir* **2012,** *28*, 14415-14423.

12. Regmi, B. P.; Monk, J.; El-Zahab, B.; Das, S.; Hung, F. R.; Hayes, D. J.; Warner, I. M., A Novel Composite Film for Detection and Molecular Weight Determination of Organic Vapors. *J. Mater. Chem.* **2012,** *22*, 13732-13741.

13. Das, S.; Bwambok, D.; El-Zahab, B.; Monk, J.; de Rooy, S. L.; Challa, S.; Li, M.; Hung, F. R.; Baker, G. A.; Warner, I. M., Nontemplated Approach to Tuning the Spectral Properties of Cyanine-Based Fluorescent NanoGUMBOS. *Langmuir* **2010,** *26*, 12867-12876.

14. Siraj, N.; Hasan, F.; Das, S.; Kiruri, L. W.; Steege Gall, K. E.; Baker, G. A.; Warner, I. M., CarbazoleDderived Group of Uniform Materials Based on Organic Salts: Solid State Fluorescent Analogues of Ionic Liquids for Potential Applications in Organic-Based Blue Light-Emitting Diodes. *J. Phys. Chem. C* **2014,** *118*, 2312-2320.

15. Jordan, A. N.; Das, S.; Siraj, N.; de Rooy, S. L.; Li, M.; El-Zahab, B.; Chandler, L.; Baker, G. A.; Warner, I. M., Anion-Controlled Morphologies and Spectral Features of Cyanine-Based NanoGUMBOS–An Improved Photosensitizer. *Nanoscale* **2012,** *4*, 5031-5038.

16. Kolic, P. E.; Siraj, N.; Hamdan, S.; Regmi, B. P.; Warner, I. M., Synthesis and Characterization of Porphyrin-Based GUMBOS and NanoGUMBOS as Improved Photosensitizers. *J. Phys. Chem. C* **2016,** *120*, 5155-5163.

17. Karam, T. E.; Siraj, N.; Warner, I. M.; Haber, L. H., Anomalous Size-Dependent Excited-State Relaxation Dynamics of NanoGUMBOS. *J. Phys. Chem. C* **2015,** *119*, 28206-28213.

18. Karam, T. E.; Siraj, N.; Zhang, Z.; Ezzir, A. F.; Warner, I. M.; Haber, L. H., Ultrafast and Nonlinear Spectroscopy of Brilliant Green-Based NanoGUMBOS with Enhanced Near-Infrared Emission. *J. Chem. Phys.* **2017,** *147*, 144701.

19. Yella, A.; Lee, H.-W.; Tsao, H. N.; Yi, C.; Chandiran, A. K.; Nazeeruddin, M. K.; Diau, E. W.-G.; Yeh, C.-Y.; Zakeeruddin, S. M.; Grätzel, M., Porphyrin-Sensitized Solar Cells with Cobalt (II/III)–Based Redox Electrolyte Exceed 12 Percent Efficiency. *Science* **2011,** *334*, 629-634.

20. Bessho, T.; Zakeeruddin, S. M.; Yeh, C. Y.; Diau, E. W. G.; Grätzel, M., Highly Efficient Mesoscopic Dye-Sensitized Solar Cells Based on Donor–Acceptor Substituted Porphyrins. *Angew. Chem. int ed* **2010,** *49*, 6646-6649.

21. Negre, C. F.; Milot, R. L.; Martini, L. A.; Ding, W.; Crabtree, R. H.; Schmuttenmaer, C. A.; Batista, V. S., Efficiency of Interfacial Electron Transfer from Zn-Porphyrin Dyes Into TiO_2 Correlated to the Linker Single Molecule Conductance. *J. Phys. Chem. C* **2013,** *117*, 24462-24470.

22. Li, L.-L.; Diau, E. W.-G., Porphyrin-Sensitized Solar cells. *Chem. Soc. Rev.* **2013,** *42*, 291-304.

23. Wasielewski, M. R., Self-Assembly Strategies for Integrating Light Harvesting and Charge Separation in Artificial Photosynthetic Systems. *Acc. Chem. Res* **2009,** *42*, 1910-1921.

24. Choi, M. S.; Yamazaki, T.; Yamazaki, I.; Aida, T., Bioinspired Molecular Design of Light-Harvesting Multiporphyrin Arrays. *Angew. Chem. int ed* **2004,** *43*, 150-158.

25. Mickley Conron, S. M.; Shoer, L. E.; Smeigh, A. L.; Ricks, A. B.; Wasielewski, M. R., Photoinitiated Electron Transfer in Zinc Porphyrin–Perylenediimide Cruciforms and Their Self-Assembled Oligomers. *J. Phys. Chem. B* **2013,** *117*, 2195-2204.

26. Mozer, A. J.; Griffith, M. J.; Tsekouras, G.; Wagner, P.; Wallace, G. G.; Mori, S.; Sunahara, K.; Miyashita, M.; Earles, J. C.; Gordon, K. C., Zn− Zn Porphyrin Dimer-Sensitized Solar Cells: Toward 3-D Light Harvesting. *J. Am. Chem. Soc.* **2009,** *131*, 15621-15623.

27. Du, B.; Fortin, D.; Harvey, P. D., Singlet and Triplet Energy Transfers in Tetra-(meso-truxene) zinc (II)-and Tetra-(meso-tritruxene) zinc (II) Porphyrin and Porphyrin-Free Base Dendrimers. *Inorg. Chem.* **2011,** *50*, 11493-11505.

28. Lu, H.-P.; Tsai, C.-Y.; Yen, W.-N.; Hsieh, C.-P.; Lee, C.-W.; Yeh, C.-Y.; Diau, E. W.-G., Control of Dye Aggregation and Electron Injection for Highly Efficient Porphyrin Sensitizers Adsorbed on Semiconductor Films with Varying Ratios of Coadsorbate. *J. Phys. Chem. C* **2009,** *113*, 20990-20997.

29. Uetomo, A.; Kozaki, M.; Suzuki, S.; Yamanaka, K.-i.; Ito, O.; Okada, K., Efficient Light-Harvesting Antenna with a Multi-Porphyrin Cascade. *J. Am. Chem. Soc.* **2011,** *133*, 13276-13279.

30. Hasobe, T., Porphyrin-Based Supramolecular Nanoarchitectures for Solar Energy Conversion. *J. Phys. Chem. Lett.* **2013,** *4*, 1771-1780.

31. Hippius, C.; van Stokkum, I. H.; Gsaenger, M.; Groeneveld, M. M.; Williams, R. M.; Wuerthner, F., Sequential FRET Processes in Calix [4] Arene-Linked Orange-Red-Green Perylene Bisimide Dye Zigzag Arrays. *J. Phys. Chem. C* **2008,** *112*, 2476-2486.

32. Diring, S.; Puntoriero, F.; Nastasi, F.; Campagna, S.; Ziessel, R., Star-Shaped Multichromophoric Arrays fromBbodipy Dyes Grafted on Truxene Core. *J. Am. Chem. Soc.* **2009,** *131*, 6108-6110.

33. Fenwick, O.; Sprafke, J. K.; Binas, J.; Kondratuk, D. V.; Di Stasio, F.; Anderson, H. L.; Cacialli, F., Linear and Cyclic Porphyrin Hexamers as Near-Infrared Emitters in Organic Light-Emitting Diodes. *Nano Lett.* **2011,** *11*, 2451-2456.

34. Pandey, R. K.; Bellnier, D. A.; Smith, K. M.; Dougherty, T. J., Chlorin and Porphyrin Derivatives as Potential Photosensitizers in Photodynamic Therapy. *J. Photochem. Photobiol.* **1991,** *53*, 65-72.

35. Ethirajan, M.; Chen, Y.; Joshi, P.; Pandey, R. K., The Role of Porphyrin Chemistry in Tumor Imaging and Photodynamic Therapy. *Chem. Soc. Rev.* **2011,** *40*, 340-362.

36. O'Connor, A. E.; Gallagher, W. M.; Byrne, A. T., Porphyrin and Nonporphyrin Photosensitizers in Oncology: Preclinical and Clinical Advances in Photodynamic Therapy. *J. Photochem. Photobiol.* **2009,** *85*, 1053-1074.

37. Kessel, D.; Luguya, R.; Vicente, M. G. H., Localization and Photodynamic Efficacy of Two Cationic Porphyrins Varying in Charge Distribution. *J. Photochem. Photobiol.* **2003,** *78*, 431-435.

38. Lin, S.; Diercks, C. S.; Zhang, Y.-B.; Kornienko, N.; Nichols, E. M.; Zhao, Y.; Paris, A. R.; Kim, D.; Yang, P.; Yaghi, O. M., Covalent Organic Frameworks Comprising Cobalt Porphyrins for Catalytic CO_2 Reduction in Water. *Science* **2015,** *349*, 1208-1213.

39. Hod, I.; Sampson, M. D.; Deria, P.; Kubiak, C. P.; Farha, O. K.; Hupp, J. T., Fe-Porphyrin-Based Metal–Organic Framework Films as High Surface Concentration, Heterogeneous Catalysts for Electrochemical Reduction of CO_2. *ACS Catal.* **2015,** *5*, 6302-6309.

40. Maeda, C.; Taniguchi, T.; Ogawa, K.; Ema, T., Bifunctional Catalysts Based on m-Phenylene-Bridged Porphyrin Dimer and Trimer Platforms: Synthesis of Cyclic Carbonates from Carbon Dioxide and Epoxides. *Angew. Chem. int ed* **2015,** *54*, 134-138.

41. Omagari, T.; Suzuki, A.; Akita, M.; Yoshizawa, M., Efficient Catalytic Epoxidation in Water by Axial N-Ligand-Free Mn-Porphyrins Within a Micellar Capsule. *J. Am. Chem. Soc.* **2016,** *138*, 499-502.

42. Charvet, R.; Yamamoto, Y.; Sasaki, T.; Kim, J.; Kato, K.; Takata, M.; Saeki, A.; Seki, S.; Aida, T., Segregated and Alternately Stacked Donor/Acceptor Nanodomains in Tubular Mmorphology Tailored with Zinc Porphyrin–C60 Amphiphilic Dyads: Clear Geometrical Effects on Photoconduction. *J. Am. Chem. Soc.* **2012,** *134*, 2524-2527.

43. Yu, H.-Z.; Baskin, J. S.; Zewail, A. H., Ultrafast Dynamics of Porphyrins in the Condensed Phase: II. Zinc Tetraphenylporphyrin. *J. Phys. Chem. A* **2002,** *106*, 9845-9854.

44. Baskin, J. S.; Yu, H.-Z.; Zewail, A. H., Ultrafast Dynamics of Porphyrins in the Condensed Phase: I. Free Base Tetraphenylporphyrin. *J. Phys. Chem. A* **2002,** *106*, 9837-9844.

45. Steiger, B.; Baskin, J. S.; Anson, F. C.; Zewail, A. H., Femtosecond Dynamics of Dioxygen–Picket-Fence Cobalt Porphyrins: Ultrafast Release of O2 and the Nature of Dative Bonding. *Angew. Chem. int ed* **2000,** *39*, 257-260.

46. Yu, H.-Z.; Baskin, J. S.; Steiger, B.; Anson, F. C.; Zewail, A. H., Femtosecond Dynamics and Electrocatalysis of the Reduction of O_2: Tetraruthenated Cobalt Porphyrins. *J. Am. Chem. Soc.* **1999,** *121*, 484-485.

47. Yu, H.; Baskin, J.; Steiger, B.; Wan, C.; Anson, F.; Zewail, A., Femtosecond Dynamics of Metalloporphyrins: Electron Transfer and Energy Redistribution. *Chem. Phys. Lett.* **1998,** *293*, 1-8.

48. Shirakawa, M.; Fujita, N.; Shinkai, S., A Stable Single Piece of Unimolecularly π-Stacked Porphyrin Aggregate in a Thixotropic Low Molecular Weight Gel: A One-Dimensional Molecular Template for Polydiacetylene Wiring Up to Several Tens of Micrometers in Length. *J. Am. Chem. Soc.* **2005,** *127*, 4164-4165.

49. Ishida, Y.; Masui, D.; Shimada, T.; Tachibana, H.; Inoue, H.; Takagi, S., The Mechanism of the Porphyrin Spectral Shift on Inorganic Nanosheets: The Molecular Flattening Induced by the Strong Host–Guest Interaction Due to the “Size-Matching Rule”. *J. Phys. Chem. C* **2012,** *116*, 7879-7885.

50. Dorough, G.; Miller, J.; Huennekens, F. M., Spectra of the Metallo-Derivatives of α, β, γ, δ-Tetraphenylporphine. *J. Am. Chem. Soc.* **1951,** *73*, 4315-4320.

51. Thomas, D. W.; Martell, A. E., Absorption Spectra of para-Substituted Tetraphenylporphines1, 2. *J. Am. Chem. Soc.* **1956,** *78*, 1338-1343.

52. Pekkarinen, L.; Linschitz, H., Studies on Metastable States of Porphyrins. II. Spectra and Decay Kinetics of Tetraphenylporphine, Zinc Tetraphenylporphine and Bacteriochlorophyll1. *J. Am. Chem. Soc.* **1960,** *82*, 2407-2411.

53. Zimmerman, J. D.; Diev, V. V.; Hanson, K.; Lunt, R. R.; Yu, E. K.; Thompson, M. E.; Forrest, S. R., Porphyrin-Tape/C60 Organic Photodetectors with 6.5% External Quantum Efficiency in the Near Infrared. *Adv. Mater.* **2010,** *22*, 2780-2783.

54. Karam, T. E.; Khoury, R. A.; Haber, L. H., Excited-State Dynamics of Size-Dependent Colloidal TiO_2-Au Nanocomposites. *J. Chem. Phys.* **2016,** *144*, 124704.

55. Fita, P.; Fedoseeva, M.; Vauthey, E., Ultrafast Excited-State Dynamics of Eosin B: A Potential Probe of the Hydrogen-Bonding Properties of the Environment. *J. Phys. Chem. A* **2011,** *115*, 2465-2470.

56. Zhao, Q.; Wang, Y.; Xu, Y.; Yan, Y.; Huang, J., Out-of-Plane Coordinated Porphyrin Nanotubes with Enhanced Singlet Oxygen Generation Efficiency. *Sci. Rep.* **2016,** *6*, 31339.

Chapter 4. Ultrafast Heating and Melting Dynamics of Aluminum Thin Films Studied by Pump-Probe Reflectivity and Microscopy

4.1 Introduction

Laser additive manufacturing is a highly efficient method to produce three dimensional (3D) materials with high precision for a range of industries that include automotive, aerospace, and medical engineering.[1-3] Additive laser manufacturing has developed into a growing industry for producing 3D objects by adding individual layers of materials such as metals, plastics, or composite materials. Selective laser melting (SLM) is the most widely applied additive manufacturing technique that can be used for fabricating complex 3D structures, involving the use of a bed of powder that is refreshed after each layer is laser fused.[4-5] In this regard, lasers are the primary high energy heat source, since the laser beam can transfer a large amount of energy into the focal region for the material to undergo rapid melting and resolidification in a controlled manner. In order to fully understand and develop SLM, it is crucial to investigate the temporal dynamics of laser heating, melting, ablation, and resolidification processes on the ultrafast time scale. Previous studies have been concentrated on understanding laser-induced solid-to-liquid phase transitions of metals such as aluminum and gold using techniques such as ultrafast pump-probe reflectivity, X-ray diffraction, and X-ray near edge absorption spectroscopy.[6-8]

During the laser-material interaction, the energy of the laser pulses is absorbed by the electrons to create a pool of excited electrons. These excited electrons then diffuse through the electron gas and transfer energy into deeper parts of the metal at speeds close to the Fermi velocity ($\sim 10^6$ m/s) by ballistic motion while spreading their energy through inelastic collisions.[9-11] Concurrently, hot electron thermalization with the lattice

occurs through electron-phonon coupling. Finally, heat is released to the surrounding medium by phonon-phonon scattering.[12-14] The two-temperature model is used to describe energy flow from hot electrons to the lattice by considering the electron gas and the lattice as two interacting subsystems with different temperatures on ultrafast timescales.[15-18] Previous research has shown that an increase in electron-phonon coupling is observed due to shortening of the electron mean free path as films become thinner, and substrate interactions become more important.[19] However, other experiments contradict this generalization and highlight that more work is needed to better understand the heating and melting dynamics of metals in thin films.[20-21]

Research on the ultrafast excited-state dynamics of metallic thin film samples is of great interest not only for advancing fundamental science but also due to the impact in a wide range of applications in areas such as high reflective mirrors,[22] field-effect transistors,[23] hot-electron photochemistry,[24] and laser ablation for processing of materials.[9] During high power ultrashort laser pulse exposure, phase transitions in metal thin films can occur resulting multiple processes such as heating, melting, resolidification, and ablation. Aluminum is a commonly used material in laser-based manufacturing processes owing to its widespread technological use as a structural component.[1, 25] Additionally, it has numerous applications in areas such as metal enhanced-fluorescence,[26] nonlinear plasmonics,[27] high energy plasmonics,[28] deep UV Raman scattering,[29-30] and laser-based material processing.[2-3] The ultrafast dynamics associated with the solid-to-liquid phase transition in aluminum has been a topic of intense debate over several years, with disagreement over whether the structural transition is caused by a thermal or nonthermal process.[6, 25] Further research is required to study the laser-based

heating and melting dynamics in aluminum under varying parameters such as wavelength, power, pulse energy, and pulse duration as well as material parameters such as thickness, density, and different level of alloying.

Numerous experimental techniques have been used to investigate the relaxation dynamics of hot electrons in metals. For example, angle-resolved photoelectron spectroscopy has been utilized to determine electron-phonon coupling near surfaces.[31] Additionally, neutron diffraction has been used as a technique to evaluate phonon lifetimes.[32] Pump-probe reflectivity is a very powerful technique used to monitor the temporal evolution of electronic relaxation and scattering mechanisms after excitation with high-intensity pump pulse irradiation at the surface of bulk metals and metallic thin films. Previous ultrafast reflectivity studies of gold thin films have demonstrated the role of sample thickness on the underlying excited-state relaxation dynamics.[33-36] Additionally, previous ultrafast reflectivity investigations on NiFe alloy thin film samples have identified the importance of the underlying substrate in high laser fluence laser heating studies.[37] However, other materials such as aluminum, which have more widespread use in materials engineering, have not been studied in detail under varying thin film thicknesses using ultrafast reflectivity experiments.

In this chapter, ultrafast pump-probe reflectivity measurements are used to investigate the heating and melting dynamics of aluminum thin films for thicknesses in the range of 20 nm to 700 nm. For each sample, the power-dependent ultrafast reflectivity time traces are acquired in order to determine properties such as the electron-photon coupling lifetimes, the melting thresholds, and the magnitudes of the change in reflectivities using 800 nm pump and probe wavelengths. Additionally, the samples are

imaged using optical microscopy both before and after the laser irradiations to confirm the laser power threshold for melting, while showing that the melt area is approximately equal to the laser spot size. These results indicate that the nanomaterial thin film becomes bulk-like as the thickness becomes larger than the characteristic heat penetration depth, which is estimated to be approximately 170 nm for aluminum. At thicknesses below this length scale, the melting threshold is significantly lower in power and the electron-phonon coupling lifetimes are faster as compared to the thicker, more bulk-like thin film samples.

4.2 Experimental Section

4.2.1 Sample Preparation

The samples used in this experiment are aluminum thin films of varying thicknesses produced by sputtering onto a silica substrate, in collaboration with Dr. McPeak's research group at LSU. Aluminum thin film samples are fabricated by the thermal evaporation of aluminum pellets onto substrates at room temperature with a base pressure of 10^{-9} Torr, a working pressure of 10^{-8} Torr, and a deposition rate of 100 Å/s. By controlling the time of deposition, the thickness of the sample is varied from 20 nm to 700 nm in different batches. All films are deposited on 1×1 cm^2 soda-lime glass substrates, purchased from VWR. The glass substrates are cleaned by ultrasonication in an aqueous solution of 5% Decon 90 for 15 minutes followed by rinsing in 18.2 MΩ type 1 deionized (DI) water and drying in a N_2 stream. For precise determination of film thickness, a lithography process is used to create a step edge on an additional sample substrate. Along with the glass substrates, an extra sample of the 1×1 cm^2 silicon substrate with a stripe on the middle (made by a sharpie pen) is added to the evaporation batch. Prior to drawing the stripe, the silicon substrate is cleaned following a standard

procedure called the RCA clean method, which was developed by the Radio Corporation of America (RCA). The RCA clean method uses a preheated ultrasonicator bath at 45°C with an RCA solution which is composed of 20 mL of H_2O_2, 4 mL of NH_4OH, and 100 mL distilled water in an Erlenmeyer flask. The the RCA solution is heated to 45°C and placed in a dish with several substrates in the utrasonicator. The dish is ultrasonicated at 35 kHz for five minutes, and then an additional five minutes at 133 kHz. Next the substrates are rinsed several times with 18.2 MΩ type 1 DI water and dried in an N_2 stream. Immediately prior to loading the substrates into the vacuum chamber, the Si substrates are dipped into a 10% HF solution for ~10 s to remove the native silicon oxide**.** After Al evaporation, the metal/stripe layer is removed by sonicating the substrate in isopropyl alcohol for 10 min, creating a step edge in the sample. The substrate is then rinsed with DI water and dried in an N_2 stream. The step edge height is then measured by a Dektek profilometer to determine the thickness of the Al thin film.

4.2.2 Ultrafast Reflectivity Setup

The ultrafast reflectivity setup is depicted in Figure 4.1. The ultrafast reflectivity measurements are carried out using a 1 kHz amplified Ti:sapphire laser system that produces 75 fs pulses centered at 800 nm with an average power of 0.7 mJ/pulse. The initial laser beam is split into pump and probe beams using a half wave plate in combination with a polarizing beam splitter, providing control of the energy ratio between the pump and probe beams. The pump beam is attenuated using a variable neutral density filter and directed to the sample as an excitation source. The probe beam is attenuated to 2 mW and is used to monitor the ultrafast reflectivity of the sample under different pump powers. Both pump and probe pulses are focused and overlapped onto

the sample surface. The pump-probe delay time is controlled by retroreflecting mirrors on a computer controlled translational stage. The pump beam is modulated with a mechanical chopper that is synchronized with the laser repetition rate at 500 Hz to block every other laser pulse. The reflected probe beam is collimated and detected using a photodiode and lock-in amplifier synchronized with the chopper. Microscopy images are also acquired of the sample using a charge coupled device (CCD) camera with two lenses. Microscopy images are taken both before and after laser irradiation to determine the onset and spatial dimensions of the resulting melt size.

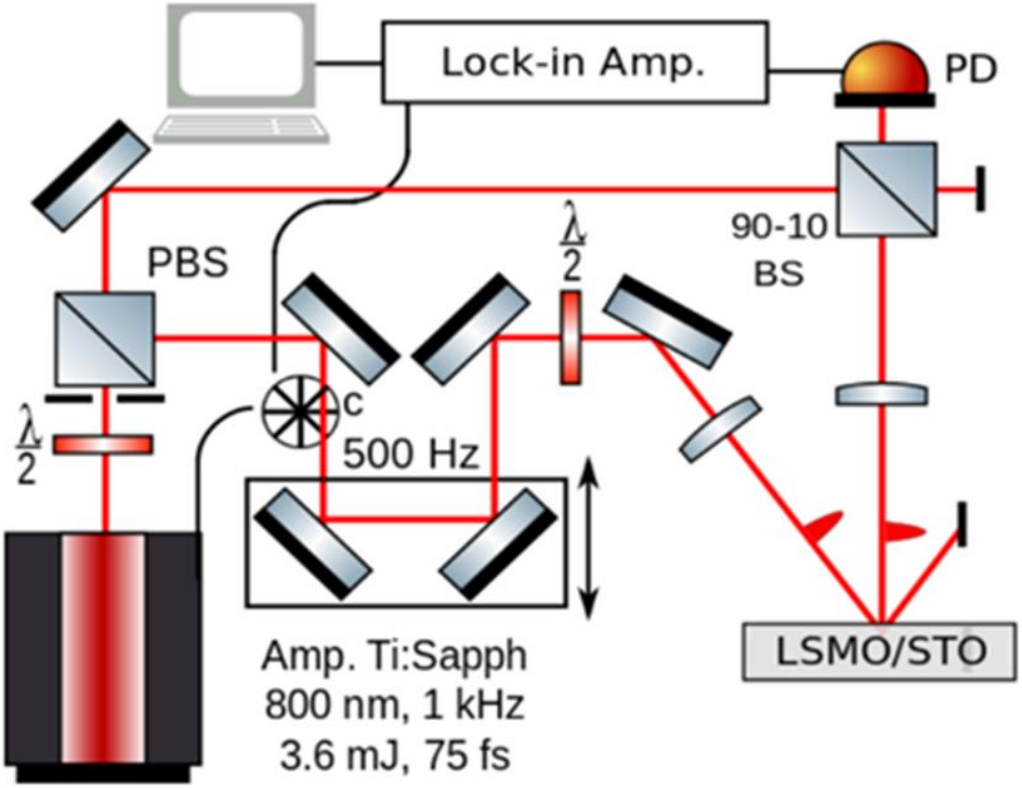

Figure 4.1. Experimental pump-probe reflectivity setup.

4.3 Results and Discussion

The heating and melting dynamics of aluminum thin film samples in the range of 20-700 nm in thickness are investigated with ultrafast reflectivity under varying pump powers. Figure 4.2 shows several representative ultrafast reflectivity time traces from a 20 nm thick aluminum thin film using 800 nm pump and probe pulses at selected pump powers. All ultrafast reflectivity time traces show zero change in reflectivity at negative time delays, corresponding to the probe pulse arriving first at the sample. Time zero corresponds to temporal overlap, where a large change in reflectivity is observed, followed by a decrease over time, tracking the metal thin film relaxation dynamics. The electron-phonon coupling lifetimes are determined by fitting the time traces using a single exponential function given by $\Delta R = A + B\,exp(-t/\tau)$, shown as solid black lines in Figure 4.2.

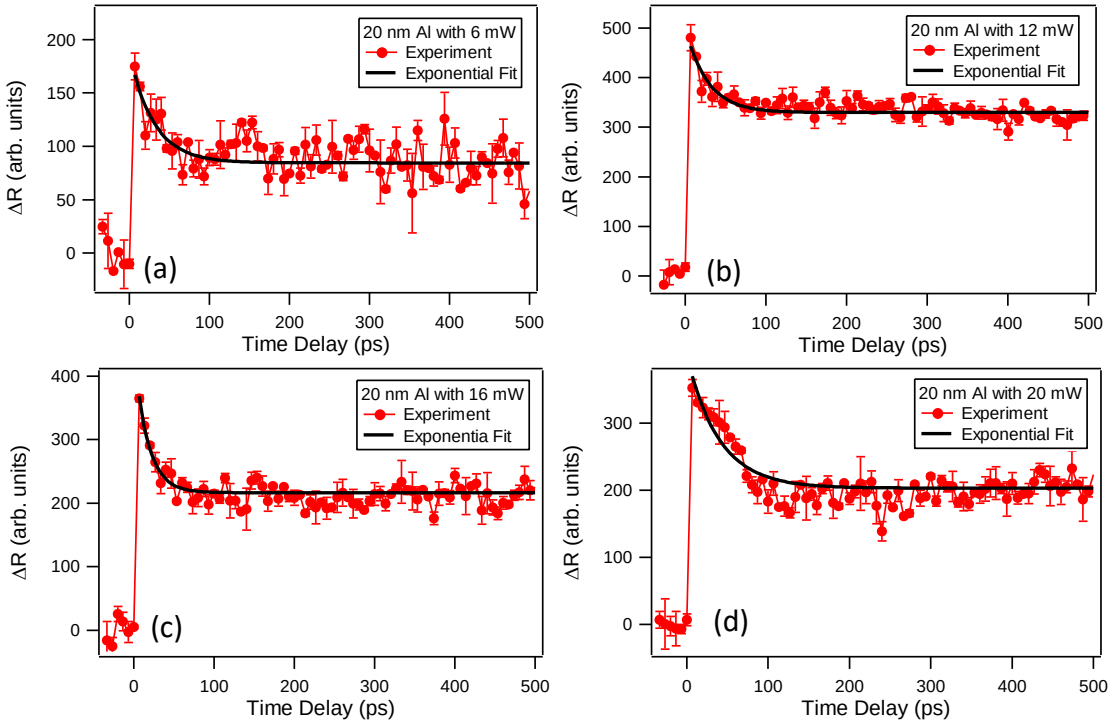

Figure 4.2. Ultrafast reflectivity time traces for 20 nm Al thin film with 800 nm at (a) 6.0, (b) 12.0, (c) 16.0, and (d) 25.0 mW pump pulse powers, respectively.

At a relatively low pump power of 6 mW, the temporal change in reflectivity is observed to be an exponential decay with a lifetime τ of 90.0 ± 14.0 ps, as shown in Figure 4.2 (a). Additionally, the amplitude of electron-phonon coupling is observed to be at a relatively low value with a B value of 102.0 ± 20.0 and an offset A of 85.0 ± 2.0. At higher pump powers of 12 and 16 mW, shown in Figures 4.2 (b) and (c), respectively, sharper exponential decays are observed. The electron-phonon coupling lifetime decreases from 28.0 ± 4.6 ps to 17.0 ± 3.3 ps, the amplitude B of electron-phonon coupling increases from 170.0 ± 21 to 225.0 ± 37, and the offset A varies from 329.0 ± 2.0 to 216.0 ± 2.0 as the pump power increases from 12 to 16 mW, respectively. By further increasing in the pump power to 25 mW, the change in reflectance is observed to drop to a lower value indicating irreversible damage in the sample surface[35] as shown in Figure 4.2 (d). However, even after these irreversible changes in the sample surface at higher powers, the exponential behavior of the time trace is still observed due to recurring heating and melting dynamics in the thin film.

Figure 4.3 shows several representative ultrafast reflectivity time traces from a 150 nm thick aluminum thin film using 800 nm pump and probe pulses at selected pump powers. Similarly, Figures 4.4 and 4.5 display several representative ultrafast reflectivity time traces from a 300 nm and 700 nm and thick aluminum thin film, respectively, at selected pump powers. Again, all time traces are fit to exponential functions given by $\Delta R = A + B\,exp(-t/\tau)$ to determine the electron-phonon coupling lifetimes τ and corresponding reflectivity values A and B.

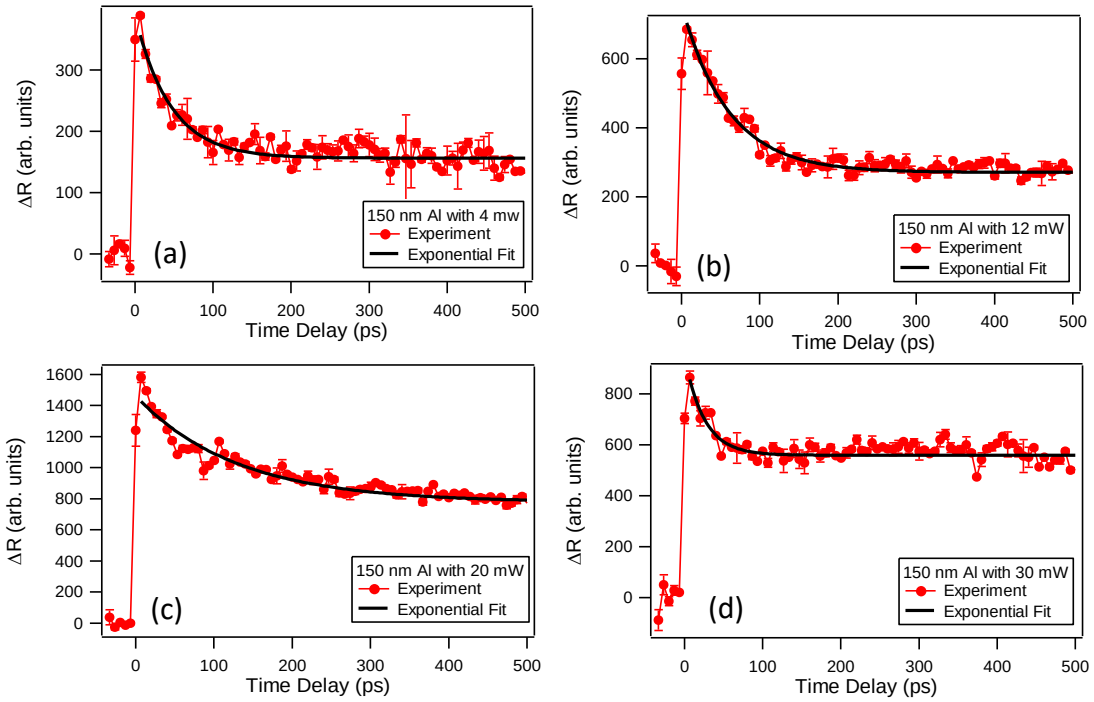

Figure 4.3. Ultrafast reflectivity time traces for 150 nm Al thin film with 800 nm at (a) 4.0, (b) 12.0, (c) 20.0, and (d) 30.0 mW pump pulse powers, respectively.

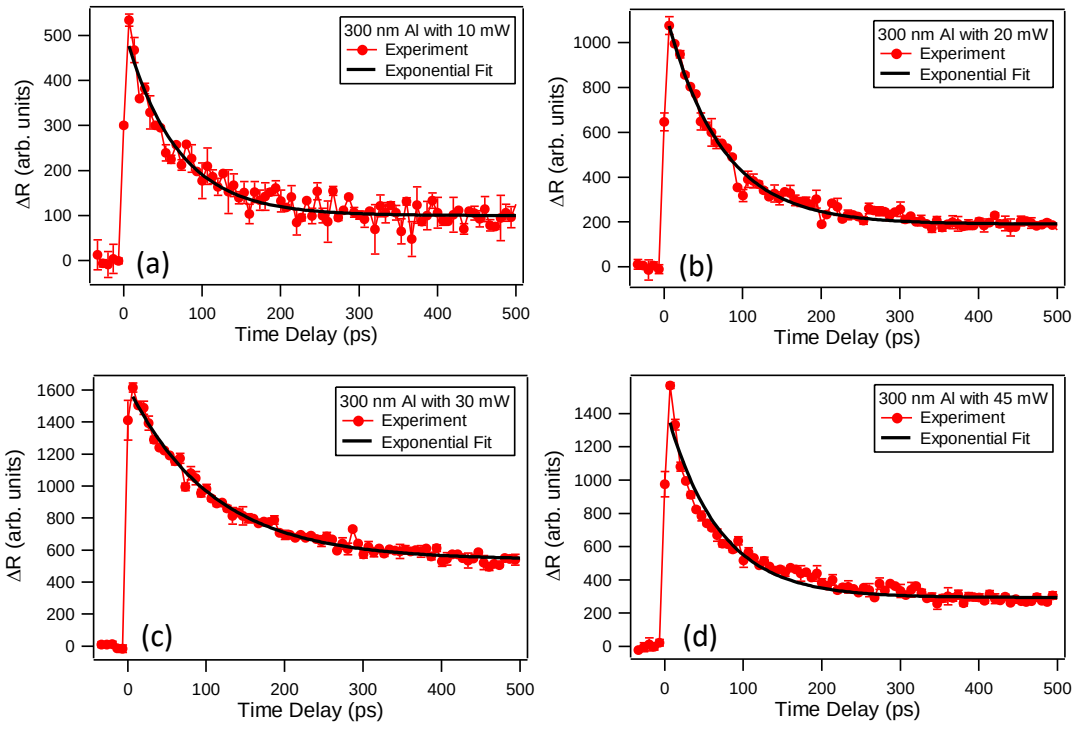

Figure 4.4. Ultrafast reflectivity time traces for 300 nm Al thin film with 800 nm at (a) 10.0, (b) 20.0, (c) 30.0, and (d) 45.0 mW pump pulse powers, respectively.

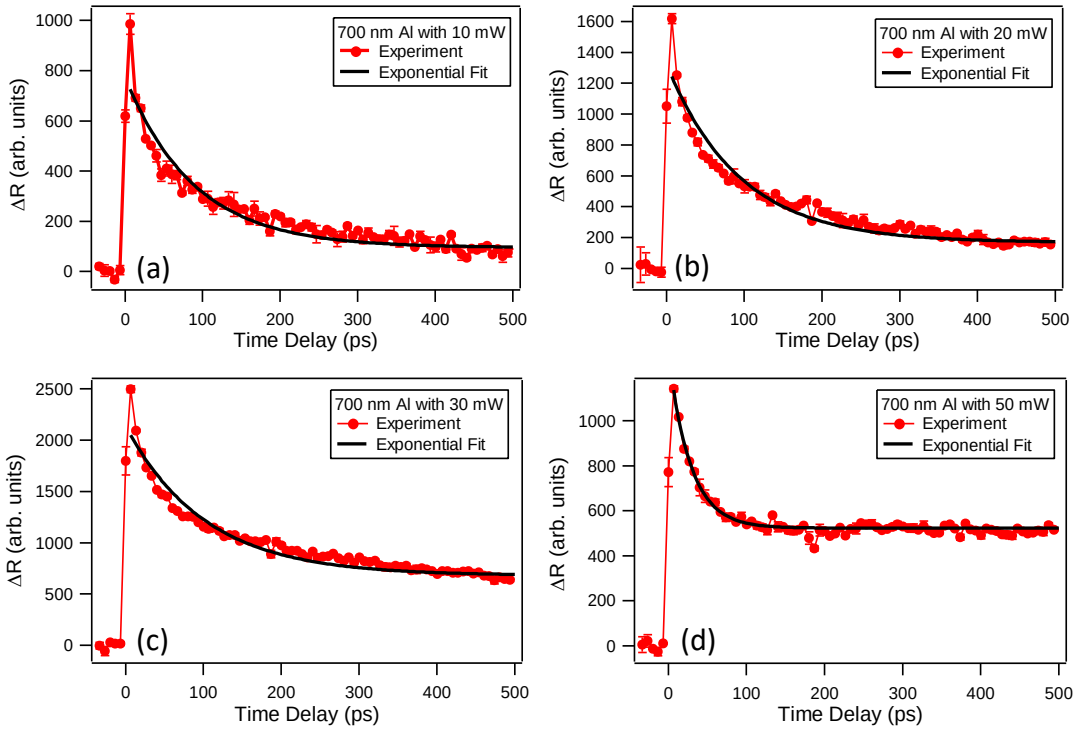

Figure 4.5. Ultrafast reflectivity time traces for 700 nm Al thin film with 800 nm at (a) 10.0, (b) 20.0, (c) 30.0, and (d) 50.0 mW pump pulse powers, respectively.

For a more detailed understanding of the power-dependent reflectivity time traces for the four Al thin film samples investigated with different thicknesses, the results of the heating and melting dynamics are directly compared in terms of the A and B reflectivity values and corresponding electron-phonon coupling lifetimes τ. Figure 4.6 shows the power-dependent reflectivity constants determined from the time traces from the different Al thin film samples. Each sample displays two distinct regions corresponding to the lower-power region before the onset of melting and the higher-power region after melting and irreversible sample damage has occurred. In the lower-power region, the sum of the reflectivity constants $A + B$ vary linearly with power up until the onset on melting. These data points are fit with linear dotted black lines for each sample, showing the linearly increasing reflectivity constants in the lower-power region before melting occurs. In this

region, the laser excitation transfers electronic population from the ground state to the excited state at time zero, where higher pump laser powers transfer larger electron populations linearly as a function of laser power resulting in corresponding linear changes in reflectivity. In the higher-power region, the onset of melting takes place and there is a deviation from the linear dependence of $A + B$ with power. In this region, the reflectivity constants decrease irreversibly since the metal thin film becomes damaged due to the laser-induced phase transition. Different sample thicknesses have different slopes of the lower-power region and different onsets of melting, as described later. Additionally, the two thinner samples of 20 and 150 nm in thickness show A and B values that are similar in intensity, while the thicker samples of 300 nm and 700 nm in thickness have significantly larger B values as compared to the corresponding A values, which will be analyzed in more detail in later sections. The samples are also investigated using microscopy both before and after the laser irradiation, showing no melting and sample damage at laser powers below the onset of melting, and clear sample damage after the onset of melting, as described later.

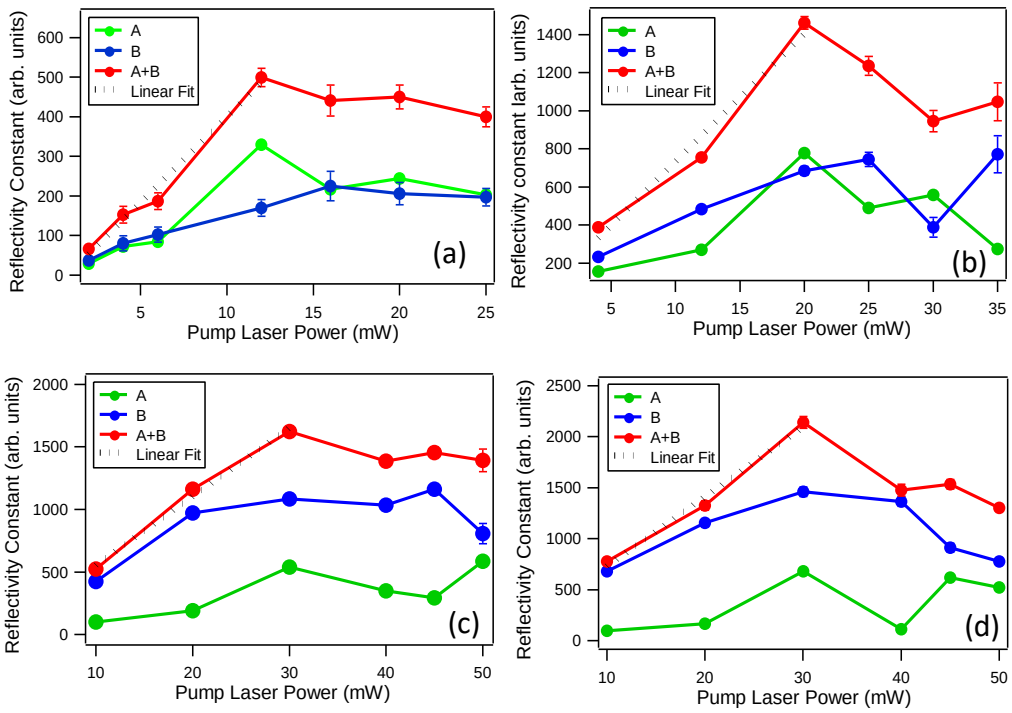

Figure 4.6. Reflectivity constant fit values as a function of pump power on Al thin film samples of thickness (a) 20, (b) 150, (c) 300, and (d) 700 nm, respectively, showing A (green), B (blue), and A+B (red) values with linear fits (dotted black line) of A+B before melting.

Figure 4.7 shows the electron-phonon coupling lifetimes as a function of the pump laser power for the four different film thicknesses. For 150, 300, and 700 nm samples, lifetimes are observed to increase with increasing laser pump power until reaching the sample damage threshold. For powers greater than the melting threshold, the lifetimes are observed to decrease as the pump power is increased. These results are in general agreement with previously reported studies for bulk-like materials that show that the relaxation times increase with increasing laser pump powers for different materials, due to lower electron-phonon coupling as the corresponding temperatures increase up until the melting threshold phase transition.[33, 38-39] However, for the very low thickness sample

of 20 nm, the trend in lifetimes with power shows a more complicated behavior, indicating a significant role of the nanomaterial interaction with the sample substrate. Additional data is required, such as repeated measurements at different thicknesses between 20 nm and 100 nm, to better understand the power-dependent electron-phonon coupling and reflectivity constant measurements in these nanomaterials.

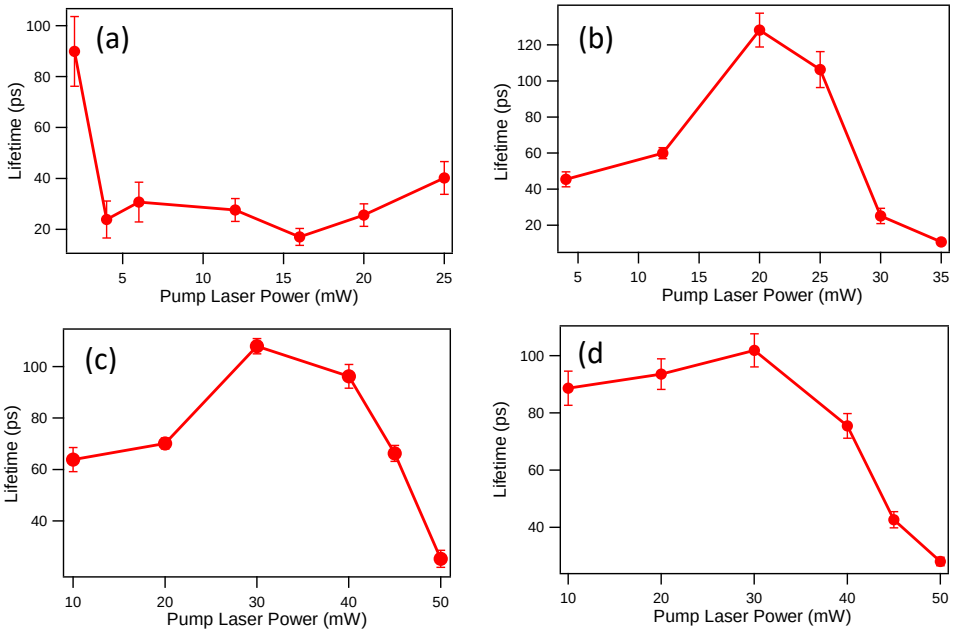

Figure 4.7. Electron-phonon coupling lifetime as a function of pump power on Al thin film samples of thickness (a) 20, (b) 150, (c) 300, and (d) 700 nm, respectively.

These ultrafast heating and melting dynamics are explained in terms of the two-temperature model, where the laser initially excites a population of electrons which rapidly thermalize to a different temperature compared to the bulk material.[40-41] At lower laser pump powers, the excited electrons return to the ground state without any irreversible changes in the sample morphology or optical properties. However, at higher laser pump powers, structural changes of the sample surface take place caused by cycles of melting and resolidification leading to irreversible chances in the sample surface chemistry and morphology.[35] However, even after melting has taken place, an exponential decay is still

apparent as cycles of melting and resolidification causes a new equilibrium with altered complex dielectric functions and a lower reflectivities.

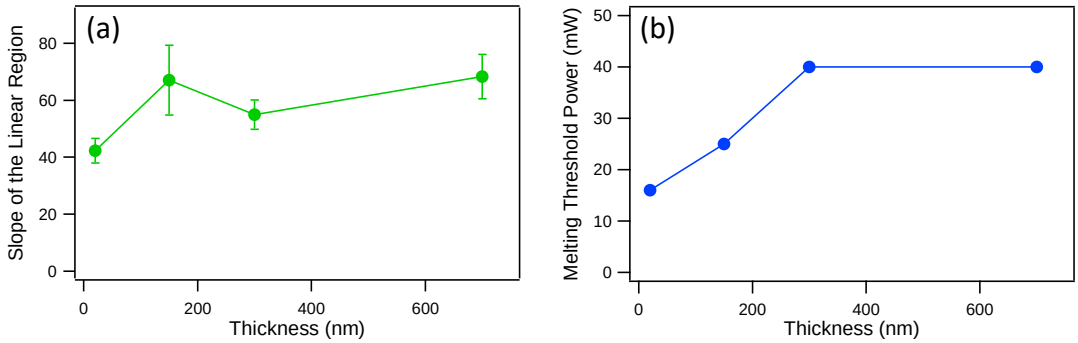

Figure 4.8. (a) Slope of the linear region and (b) melting threshold power as a function of the thickness of Al thin film samples obtained from variation of reflectivity constant with pump laser power.

Figure 4.8 summarizes the slope of the lower-power linear region and the melting threshold as a function of the thickness of the aluminum thin film samples obtained from the variations of the reflectivity constants with power. The slope of the linear region increases with increasing thickness from 20 to 150 nm and then it stays relatively constant within the standard deviation as the thickness continues to increase. Additionally, the threshold laser pump power that induces melting is shown to increase with increasing thickness from 20 to 300 nm and then the threshold power remains constant for further increases in sample thicknesses. These results suggest that aluminum thin films with a thickness of approximately 300 nm or greater behaves as a bulk-like material, while thin films of lower thickness have nanomaterial-like properties and overall heating and melting dynamics that are thickness-dependent with additional interactions with the underlying substrate. These results also point to the influence of a characteristic length scale relating to the heat penetration depth, as reported previously in gold thin films.[33]

In order to further characterize the laser-induced heating and melting, microscopy images are taken for the samples before and after laser irradiation. Additionally, the focused laser beam profiles of the probe and pump laser pulses at the sample are imaged using a white card, as shown in Figures 4.9 (a) and (b), respectively. The corresponding focal spot sizes of the probe and pump pulses are 130 and 260 μm, respectively.

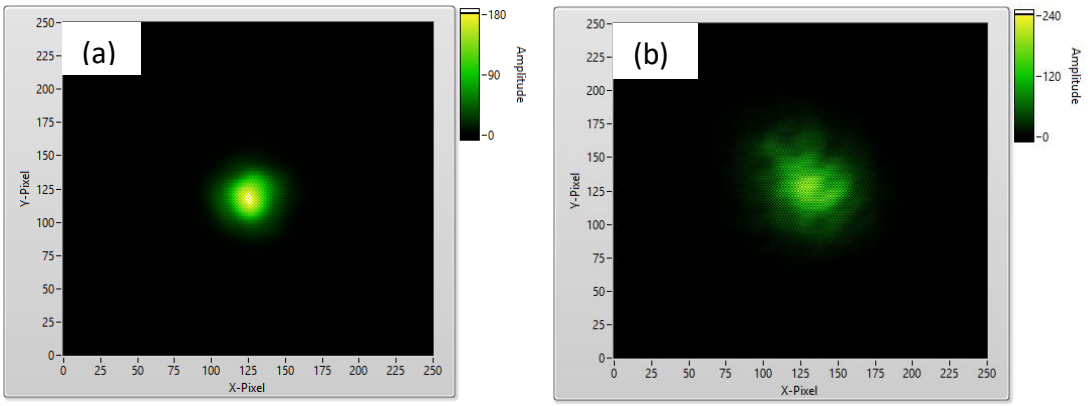

Figure 4.9. Optical microscopy image of (a) probe laser pulse and (b) pump laser pulse.

For the experiments above on aluminum thin films, no damage is observed below the melting threshold of about 16, 25, 40, and 40 mW for 20, 150, 300, and 700 nm aluminum thin film samples, respectively. Above the melting threshold, a damage spot roughly the same size as the laser focus is clearly observed. Optical microscopy images for pre-melting and post-melting conditions are shown in Figures 4.10, 4.11,4.12, and 4.13 for 20, 150, 300, and 700 nm thin film samples, respectively. Moreover, Figure 4.14 depicts additional optical microscopy images for 700 nm aluminum thin film sample for different pump laser power surveyed in this experiment. Beginning from a laser power of 40 mW the damage spot is observed.

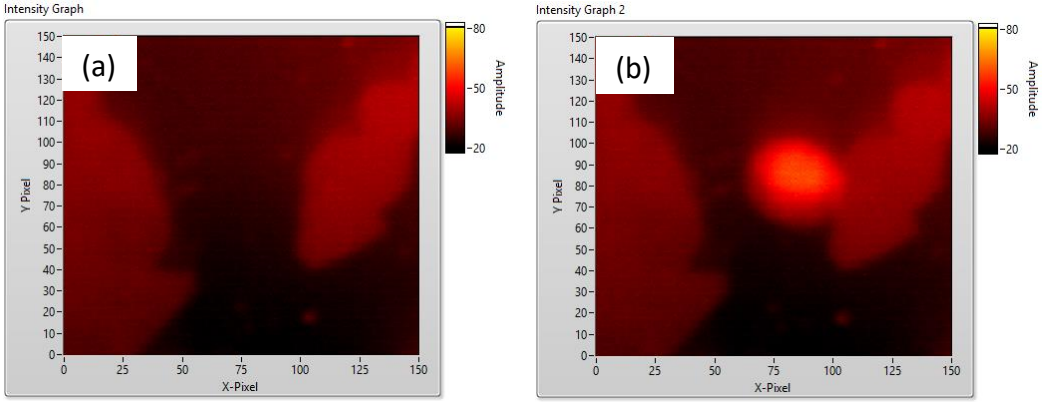

Figure 4.10. Optical microscopy image of 20 nm aluminum thin film (a) before melting and (b) after melting.

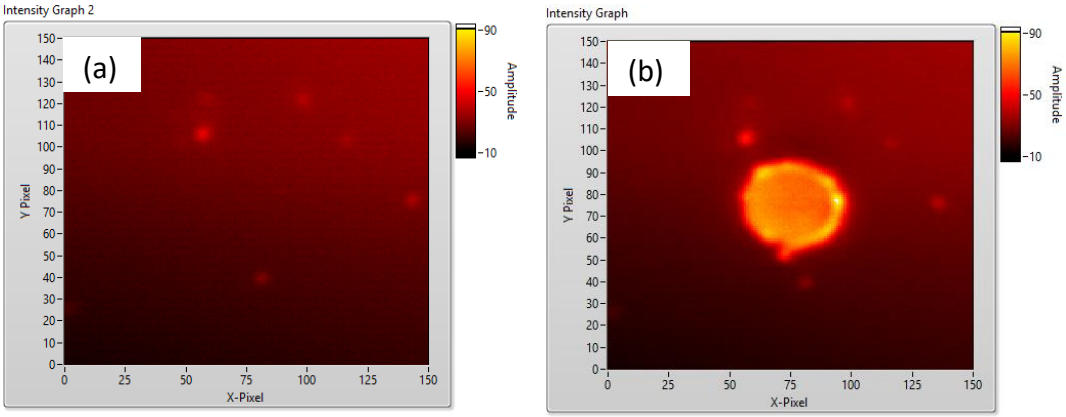

Figure 4.11. Optical microscopy image of 150 nm aluminum thin film (a) before melting and (b) after melting.

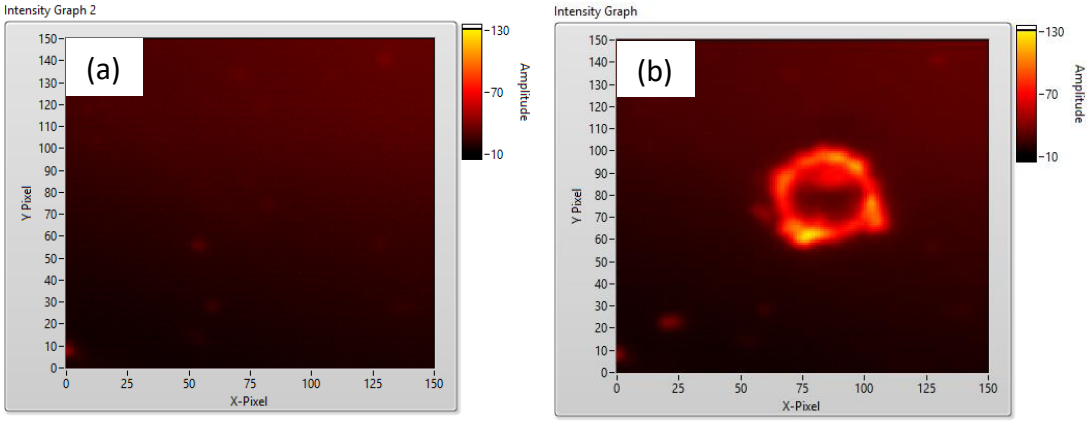

Figure 4.12. Optical microscopy image of 300 nm aluminum thin film (a) before melting and (b) after melting.

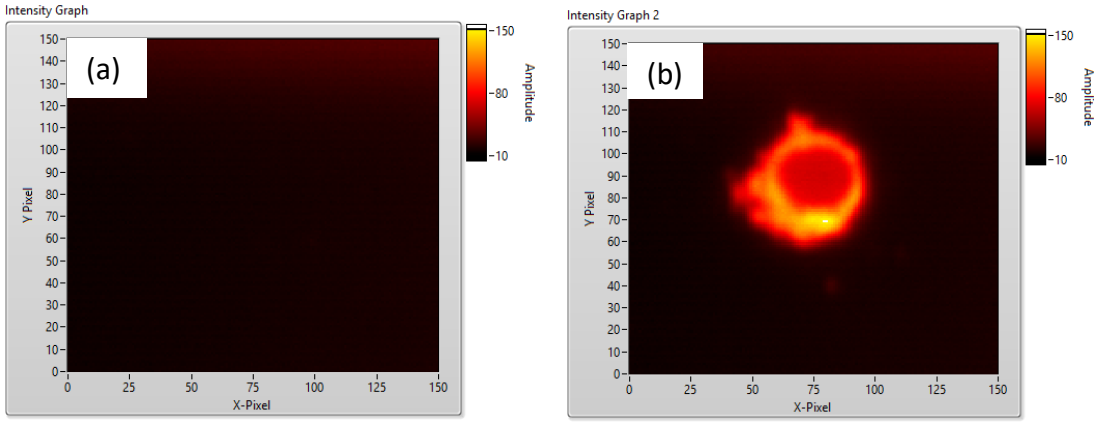

Figure 4.13. Optical microscopy image of 700 nm aluminum thin film (a) before melting and (b) after melting.

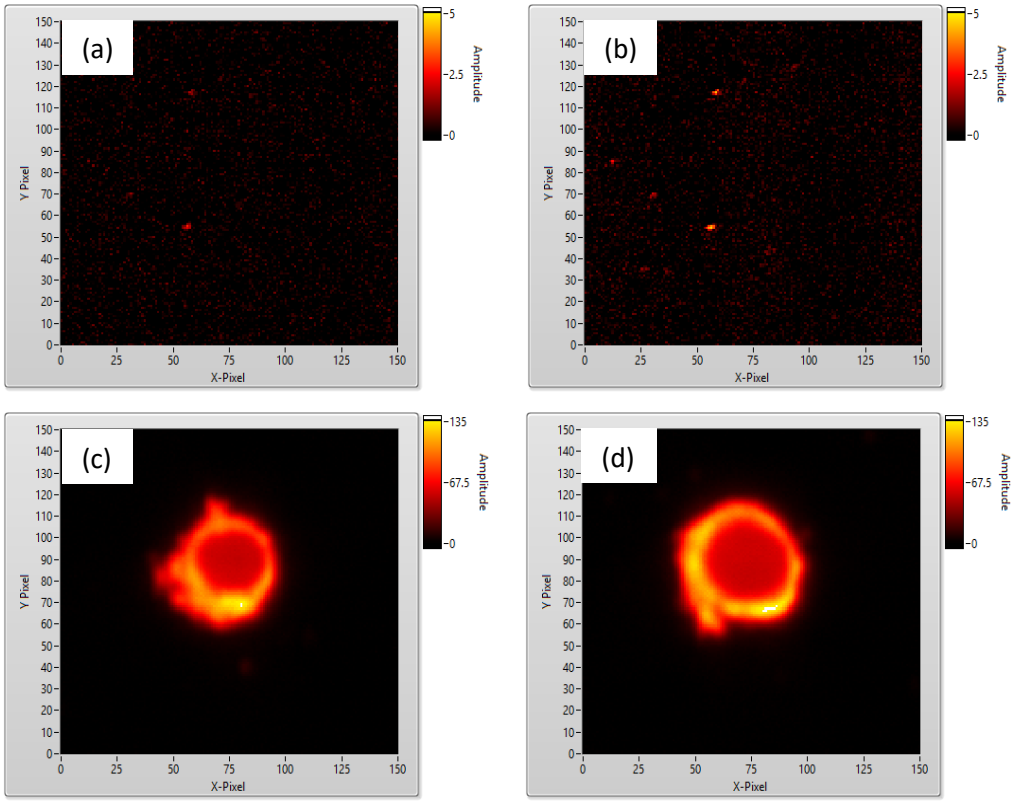

Figure 4.14. Optical microscopy image of 700 nm Al thin film using pump laser pulses at powers (a) 10, (b) 30, (c) 40, and (c) 50 mW, respectively.

The characteristic heat penetration depth of a material is important in describing the correlation between power dependence of heating and melting and the corresponding ultrafast reflectivity constants as a function of laser power and thin film thickness. The heat penetration depth is given by the equation,

$$z_0 = (128/\pi)^{1/8} (\kappa_0^2 C_l / T_m g^2 \gamma)^{1/4} \quad 4.1$$

where z_0 is heat penetration depth, κ_0 is the heat conductivity, C_l is the lattice heat capacity, T_m is the melting temperature, g is the electron-phonon coupling constant, and γ is the coefficient for electron heat capacity. Using previous estimates z_0 is expected to be approximately 170 nm for aluminum.[9, 25] This characteristic length is approximately taken to be the thickness where a thin film approaches bulk-like properties in terms of the

laser heating dynamics. For thin films of thickness much greater than the heat penetration depth, the thin film will have negligible interaction with the substrate in term of laser heating and will behave similar to the bulk material under laser irradiation. For thin films of thickness corresponding to approximately this heat penetration depth or less, the heat from the laser interaction will penetrate down to the substrate, causing thickness-dependent interactions, making the thin film behave more like a nanomaterial. In a bulk-like material, the laser heating will cause a distance-dependent gradient of temperatures from the surface into the bulk. However, when film thickness is much less than heat penetration depth, the heating will result in a more homogeneous distribution of hot carriers throughout the sample which could result from a hindered a distance-dependent temperature gradient such that the sample will behave differently compared to bulk-like materials.[33] Additionally, the heat penetration depth is related to electron-phonon relaxation time τ_R by equation,

$$L_c = \sqrt{2\,\kappa_0 \tau_R / \gamma T_l} \qquad 4.2$$

where T_l is the lattice temperature. By combining equations 4.1 and 4.2, an expression can be derived showing the relationship between the electron-phonon relaxation time and electron-phonon coupling constant. Moreover, the link between the absorbed laser fluence F_{th}, the melting temperature, and the electron-phonon coupling constant is given by the equation

$$F_{th} = (128/\pi)^{1/8} \left(\kappa_0^2 c_l^5 T_m^3 / g^2 \gamma\right)^{1/4} \qquad 4.3$$

This basic concept of heat penetration depth relating to thickness-dependent reflectivity of heating and melting in thin films has been demonstrated previously in gold nanoparticle thin films,[9] showing similar trends for our observations in aluminum thin films. Therefore,

it is of fundamental interest to study this behavior in comparison to theory in different materials in order to gain an in depth understanding on thin film ultrafast heating and melting dynamics from laser irradiation.

Future work will focus on repeating these measurements on aluminum thin film samples with additional thicknesses. Additional characterization tools such as atomic force microscopy (AFM) and ellipsometry will be employed to ensure high sample quality for all thicknesses investigated. Ellipsometry measurements will also provide data on the change in the optical properties of the sample before and after laser-induced melting occurs. The reflectivity is related to the real and imaginary part of the dielectric constant through the Fresnel equation and the change in the reflectivity is proportional to the changes in the dielectric constant upon laser excitation. Future work will also redo these measurements using different wavelengths, such as 1064 nm where SLM processing is often done, and will investigate different metal and metal alloy materials. This work will significantly help advance our fundamental understanding of laser-metal heating and melting dynamics in nanomaterials.

4.4 Conclusion

The ultrafast pump-probe reflectivity of aluminum thin films are measured under varying pump laser powers and with different thicknesses varying from 20 nm to 700 nm to determine the heating and melting dynamics. The results are consistent with the two-temperature model, which treats the electrons and the metal lattice as two distinct, interacting subsystems with different temperatures on the ultrafast timescale. The data reveal a dramatic change in the carrier relaxation mechanism for thin films of thickness below the characteristic heat penetration depth of approximately 170 nm, where

thicknesses above this value have more bulk-like properties. Electron-phonon coupling lifetimes are shown to exhibit a pronounced thickness dependence as a function of pump laser power. These studies are of fundamental importance for understanding laser heating and melting processes for metal and metal alloy nanomaterials and for potential advances of selective laser melting in additive laser manufacturing.

4.5 Notes

1. Guo, N.; Leu, M. C., Additive Manufacturing: Technology, Applications and Research Needs. *Front. Mech. Eng.* **2013,** *8*, 215-243.

2. Herzog, D.; Seyda, V.; Wycisk, E.; Emmelmann, C., Additive Manufacturing of Metals. *Acta Mater.* **2016,** *117*, 371-392.

3. Ngo, T. D.; Kashani, A.; Imbalzano, G.; Nguyen, K. T.; Hui, D., Additive Manufacturing (3D printing): A Review of Materials, Methods, Applications and Challenges. *Compos. B Eng.* **2018,** *143*, 172-196.

4. Yap, C. Y.; Chua, C. K.; Dong, Z. L.; Liu, Z. H.; Zhang, D. Q.; Loh, L. E.; Sing, S. L., Review of Selective Laser Melting: Materials and Applications. *Appl. Phys. Rev.* **2015,** *2*, 041101.

5. Yadroitsev, I.; Bertrand, P.; Smurov, I., Parametric Analysis of the Selective Laser Melting Process. *Appl. Surf. Sci.* **2007,** *253*, 8064-8069.

6. Kandyla, M.; Shih, T.; Mazur, E., Femtosecond Dynamics of the Laser-Induced Solid-to-Liquid Phase Transition in Aluminum. *Phys. Rev. B* **2007,** *75*, 214107.

7. Ernstorfer, R.; Harb, M.; Hebeisen, C. T.; Sciaini, G.; Dartigalongue, T.; Miller, R. D., The Formation of Warm Dense Matter: Experimental Evidence for Electronic Bond Hardening in Gold. *Science* **2009,** *323*, 1033-1037.

8. Leguay, P.; Lévy, A.; Chimier, B.; Deneuville, F.; Descamps, D.; Fourment, C.; Goyon, C.; Hulin, S.; Petit, S.; Peyrusse, O., Ultrafast Short-Range Disordering of Femtosecond-Laser-Heated Warm Dense Aluminum. *Phys. Rev. Lett.* **2013,** *111*, 245004.

9. Wellershoff, S.-S.; Hohlfeld, J.; Güdde, J.; Matthias, E., The Role of Electron–Phonon Coupling in Femtosecond Laser Damage of Metals. *Appl. Phys. A* **1999,** *69*, S99-S107.

10. Hopkins, P. E.; Kassebaum, J. L.; Norris, P. M., Effects of Electron Scattering at Metal-Nonmetal Interfaces on Electron-Phonon Equilibration in Gold Films. *J. Appl. Phys.* **2009,** *105*, 023710.

11. Hopkins, P. E.; Norris, P. M., Contribution of Ballistic Electron Transport to Energy Transfer During Electron-Phonon Nonequilibrium in Thin Metal Films. *J. Heat Transfer* **2009,** *131*, 043208.

12. Besteiro, L. V.; Yu, P.; Wang, Z.; Holleitner, A. W.; Hartland, G. V.; Wiederrecht, G. P.; Govorov, A. O., The Fast and the Furious: Ultrafast Hot Electrons in Plasmonic Metastructures. Size and Structure Matter. *Nano Today* **2019,** *27*, 120-145.

13. Hartland, G. V., Optical Studies of Dynamics in Noble Metal Nanostructures. *Chem. Rev.* **2011,** *111*, 3858-3887.

14. Hartland, G. V., Measurements of the Material Properties of Metal Nanoparticles by Time-Resolved Spectroscopy. *Phys. Chem. Chem. Phys.* **2004,** *6*, 5263-5274.

15. Anisimov, S.; Kapeliovich, B.; Perelman, T., Electron Emission from Metal Surfaces Exposed to Ultrashort Laser Pulses. *Zh. Eksp. Teor. Fiz* **1974,** *66*, 375-377.

16. Jiang, L.; Tsai, H.-L., A Plasma Model Combined with an Improved Two-Temperature Equation for Ultrafast Laser Ablation of Dielectrics. *J. Appl. Phys.* **2008,** *104*, 093101.

17. Jiang, L.; Tsai, H.-L., Improved Two-Temperature Model and its Application in Ultrashort Laser Heating of Metal Films. *J. Heat Transfer* **2005,** *127*, 1167-1173.

18. Fang, R.; Zhang, D.; Wei, H.; Li, Z.; Yang, F.; Gao, Y., Improved Two-Temperature Model and Its Application in Femtosecond Laser Ablation of Metal Target. *Laser Part.Beams* **2010,** *28*, 157-164.

19. Elsayed-Ali, H.; Juhasz, T.; Smith, G.; Bron, W., Femtosecond Thermoreflectivity and Thermotransmissivity of Polycrystalline and Single-Crystalline Gold Films. *Phys. Rev. B* **1991,** *43*, 4488.

20. Hohlfeld, J.; Wellershoff, S.-S.; Güdde, J.; Conrad, U.; Jähnke, V.; Matthias, E., Electron and Lattice Dynamics Following Optical Excitation of Metals. *Chem. Phys.* **2000,** *251*, 237-258.

21. Smith, A. N.; Norris, P. M., Influence of Intraband Transitions on the Electron Thermoreflectance Response of Metals. *Appl. Phys. Lett.* **2001,** *78*, 1240-1242.

22. Qiu, T.; Tien, C., Femtosecond Laser heating of Multi-Layer Metals—I. Analysis. *Int. J. Heat Mass Transf.* **1994,** *37*, 2789-2797.

23. Majumdar, A.; Fushinobu, K.; Hijikata, K., Effect of Gate Voltage on Hot-Electron and Hot Phonon Interaction and transport in a Submicrometer Transistor. *J. Appl. Phys.* **1995,** *77*, 6686-6694.

24. Gadzuk, J., Resonance-Assisted Hot Electron Femtochemistry at Surfaces. *Phys. Rev. Lett.* **1996,** *76*, 4234.

25. Guo, C.; Rodriguez, G.; Lobad, A.; Taylor, A., Structural Phase Transition of Aluminum Induced by Electronic Excitation. *Phys. Rev. Lett.* **2000,** *84*, 4493.

26. Ray, K.; Chowdhury, M. H.; Lakowicz, J. R., Aluminum Nanostructured Films as Substrates for Enhanced Fluorescence in the Ultraviolet-Blue Spectral Region. *Anal. Chem.* **2007,** *79*, 6480-6487.

27. Castro-Lopez, M.; Brinks, D.; Sapienza, R.; van Hulst, N. F., Aluminum for Nonlinear Plasmonics: Resonance-Driven Polarized Luminescence of Al, Ag, and Au Nanoantennas. *Nano Lett.* **2011,** *11*, 4674-4678.

28. Bisio, F.; Proietti Zaccaria, R.; Moroni, R.; Maidecchi, G.; Alabastri, A.; Gonella, G.; Giglia, A.; Andolfi, L.; Nannarone, S.; Mattera, L., Pushing the High-Energy Limit of Plasmonics. *ACS Nano* **2014,** *8*, 9239-9247.

29. Jha, S. K.; Ahmed, Z.; Agio, M.; Ekinci, Y.; Löffler, J. r. F., Deep-UV Surface-enhanced Resonance Raman Scattering of Adenine on Aluminum Nanoparticle Arrays. *J. Am. Chem. Soc.* **2012,** *134*, 1966-1969.

30. Dörfer, T.; Schmitt, M.; Popp, J., Deep-UV Surface-Enhanced Raman Scattering. *J. Raman Spectrosc.* **2007,** *38*, 1379-1382.

31. Plummer, E.; Shi, J.; Tang, S.-J.; Rotenberg, E.; Kevan, S., Enhanced Electron–Phonon Coupling at Metal Surfaces. *Prog. Surf. Sci.* **2003,** *74*, 251-268.

32. Stedman, R.; Almqvist, L.; Nilsson, G., Phonon-Frequency Distributions and Heat Capacities of Aluminum and Lead. *Phys. Rev.* **1967,** *162*, 549.

33. Hohlfeld, J.; Müller, J.; Wellershoff, S.-S.; Matthias, E., Time-Resolved Thermoreflectivity of Thin Gold Films and Its Dependence on Film Thickness. *Appl. Phys. B* **1997,** *64*, 387-390.

34. Hopkins, P. E.; Norris, P. M., Substrate Influence in Electron–Phonon Coupling Measurements in Thin Au Films. *Appl. Surf. Sci.* **2007,** *253*, 6289-6294.

35. Guo, C.; Taylor, A. J., Ultrafast Electronic Disorder in Heat-Induced Structural Deformations and Phase Transitions in Metals. *Phys. Rev. B* **2000,** *62*, 5382.

36. Hostetler, J. L.; Smith, A. N.; Czajkowsky, D. M.; Norris, P. M., Measurement of the Electron-Phonon Coupling Factor Dependence on Film Thickness and Grain Size in Au, Cr, and Al. *Appl. Opt.* **1999,** *38*, 3614-3620.

37. Bosco, C.; Azevedo, A.; Acioli, L., Substrate Dependent Ultrafast Dynamics in Thin NiFe Films. *Appl. Phys. Lett.* **2003,** *83*, 1767-1769.

38. Sun, C.-K.; Vallée, F.; Acioli, L.; Ippen, E.; Fujimoto, J., Femtosecond-Tunable Measurement of Electron Thermalization in Gold. *Phys. Rev. B* **1994,** *50*, 15337.

39. Sun, C.-K.; Vallee, F.; Acioli, L.; Ippen, E.; Fujimoto, J., Femtosecond Investigation of Electron Thermalization in Gold. *Phys. Rev. B* **1993,** *48*, 12365.

40. Bonn, M.; Denzler, D. N.; Funk, S.; Wolf, M.; Wellershoff, S.-S.; Hohlfeld, J., Ultrafast Electron Dynamics at Metal Surfaces: Competition Between Electron-Phonon Coupling and Hot-Electron Transport. *Phys. Rev. B* **2000,** *61*, 1101.

41. Chen, J.; Tzou, D.; Beraun, J., A Semiclassical Two-Temperature Model for Ultrafast Laser Heating. *Int. J. Heat Mass Transf.* **2006,** *49*, 307-316.

Appendix A. Monitoring the Growth Dynamics of Colloidal Gold-Silver Core-Shell Nanoparticles Using *in Situ* Second Harmonic Generation and Extinction Spectroscopy

A.1 Additional Nanoparticle Characterization Details

Figure A.1 shows a representative transmission electron microscopy (TEM) image of the gold seed nanoparticles and the corresponding extinction spectrum. Using Mie theory with error analysis, the concentration of the gold seed solution is determined to be $(4.4 \pm 1.0) \times 10^{11}$ nanoparticles/mL. Figures A.2, A.3, and A.4 show additional representative TEM images of gold-silver core-shell (Au@Ag) nanoparticles prepared using 27.5, 22.5, and 17.5 μL of precursor gold seeds, respectively, shown in order of increasing nanoparticle size, where the growth processes are monitored using *in situ* second harmonic generation (SHG) and extinction spectroscopy. The TEM images are taken using a JEOL-1400 microscope with carbon-coated copper grids. The nanoparticle size histograms are determined from the TEM images, with the results shown in Figure A5. The size histograms are fit to log-normal functions, which are indicated by dotted lines in Figure A.5. The sizes obtained from the fits are 13.8 ± 1.2 nm for the gold seeds, and 51.0 ± 7.1 nm, 65.8 ± 9.2 nm, and 77.7 ± 8.6 nm for the gold-silver core-shell nanoparticles prepared with 27.5, 22.5, and 17.5 μL precursor gold seeds, respectively.

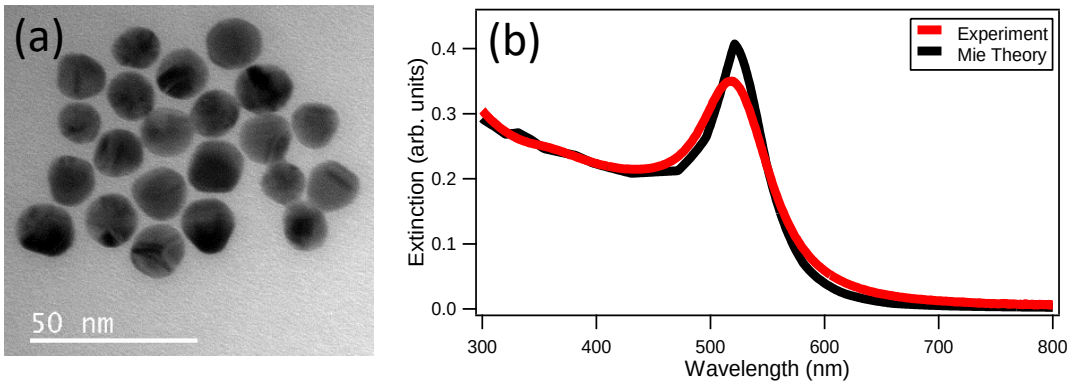

Figure A.1. (a) Representative TEM image of gold seed nanoparticles and (b) the measured extinction spectrum (red line) of gold seed nanoparticles compared to Mie theory (black line).

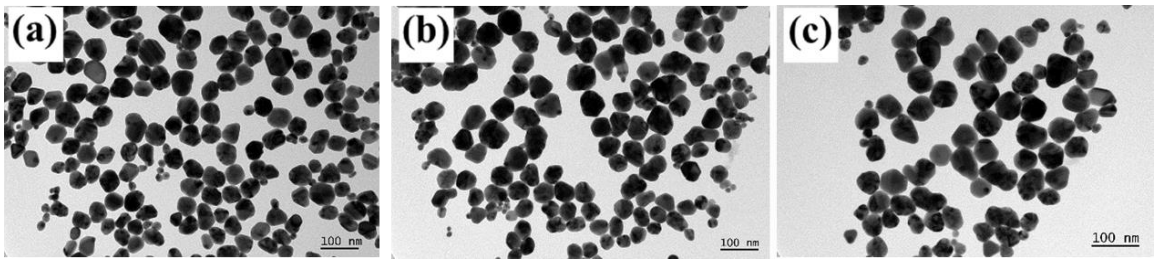

Figure A.2. Additional TEM images of gold-silver core-shell nanoparticles prepared using 27.5 µL precursor seeds.

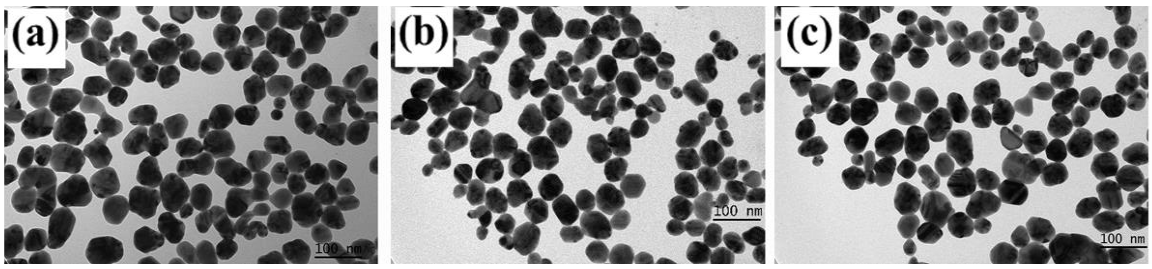

Figure A.3. Additional TEM images of gold-silver core-shell nanoparticles prepared using 22.5 µL precursor seeds.

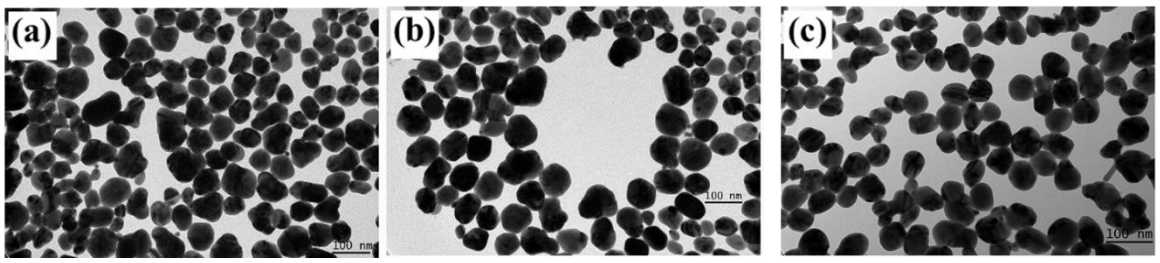

Figure A.4. Additional TEM images of gold-silver core-shell nanoparticles prepared using 17.5 µL precursor seeds.

A.2 Additional Results from *In Situ* Second Harmonic Generation and Extinction Spectroscopy

The in situ SHG and extinction spectroscopy setup is shown in Figure A.6 and is modified from our previous work. Figures A.7 (a) and (b) show the SHG spectra at selected reaction times during the nanoparticle growth process for the 51 nm and 66 nm gold-silver core-shell nanoparticles, respectively. The lower level of noise in the last SHG spectra is due to five-times longer acquisition times. Figure A.8 shows the peak SHG electric field as a function of final nanoparticle diameter. The larger gold-silver core-shell nanoparticles show a higher peak SHG electric field, which is consistent with our previous SHG studies from seed-mediated gold nanoparticles.[1]

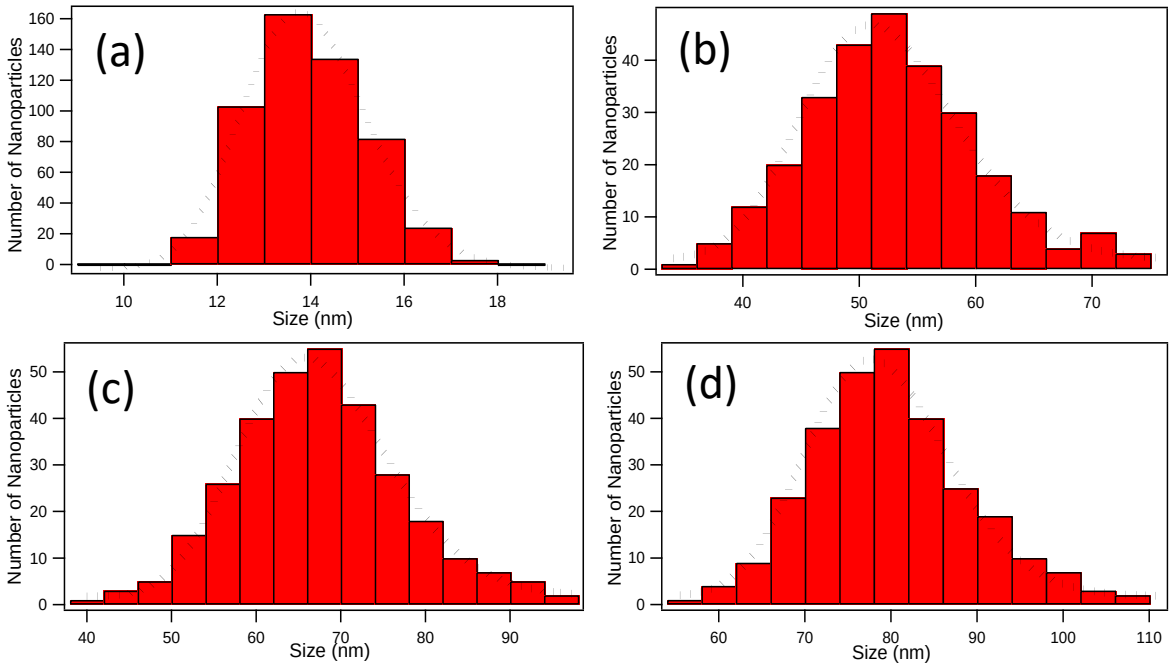

Figure A.5. Size distribution histograms for (a) gold seed nanoparticles and gold-silver core-shell nanoparticles prepared with (b) 27.5 µL, (c) 22.5 µL, and (d) 17.5 µL precursor gold seeds, respectively, with corresponding log-normal fits (dotted lines).

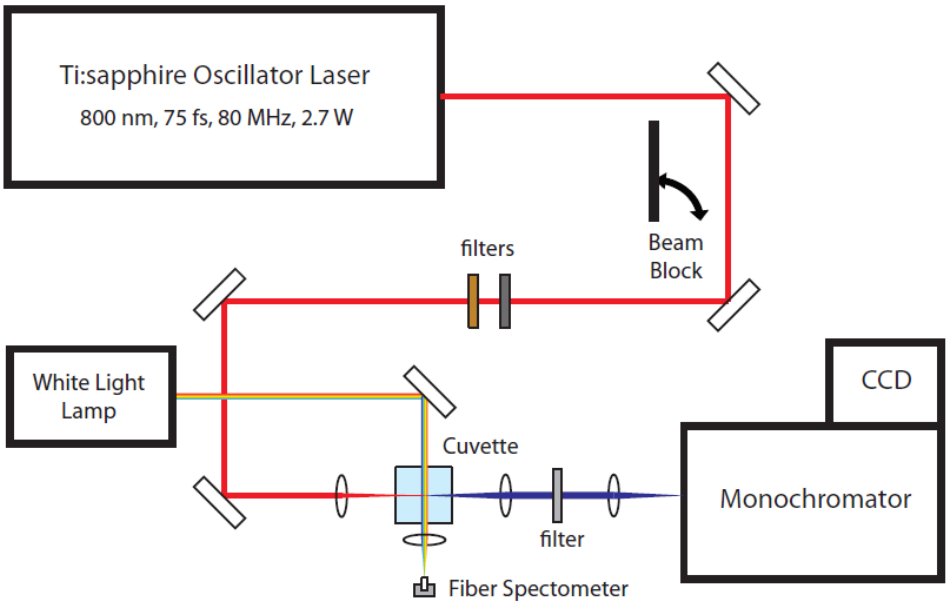

Figure A.6. In-situ SHG and extinction spectroscopy experimental setup.

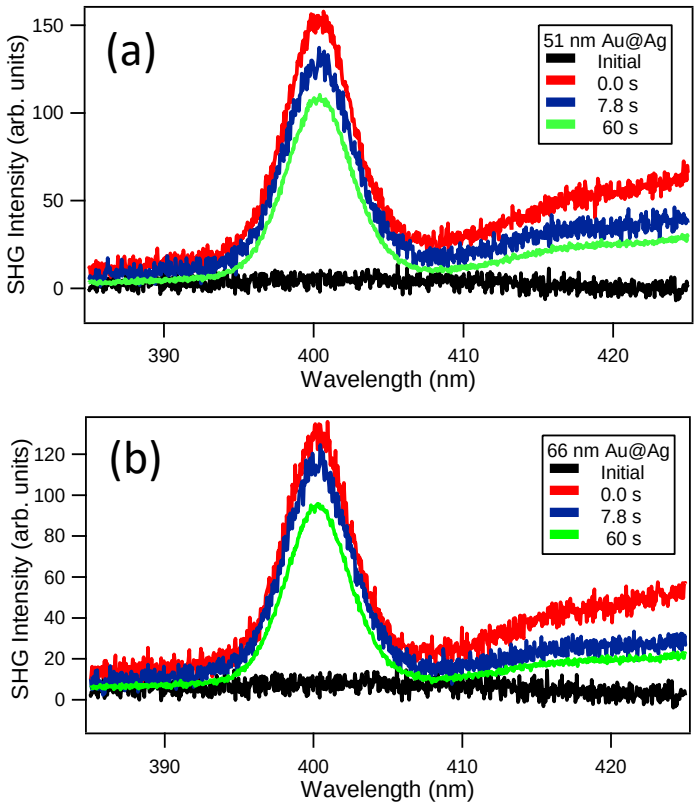

Figure A.7. SHG spectra during different reaction times for the (a) 51 nm and (b) 66 nm colloidal gold-silver core-shell nanoparticles.

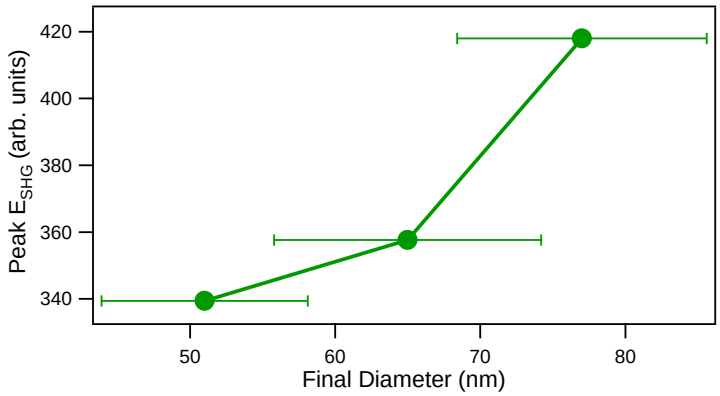

Figure A.8. Peak SHG electric field as a function of final gold-silver core-shell nanoparticle diameter.

The peak intensity from the *in situ* extinction spectroscopy of the gold-silver core-shell nanoparticles as a function of reaction time are fit using an exponential function, as described in Chapter 2. Table A.1 shows the tabulated offsets B, amplitudes A, and lifetimes τ_{ext} from the corresponding fits.

Table A.1. Fitting parameters obtained from the *in situ* extinction spectroscopy peak intensities as a function of reaction time for the different core-shell nanoparticles.

Final Diameter (nm)	**Offset B**	**Amplitude A**	**Lifetime τ_{ext} (s)**
51.0 ± 7.1	0.817 ± 0.002	-0.45 ± 0.01	5.2 ± 0.2
65.8 ± 9.2	0.750 ± 0.002	-0.66 ± 0.01	5.3 ± 0.2
77.7 ± 8.6	0.758 ± 0.001	-0.30 ± 0.01	6.2 ± 0.1

The *in situ* SHG electric field as a function of reaction time for the different core-shell nanoparticles are fit using a biexponential function, as described in Chapter 2. Table A.2 shows the tabulated offsets B_{SHG}, amplitudes A_1 and A_2, the fast SHG lifetimes τ_1, and the slow SHG lifetimes τ_2 from the corresponding fits.

Table A.2. Fitting parameters obtained from the *in situ* SHG electric field as a function of reaction time for the different core-shell nanoparticles.

Final Diameter (nm)	**Offset B_{SHG}**	**Amplitude A_1**	**Amplitude A_2**	**Fast SHG Lifetime τ_1 (s)**	**Slow SHG Lifetime τ_2 (s)**
51.0 ± 7.1	259.0 ± 0.4	40.3 ± 1.0	40.2 ± 1.9	4.6 ± 0.5	175 ± 9
65.8 ± 9.2	276.4 ± 0.3	29.8 ± 0.6	51.3 ± 1.0	6.4 ± 0.2	239 ± 17
77.7 ± 8.6	306.1 ± 0.5	36.9 ± 1.1	91.9 ± 2.2	10.0 ± 0.4	268 ± 10

Figure A.9 shows the final normalized experimental extinction spectra for the three different gold-silver core-shell nanoparticle samples used in this study. Note that these extinction spectra are reproduced from Figure 2.4 (a)-(c) in chapter 2, shown on the same graph for direct comparison.

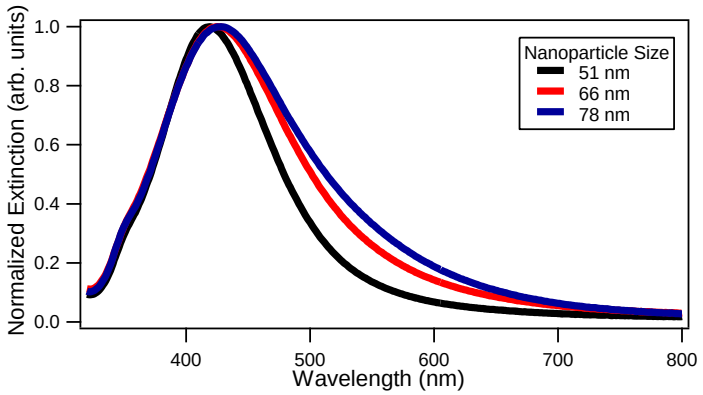

Figure A.9. Final normalized experimental extinction spectra for the 51 nm (black line), 66 nm (red line), and 78 nm (blue line) gold-silver core-shell nanoparticles.

A.3 Additional Details on the Finite-Difference Time-Domain Calculations

In order to simulate the extinction cross sections of these systems, we use an in-house developed finite-difference time-domain code, which was first used in the calculation of plasmonic response in dye monolayers on metal nanoparticles in our group.[2] In short, this method uses finite differences in time and distance to solve Maxwell's equations. For the gold and silver frequency-dependent permittivities, we use Neuhauser's 7 and 9 pole fit, respectively, to the experimental bulk data taken from 0.60 eV = 2066 nm to 6.69 eV = 185 nm.[3] The extinction spectra were computed from the sum of the absorption and scattering cross sections. The system was excited using a plane wave which is a discrete Ricker wavelet pulse with pulse width of 0.405 fs centered at 3.20 eV. The absorption was computed via a flux monitor located inside a total

field/scattered field (TFSF) interface, and the scattering cross-section was computed using a near-to-far field transform outside the TFSF.

Polydispersity in the core and shell sizes necessitates simulating the extinction for a range of particle geometries. In experiment, the observed range of diameters for the gold core is 13.8 ± 1.0 nm. To first determine the effect of the polydispersity of the core, we computed the spectra of a single gold nanospheres in water with diameters of 12.8 nm, 13.8 nm, 14.8 nm. Here, the grid space was taken to be 10 au = 0.53 nm, the total grid number was taken to be $100^3 = 10^6$, the time step was chosen to be 0.067 au = 1.62 × 10^{-3} fs so that the Courant-Friedrichs-Lewy (CFL) stability condition equals to 0.8. The resulting spectra are shown in Fig. A.10, which demonstrates that core size has little effect on the plasmon frequency. For comparison, the computed extinction peak of gold nanospheres is 529.35nm, which is about (2%) red-shifted with respect to experiment.

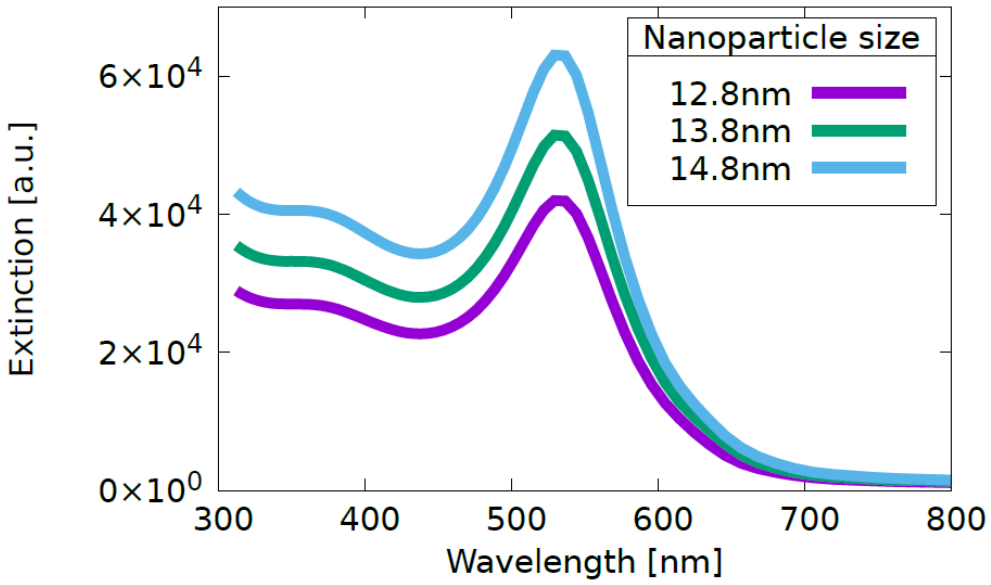

Figure A.10. Calculated Extinction Spectra of single Gold Nanospheres in water with diameters of 12.8nm, 13.8nm and 14.8nm.

Next, we consider Ag shell-only spectra for core diameters of 12.8 nm, 13.8 nm, and 14.8 nm, and total particle diameters of 38.0 nm and 87.8 nm. Here we treat the cores as vacuum, while the entire shell is in water. The grid space was taken to be 20 au = 1.06 nm, the time step was chosen to be 0.067 au = 1.62×10^{-3} fs, and the total grid number was taken to be $150^3 = 3.375 \times 10^6$ for 38.0 nm particles and $300^3 = 2.7 \times 10^7$ for 87.8 nm particles. The results are shown in Fig. A.11 and Fig. A.12. This shows that for a given particle diameter, varying the core diameter has negligible effect on the extinction. Additionally, the maximum extinction of these silver shells is roughly three order of magnitude greater than that of the Au core. Based on these results, it is clear that the polydispersity of the core does not need to be explicitly considered, and thus all subsequent calculations used a single core diameter of 13.8 nm.

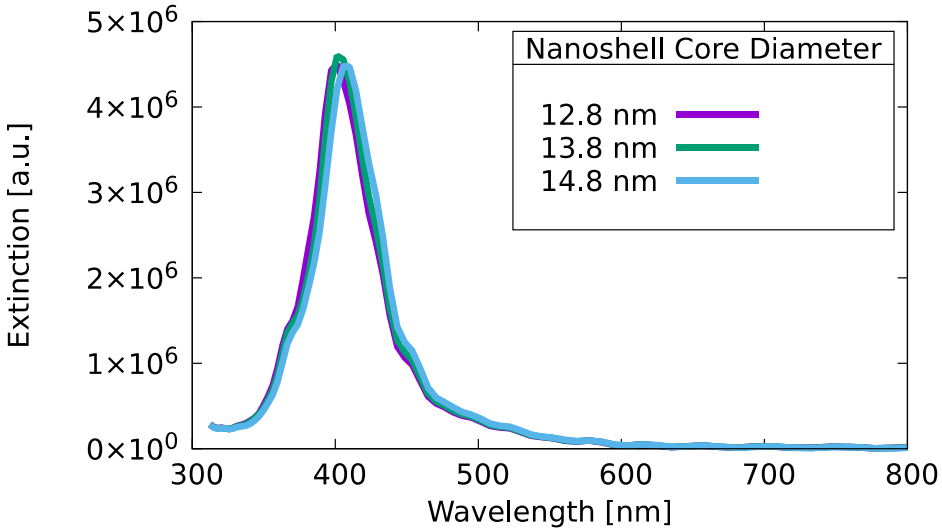

Figure A.11. Calculated extinction spectra of single silver nanoshells in water with vacuum core diameters of 12.8 nm, 13.8 nm, and 14.8 nm with total particle diameter of 38.0 nm.

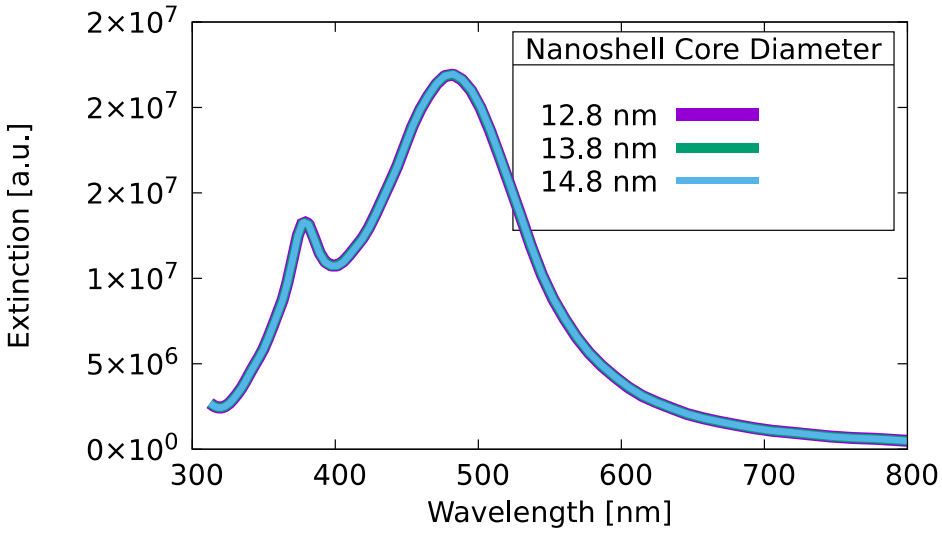

Figure A.12. Calculated extinction spectra of single silver nanoshells in water with vacuum core diameters of 12.8 nm, 13.8 nm, and 14.8 nm with total particle diameter of 87.8 nm.

Next, we present simulation results for gold-silver core-shell (Au-Ag CS) nanoparticles. To emulate the experimental polydispersity, we computed extinction for Au-Ag CS nanoparticles with core diameter of 13.8 nm and total diameters of 38, 41, 51, 60, 68, 72, 78, 84, and 88 nm. Here, the FDTD parameters were the same as those for the pure Ag shell case. The results are shown in Fig. 4 and discussed in the chapter 2. A key finding is that the extinction spectra in these CS nanoparticles are dominated by two shell-like modes. Additionally, the experimentally observed spectral widths cannot be explained by polydispersity alone and are likely due to a distribution of non-spherical shapes and surface roughness at the outer silver shell and buried gold-silver interface.

The calculated plasmonic extinction spectra, peak wavelengths, and relative extinction intensities for the gold-silver core-shell nanoparticles with varying shell thicknesses are shown in Figure A.13, for the case of a 13.8 nm gold spherical core, and silver shell thickness varying from 12 nm to 37 nm. The extinction spectra of gold-silver

core-shell nanoparticles have contributions from both the gold core and the silver shell; however, as the thickness of shell increases, the contribution from the silver shell increases and becomes more dominant. The “shell-like” nature of the spectrum is also apparent from the splittings between the two peaks in the spectrum. As the silver shell increases in thickness, the calculated extinction spectrum is observed to red shift, increase in intensity, and increase in spectral width. The dominant plasmon peak, which originates from the outer silver shell surface, varies from approximately 400 nm to 480 nm as the silver shell thickness increases. Additionally, a secondary plasmon peak is observed near 380 nm, corresponding to the inner silver shell, which remains relatively constant in wavelength and becomes more prominent as the silver shell thickness increases.

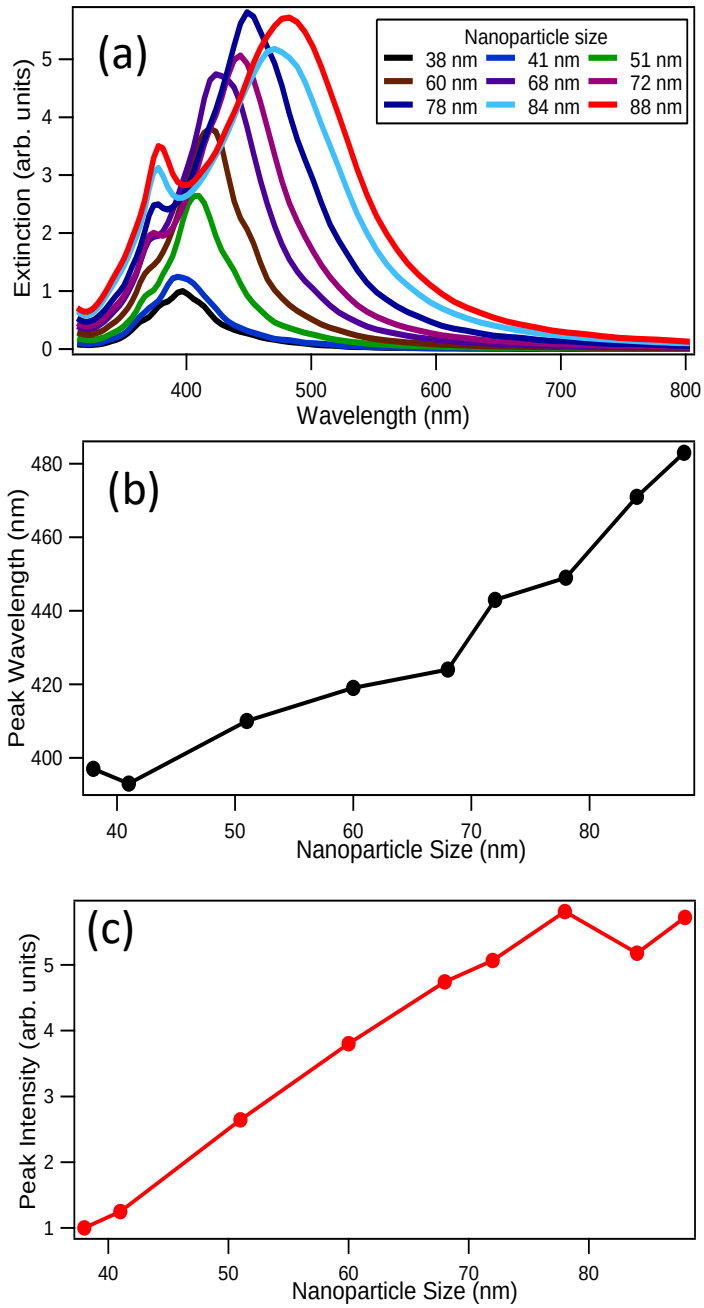

Figure A.13. (a) Calculated extinction spectra for the gold-silver core-shell nanoparticles with different silver shell thicknesses, with corresponding (b) peak wavelengths and (c) peak intensities as a function of the shell thickness from the FDTD results. Each Au@Ag nanoparticle has a 13.8 nm gold core.

A.4 Notes

1. Khoury, R. A.; Ranasinghe, J. C.; Dikkumbura, A. S.; Hamal, P.; Kumal, R. R.; Karam, T. E.; Smith, H. T.; Haber, L. H., Monitoring the Seed-Mediated Growth of Gold Nanoparticles Using in Situ Second Harmonic Generation and Extinction Spectroscopy. *J. Phys. Chem. C* **2018,** *122*, 24400-24406.

2. Smith, H. T.; Karam, T. E.; Haber, L. H.; Lopata, K., Capturing Plasmon–Molecule Dynamics in Dye Monolayers on Metal Nanoparticles Using Classical Electrodynamics with Quantum Embedding. *J. Phys. Chem. C* **2017,** *121*, 16932-16942.

3. Coomar, A.; Arntsen, C.; Lopata, K. A.; Pistinner, S.; Neuhauser, D., Near-field: A Finite-Difference Time-Dependent Method for Simulation of Electrodynamics on Small Scales. *J. Chem. Phys.* **2011,** *135*, 084121.

Appendix B. Efficient Photoinduced Energy Transfer in Porphyrin-Based Nanomaterials

B.1 Pump-Probe Transient Absorption Setup

Ultrafast transient absorption spectroscopy provides information about excited state dynamics including electron transfer, internal conversion, and intersystem crossing in a nanoparticle system under study. The experimental setup used for the characterization of porphyrin dyes and nanoGUMBOS is shown in Figure B.1 and explained in detail in Chapter 3.

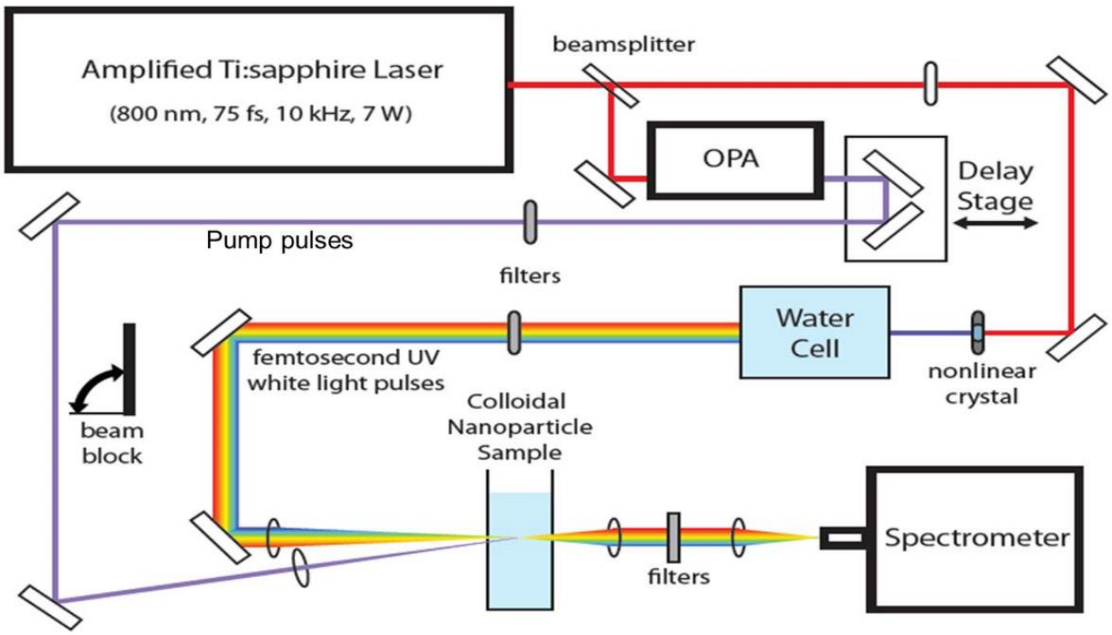

Figure B.1. Pump-probe transient absorption experimental setup.

List of References

1. Abécassis, B.; Testard, F.; Spalla, O.; Barboux, P., Probing In Situ the Nucleation and Growth of Gold Nanoparticles by Small-Angle X-ray Scattering. Nano Lett. 2007, 7, 1723-1727.

2. Abeyweera, S. C.; Rasamani, K. D.; Sun, Y., Ternary Silver Halide Nanocrystals. Acc. Chem. Res. 2017, 50, 1754-1761.

3. Abid, J.-P.; Nappa, J.; Girault, H. H.; Brevet, P.-F., Pure Surface Plasmon Resonance Enhancement of the First Hyperpolarizability of Gold Core–Silver Shell Nanoparticles. J. Chem. Phys. 2004, 121, 12577-12582.

4. Alvarez-Puebla, R.; Cui, B.; Bravo-Vasquez, J.-P.; Veres, T.; Fenniri, H., Nanoimprinted SERS-Active Substrates with Tunable Surface Plasmon Resonances. J. Phys. Chem. C 2007, 111, 6720-6723.

5. An, B.-K.; Kwon, S.-K.; Jung, S.-D.; Park, S. Y., Enhanced Emission and Its Switching in Fluorescent Organic Nanoparticles. J. Am. Chem. Soc. 2002, 124, 14410-14415.

6. Anandan, S.; Grieser, F.; Ashokkumar, M., Sonochemical Synthesis of Au− Ag Core−Shell Bimetallic Nanoparticles. J. Phys. Chem. C 2008, 112, 15102-15105.

7. Anisimov, S.; Kapeliovich, B.; Perelman, T., Electron Emission from Metal Surfaces Exposed to Ultrashort Laser Pulses. Zh. Eksp. Teor. Fiz 1974, 66, 375-377.

8. Bachelier, G.; Butet, J.; Russier-Antoine, I.; Jonin, C.; Benichou, E.; Brevet, P.-F., Origin of Optical Second-Harmonic Generation in Spherical Gold Nanoparticles: Local Surface and Nonlocal Bulk Contributions. Phys. Rev. B 2010, 82, 235403.

9. Baskin, J. S.; Yu, H.-Z.; Zewail, A. H., Ultrafast Dynamics of Porphyrins in the Condensed Phase: I. Free Base Tetraphenylporphyrin. J. Phys. Chem. A 2002, 106, 9837-9844.

10. Beane, G.; Devkota, T.; Brown, B. S.; Hartland, G. V., Ultrafast Measurements of the Dynamics of Single Nanostructures: A Review. Rep. Prog. Phys. 2018, 82, 016401.

11. Berera, R.; van Grondelle, R.; Kennis, J. T., Ultrafast Transient Absorption Spectroscopy: Principles and Application to Photosynthetic Systems. Photosynth. Res. 2009, 101, 105-118.

12. Bessho, T.; Zakeeruddin, S. M.; Yeh, C. Y.; Diau, E. W. G.; Grätzel, M., Highly Efficient Mesoscopic Dye-Sensitized Solar Cells Based on Donor–Acceptor-Substituted Porphyrins. Angew. Chem. 2010, 49, 6646-6649.

13. Besteiro, L. V.; Yu, P.; Wang, Z.; Holleitner, A. W.; Hartland, G. V.; Wiederrecht, G. P.; Govorov, A. O., The Fast and The Furious: Ultrafast Hot Electrons in Plasmonic Metastructures. Size and Structure Matter. Nano Today 2019.

14. Bisio, F.; Proietti Zaccaria, R.; Moroni, R.; Maidecchi, G.; Alabastri, A.; Gonella, G.; Giglia, A.; Andolfi, L.; Nannarone, S.; Mattera, L., Pushing the High-Energy Limit of Plasmonics. ACS Nano 2014, 8, 9239-9247.

15. Bonn, M.; Denzler, D. N.; Funk, S.; Wolf, M.; Wellershoff, S.-S.; Hohlfeld, J., Ultrafast Electron Dynamics at Metal Surfaces: Competition Between Electron-Phonon Coupling and Hot-Electron Transport. Phys. Rev. B 2000, 61, 1101.

16. Bonse, J.; Bachelier, G.; Siegel, J.; Solis, J., Time-and Space-Resolved Dynamics of Melting, Ablation, and Solidification Phenomena Induced by Femtosecond Laser Pulses in Germanium. Phys. Rev. B 2006, 74, 134106.

17. Bosco, C.; Azevedo, A.; Acioli, L., Substrate Dependent Ultrafast Dynamics in Thin NiFe Films. Appl. Phys. Lett. 2003, 83, 1767-1769.

18. Brown, K. R.; Walter, D. G.; Natan, M. J., Seeding of Colloidal Au Nanoparticle Solutions. 2. Improved Control of Particle Size and Shape. Chem. Mater. 2000, 12, 306-313.

19. Burda, C.; Chen, X.; Narayanan, R.; El-Sayed, M. A., Chemistry and Properties of Nanocrystals of Different Shapes. Chem. Rev. 2005, 105, 1025-1102.

20. Butet, J.; Brevet, P.-F.; Martin, O. J., Optical Second Harmonic Generation in Plasmonic Nanostructures: from Fundamental Principles to Advanced Applications. ACS Nano 2015, 9, 10545-10562.

21. Bwambok, D. K.; El-Zahab, B.; Challa, S. K.; Li, M.; Chandler, L.; Baker, G. A.; Warner, I. M., Near-Infrared Fluorescent nanoGUMBOS for Biomedical Imaging. ACS Nano 2009, 3, 3854-3860.

22. Castro-Lopez, M.; Brinks, D.; Sapienza, R.; van Hulst, N. F., Aluminum for Nonlinear Plasmonics: Resonance-Driven Polarized Luminescence of Al, Ag, and Au Nanoantennas. Nano Lett. 2011, 11, 4674-4678.

23. Charvet, R.; Yamamoto, Y.; Sasaki, T.; Kim, J.; Kato, K.; Takata, M.; Saeki, A.; Seki, S.; Aida, T., Segregated and Alternately Stacked Donor/Acceptor Nanodomains in Tubular Morphology Tailored with Zinc Porphyrin–C60 Amphiphilic Dyads: Clear Geometrical Effects on Photoconduction. J. Am. Chem. Soc. 2012, 134, 2524-2527.

24. Chen, J.; Tzou, D.; Beraun, J., A Semiclassical Two-Temperature Model for Ultrafast Laser Heating. Int. J. Heat Mass Transf. 2006, 49, 307-316.

25. Choi, M. S.; Yamazaki, T.; Yamazaki, I.; Aida, T., Bioinspired Molecular Design of Light-Harvesting Multiporphyrin Arrays. Angew. Chem. 2004, 43, 150-158.

26. Cole, M. R.; Li, M.; El-Zahab, B.; Janes, M. E.; Hayes, D.; Warner, I. M., Design, Synthesis, and Biological Evaluation of β-Lactam Antibiotic-Based Imidazolium-and Pyridinium-Type Ionic Liquids. Chem. Biol. Drug Des. 2011, 78, 33-41.

27. Cole, M. R.; Li, M.; Jadeja, R.; El-Zahab, B.; Hayes, D.; Hobden, J. A.; Janes, M. E.; Warner, I. M., Minimizing Human Infection From Escherichia Coli O157: H7 Using GUMBOS. J. Antimicrob. Chemother. 2013, 68, 1312-1318.

28. Coomar, A.; Arntsen, C.; Lopata, K. A.; Pistinner, S.; Neuhauser, D., Near-Field: A Finite-Difference Time-Dependent Method for Simulation of Electrodynamics on Small Scales. J. Chem. Phys. 2011, 135, 084121.

29. Cortie, M. B.; McDonagh, A. M., Synthesis and Optical Properties of Hybrid and Alloy Plasmonic Nanoparticles. Chem. Rev. 2011, 111, 3713-3735.

30. Dadap, J. I.; Shan, J.; Eisenthal, K. B.; Heinz, T. F., Second-Harmonic Rayleigh Scattering From a Sphere of Centrosymmetric Material. Phys. Rev. Lett. 1999, 83, 4045.

31. Darlington, A. M.; Gibbs-Davis, J. M., Bimodal or Trimodal? The Influence of Starting pH on Site Identity and Distribution at the Low Salt Aqueous/Silica Interface. J. Phys. Chem. C 2015, 119, 16560-16567.

32. Das, S.; Bwambok, D.; El-Zahab, B.; Monk, J.; de Rooy, S. L.; Challa, S.; Li, M.; Hung, F. R.; Baker, G. A.; Warner, I. M., Nontemplated Approach to Tuning the Spectral Properties of Cyanine-Based Fluorescent nanoGUMBOS. Langmuir 2010, 26, 12867-12876.

33. Das, S.; Magut, P. K.; de Rooy, S. L.; Hasan, F.; Warner, I. M., Ionic Liquid-Based Fluorescein Colorimetric pH Nanosensors. RSC Adv. 2013, 3, 21054-21061.

34. DeSantis, C. J.; Weiner, R. G.; Radmilovic, A.; Bower, M. M.; Skrabalak, S. E., Seeding Bimetallic Nanostructures As a New Class of Plasmonic Colloids. J. Phys. Chem. Lett. 2013, 4, 3072-3082.

35. Devkota, T.; Chakraborty, D.; Yu, K.; Beane, G.; Sader, J. E.; Hartland, G. V., On the Measurement of Relaxation Times of Acoustic Vibrations in Metal Nanowires. Phys. Chem. Chem. Phys. 2018, 20, 17687-17693.

36. Diring, S.; Puntoriero, F.; Nastasi, F.; Campagna, S.; Ziessel, R., Star-Shaped Multichromophoric Arrays From Bodipy Dyes Grafted on Truxene Core. J. Am. Chem. Soc. 2009, 131, 6108-6110.

37. Dominguez-Juarez, J. L.; Kozyreff, G.; Martorell, J., Whispering Gallery Microresonators for Second Harmonic Light Generation From a Low Number of Small Molecules. Nat. Commun. 2011, 2, 254.

38. Domke, M.; Nobile, L.; Rapp, S.; Eiselen, S.; Sotrop, J.; Huber, H. P.; Schmidt, M., Understanding Thin Film Laser Ablation: The Role of the Effective Penetration Depth and the Film Thickness. Phys. Procedia 2014, 56, 1007-1014.

39. Dörfer, T.; Schmitt, M.; Popp, J., Deep-UV Surface-Enhanced Raman Scattering. J. Raman Spectrosc. 2007, 38, 1379-1382.

40. Dorough, G.; Miller, J.; Huennekens, F. M., Spectra of the Metallo-Derivatives of α, β, γ, δ-Tetraphenylporphine. J. Am. Chem. Soc. 1951, 73, 4315-4320.

41. Doughty, B.; Ma, Y.-Z.; Shaw, R. W., Probing Interfacial Electronic States in CdSe Quantum Dots Using Second Harmonic Generation Spectroscopy. J. Phys. Chem. C 2015, 119, 2752-2760.

42. Doughty, B.; Rao, Y.; Kazer, S. W.; Kwok, S. J.; Turro, N. J.; Eisenthal, K. B., Binding of the Anti-Cancer Drug Daunomycin to DNA Probed by Second Harmonic Generation. J. Phys. Chem. B 2013, 117, 15285-15289.

43. Dreier, L. B.; Bernhard, C.; Gonella, G.; Backus, E. H.; Bonn, M., Surface Potential of a Planar Charged Lipid–Water Interface. What Do Vibrating Plate Methods, Second Harmonic and Sum Frequency Measure? J. Phys. Chem. Lett. 2018, 9, 5685-5691.

44. Du, B.; Fortin, D.; Harvey, P. D., Singlet and Triplet Energy Transfers in Tetra-(meso-truxene) zinc (II)-and Tetra-(meso-tritruxene) zinc (II) Porphyrin and Porphyrin-Free Base Dendrimers. Inorg. Chem. 2011, 50, 11493-11505.

45. Eisenthal, K. B., Second Harmonic Spectroscopy of Aqueous Nano-and Microparticle Interfaces. Chem. Rev. 2006, 106, 1462-1477.

46. El-Sayed, I. H.; Huang, X.; El-Sayed, M. A., Surface Plasmon Resonance Scattering and Absorption of Anti-EGFR Antibody Conjugated Gold Nanoparticles in Cancer Diagnostics: Applications in Oral Cancer. Nano Lett. 2005, 5, 829-834.

47. Elsayed-Ali, H.; Juhasz, T.; Smith, G.; Bron, W., Femtosecond Thermoreflectivity and Thermotransmissivity of Polycrystalline and Single-Crystalline Gold Films. Phys. Rev. B 1991, 43, 4488.

48. Ernstorfer, R.; Harb, M.; Hebeisen, C. T.; Sciaini, G.; Dartigalongue, T.; Miller, R. D., The Formation of Warm Dense Matter: Experimental Evidence for Electronic Bond Hardening in Gold. Science 2009, 323, 1033-1037.

49. Ethirajan, M.; Chen, Y.; Joshi, P.; Pandey, R. K., The Role of Porphyrin Chemistry in Tumor Imaging and Photodynamic Therapy. Chem. Soc. Rev. 2011, 40, 340-362.

50. Fang, R.; Zhang, D.; Wei, H.; Li, Z.; Yang, F.; Gao, Y., Improved Two-Temperature Model and Its Application in Femtosecond Laser Ablation of Metal Target. Laser Part. Beams 2010, 28, 157-164.

51. Fann, W.; Storz, R.; Tom, H.; Bokor, J., Electron Thermalization in Gold. Phys. Rev. B 1992, 46, 13592.

52. Farm, W.; Storz, R.; Tom, H.; Bokor, J., Direct Measurement of Nonequilibrium Electron-Energy Distributions in Sub-Picosecond Laser-Heated Gold Films. Surf. Sci. 1993, 283, 221-225.

53. Fearon, A. D.; Stokes, G. Y., Thermodynamics of Indomethacin Adsorption to Phospholipid Membranes. J. Phys. Chem. B 2017, 121, 10508-10518.

54. Fenwick, O.; Sprafke, J. K.; Binas, J.; Kondratuk, D. V.; Di Stasio, F.; Anderson, H. L.; Cacialli, F., Linear and Cyclic Porphyrin Hexamers As Near-Infrared Emitters in Organic Light-Emitting Diodes. Nano Lett. 2011, 11, 2451-2456.

55. Fita, P.; Fedoseeva, M.; Vauthey, E., Ultrafast Excited-State Dynamics of Eosin B: A Potential Probe of the Hydrogen-Bonding Properties of the Environment. J. Phys. Chem. A 2011, 115, 2465-2470.

56. Gadzuk, J., Resonance-Assisted Hot Electron Femtochemistry at Surfaces. Phys. Rev. Lett. 1996, 76, 4234.

57. Gan, W.; Gonella, G.; Zhang, M.; Dai, H.-L., Communication: Reactions and Adsorption at the Surface of Silver Nanoparticles Probed by Second Harmonic Generation. J. Chem. Phys. 2011, 134, 041104.

58. Ghosh Chaudhuri, R.; Paria, S., Core/Shell Nanoparticles: Classes, Properties, Synthesis Mechanisms, Characterization, and Applications. Chem. Rev. 2011, 112, 2373-2433.

59. Gilroy, K. D.; Ruditskiy, A.; Peng, H.-C.; Qin, D.; Xia, Y., Bimetallic Nanocrystals: Syntheses, Properties, and Applications. Chem. Rev. 2016, 116, 10414-10472.

60. Gonzalez, C. M.; Liu, Y.; Scaiano, J., Photochemical Strategies for the Facile Synthesis of Gold− Silver Alloy and Core−Shell Bimetallic Nanoparticles. J. Phys. Chem. C 2009, 113, 11861-11867.

61. Guo, C.; Rodriguez, G.; Lobad, A.; Taylor, A., Structural Phase Transition of Aluminum Induced by Electronic Excitation. Phys. Rev. Lett. 2000, 84, 4493.

62. Guo, C.; Taylor, A. J., Ultrafast Electronic Disorder in Heat-Induced Structural Deformations and Phase Transitions in Metals. Phys. Rev. B 2000, 62, 5382.

63. Guo, N.; Leu, M. C., Additive Manufacturing: Technology, Applications and Research Needs. Front. Mech. Eng. 2013, 8, 215-243.

64. Haber, L. H.; Kwok, S. J.; Semeraro, M.; Eisenthal, K. B., Probing the Colloidal Gold Nanoparticle/Aqueous Interface With Second Harmonic Generation. Chem. Phys. Lett. 2011, 507, 11-14.

65. Haes, A. J.; Van Duyne, R. P., A Nanoscale Optical Biosensor: Sensitivity and Selectivity of an Approach Based on the Localized Surface Plasmon Resonance Spectroscopy of Triangular Silver Nanoparticles. J. Am. Chem. Soc. 2002, 124 (35), 10596-10604.

66. Hamal, P.; Nguyenhuu, H.; Subasinghege Don, V.; Kumal, R. R.; Kumar, R.; McCarley, R. L.; Haber, L. H., Molecular Adsorption and Transport at Liposome Surfaces Studied by Molecular Dynamics Simulations and Second Harmonic Generation Spectroscopy. J. Phys. Chem. B 2019, 123, 7722-7730.

67. Hao, E.; Schatz, G. C.; Johnson, R.; Hupp, J. T., Hyper-Rayleigh Scattering From Silver Nanoparticles. J. Chem. Phys. 2002, 117, 5963-5966.

68. Hartland, G. V., Measurements of the Material Properties of Metal Nanoparticles by Time-Resolved Spectroscopy. Phys. Chem. Chem. Phys. 2004, 6, 5263-5274.

69. Hartland, G. V., Optical Studies of Dynamics in Noble Metal Nanostructures. Chem. Rev. 2011, 111, 3858-3887.

70. Hasobe, T., Porphyrin-Based Supramolecular Nanoarchitectures for Solar Energy Conversion. J. Phys. Chem. Lett. 2013, 4, 1771-1780.

71. Hayes, P. L.; Malin, J. N.; Jordan, D. S.; Geiger, F. M., Get charged up: Nonlinear Optical Voltammetry for Quantifying the Thermodynamics and Electrostatics of Metal Cations at Aqueous/Oxide Interfaces. Chem. Phys. Lett. 2010, 499, 183-192.

72. He, X.; Punpongjareorn, N.; Wu, C.; Davydov, I. A.; Yang, D.-S., Ultrafast Carrier Dynamics of CdTe: Surface Effects. J. Phys. Chem. C 2016, 120 (17), 9350-9356.

73. Herzog, D.; Seyda, V.; Wycisk, E.; Emmelmann, C., Additive Manufacturing of Metals. Acta Mater. 2016, 117, 371-392.

74. Hippius, C.; van Stokkum, I. H.; Gsaenger, M.; Groeneveld, M. M.; Williams, R. M.; Wuerthner, F., Sequential FRET Processes in Calix [4] Arene-Linked Orange-Red-Green Perylene Bisimide Dye Zigzag Arrays. J. Phys. Chem. C 2008, 112, 2476-2486.

75. Hod, I.; Sampson, M. D.; Deria, P.; Kubiak, C. P.; Farha, O. K.; Hupp, J. T., Fe-Porphyrin-Based Metal–Organic Framework Films as High-Surface Concentration, Heterogeneous Catalysts for Electrochemical Reduction of CO2. ACS Catal. 2015, 5, 6302-6309.

76. Hodak, J. H.; Martini, I.; Hartland, G. V., Spectroscopy and Dynamics of Nanometer-Sized Noble Metal Particles. J. Phys. Chem. B 1998, 102, 6958-6967.

77. Hohlfeld, J.; Müller, J.; Wellershoff, S.-S.; Matthias, E., Time-Resolved Thermoreflectivity of Thin Gold Films and Its Dependence on Film Thickness. Appl. Phys. B 1997, 64 (3), 387-390.

78. Hohlfeld, J.; Wellershoff, S.-S.; Güdde, J.; Conrad, U.; Jähnke, V.; Matthias, E., Electron and Lattice Dynamics Following Optical Excitation of Metals. Chem. Phys. 2000, 251, 237-258.

79. Hopkins, P. E.; Kassebaum, J. L.; Norris, P. M., Effects of Electron Scattering at Metal-Nonmetal Interfaces on Electron-Phonon Equilibration in Gold Films. J. Appl. Phys. 2009, 105, 023710.

80. Hopkins, P. E.; Norris, P. M., Substrate Influence in Electron–Phonon Coupling Measurements in Thin Au Films. Appl. Surf. Sci. 2007, 253, 6289-6294.

81. Hopkins, P. E.; Norris, P. M., Contribution of Ballistic Electron Transport to Energy Transfer During Electron-Phonon Nonequilibrium in Thin Metal Films. J. Heat Transfer 2009, 131, 043208.

82. Hostetler, J. L.; Smith, A. N.; Czajkowsky, D. M.; Norris, P. M., Measurement of the Electron-Phonon Coupling Factor Dependence on Film Thickness and Grain Size in Au, Cr, and Al. Appl. Opt. 1999, 38, 3614-3620.

83. Hou, Y.; Chen, S.-L.; Gan, W.; Ma, X.; Yuan, Q., Understanding the Dynamic Behavior of an Anti-cancer Drug-Doxorubicin on a Lipid Membrane Using Multiple Spectroscopic Techniques. J. Phys. Chem. B 2019.

84. Ho-Wu, R.; Sahu, P. K.; Wu, N.; Chen, T. K.; Yu, C.; Xie, J.; Goodson III, T., Understanding the Optical Properties of Au@ Ag Bimetallic Nanoclusters through Time-Resolved and Nonlinear Spectroscopy. J. Phys. Chem. C 2018, 122, 24368-24379.

85. Hsu, S.-W.; Rodarte, A. L.; Som, M.; Arya, G.; Tao, A. R., Colloidal Plasmonic Nanocomposites: From Fabrication to Optical Function. Chem. Rev. 2018, 118, 3100-3120.

86. Huang, X.; El-Sayed, I. H.; Qian, W.; El-Sayed, M. A., Cancer Cell Imaging and Photothermal Therapy in the Near-Infrared Region by Using Gold Nanorods. J. Am. Chem. Soc. 2006, 128, 2115-2120.

87. Ishida, Y.; Masui, D.; Shimada, T.; Tachibana, H.; Inoue, H.; Takagi, S., The Mechanism of the Porphyrin Spectral Shift on Inorganic Nanosheets: The Molecular Flattening Induced by the Strong Host–Guest Interaction Due to the “Size-Matching Rule”. J. Phys. Chem. C 2012, 116, 7879-7885.

88. Jana, N. R.; Gearheart, L.; Murphy, C. J., Evidence for Seed-Mediated Nucleation in the Chemical Reduction of Gold Salts to Gold Nanoparticles. Chem. Mater. 2001, 13, 2313-2322.

89. Jen, S.-H.; Gonella, G.; Dai, H.-L., The Effect of Particle Size in Second Harmonic Generation From the Surface of Spherical Colloidal Particles. I: Experimental Observations. J. Phys. Chem. A 2009, 113, 4758-4762.

90. Jha, S. K.; Ahmed, Z.; Agio, M.; Ekinci, Y.; Löffler, J. r. F., Deep-UV Surface-Enhanced Resonance Raman Scattering of Adenine on Aluminum Nanoparticle Arrays. J. Am. Chem. Soc. 2012, 134, 1966-1969.

91. Jiang, L.; Tsai, H.-L., Improved Two-Temperature Model and Its Application in Ultrashort Laser Heating of Metal Films. J. Heat Transfer 2005, 127, 1167-1173.

92. Jiang, L.; Tsai, H.-L., A Plasma Model Combined With an Improved Two-Temperature Equation for Ultrafast Laser Ablation of Dielectrics. J. Appl. Phys. 2008, 104, 093101.

93. Jin, R.; Jureller, J. E.; Kim, H. Y.; Scherer, N. F., Correlating Second Harmonic Optical Responses of Single Ag Nanoparticles With Morphology. J. Am. Chem. Soc. 2005, 127, 12482-12483.

94. Jones, M. R.; Osberg, K. D.; Macfarlane, R. J.; Langille, M. R.; Mirkin, C. A., Templated Techniques for the Synthesis and Assembly of Plasmonic Nanostructures. Chem. Rev. 2011, 111, 3736-3827.

95. Jordan, A. N.; Das, S.; Siraj, N.; de Rooy, S. L.; Li, M.; El-Zahab, B.; Chandler, L.; Baker, G. A.; Warner, I. M., Anion-Controlled Morphologies and Spectral Features of Cyanine-Based nanoGUMBOS–An Improved Photosensitizer. Nanoscale 2012, 4, 5031-5038.

96. Kamat, P. V., Meeting the Clean Energy Demand: Nanostructure Architectures for Solar Energy Conversion. J. Phys. Chem. C 2007, 111, 2834-2860.

97. Kandyla, M.; Shih, T.; Mazur, E., Femtosecond Dynamics of the Laser-Induced Solid-to-Liquid Phase Transition in Aluminum. Phys. Rev. B 2007, 75, 214107.

98. Karam, T. E.; Haber, L. H., Molecular Adsorption and Resonance Coupling at the Colloidal Gold Nanoparticle Interface. J. Phys. Chem. C 2013, 118, 642-649.

99. Karam, T. E.; Khoury, R. A.; Haber, L. H., Excited-State Dynamics of Size-Dependent Colloidal TiO2-Au Nanocomposites. J. Chem. Phys. 2016, 144, 124704.

100. Karam, T. E.; Siraj, N.; Warner, I. M.; Haber, L. H., Anomalous Size-Dependent Excited-State Relaxation Dynamics of NanoGUMBOS. J. Phys. Chem. C 2015, 119, 28206-28213.

101. Karam, T. E.; Siraj, N.; Zhang, Z.; Ezzir, A. F.; Warner, I. M.; Haber, L. H., Ultrafast and Nonlinear Spectroscopy of Brilliant Green-Based nanoGUMBOS With Enhanced Near-Infrared Emission. J. Chem. Phys. 2017, 147, 144701.

102. Karam, T. E.; Smith, H. T.; Haber, L. H., Enhanced Photothermal Effects and Excited-State Dynamics of Plasmonic Size-Controlled Gold–Silver–Gold Core–Shell–Shell Nanoparticles. J. Phys. Chem. C 2015, 119, 18573-18580.

103. Kessel, D.; Luguya, R.; Vicente, M. G. H., Localization and Photodynamic Efficacy of Two Cationic Porphyrins Varying in Charge Distribution¶. Photochem. Photobiol. 2003, 78, 431-435.

104. Khoury, R. A.; Ranasinghe, J. C.; Dikkumbura, A. S.; Hamal, P.; Kumal, R. R.; Karam, T. E.; Smith, H. T.; Haber, L. H., Monitoring the Seed-Mediated Growth of Gold Nanoparticles Using in Situ Second Harmonic Generation and Extinction Spectroscopy. J. Phys. Chem. C 2018, 122, 24400-24406.

105. Knowles, K. E.; Koch, M. D.; Shelton, J. L., Three Applications of Ultrafast Transient Absorption Spectroscopy of Semiconductor Thin Films: Spectroelectrochemistry, Microscopy, and Identification of Thermal Contributions. J. Mater. Chem. C 2018, 6, 11853-11867.

106. Kolic, P. E.; Siraj, N.; Hamdan, S.; Regmi, B. P.; Warner, I. M., Synthesis and Characterization of Porphyrin-Based GUMBOS and NanoGUMBOS as Improved Photosensitizers. J. Phys. Chem. C 2016, 120, 5155-5163.

107. Kumal, R. R.; Abu-Laban, M.; Hamal, P.; Kruger, B.; Smith, H. T.; Hayes, D. J.; Haber, L. H., Near-Infrared Photothermal Release of siRNA from the Surface of Colloidal Gold–Silver–Gold Core–Shell–Shell Nanoparticles Studied with Second-Harmonic Generation. J. Phys. Chem. C 2018, 122, 19699-19704.

108. Kumal, R. R.; Karam, T. E.; Haber, L. H., Determination of the Surface Charge Density of Colloidal Gold Nanoparticles Using Second Harmonic Generation. J. Phys. Chem. C 2015, 119, 16200-16207.

109. Kumal, R. R.; Landry, C. R.; Abu-Laban, M.; Hayes, D. J.; Haber, L. H., Monitoring the Photocleaving Dynamics of Colloidal Microrna-Functionalized Gold Nanoparticles Using Second Harmonic Generation. Langmuir 2015, 31, 9983-9990.

110. Kumal, R. R.; Nguyenhuu, H.; Winter, J. E.; McCarley, R. L.; Haber, L. H., Impacts of Salt, Buffer, and Lipid Nature on Molecular Adsorption and Transport in Liposomes as Observed by Second Harmonic Generation. J. Phys. Chem. C 2017, 121, 15851-15860.

111. Leguay, P.; Lévy, A.; Chimier, B.; Deneuville, F.; Descamps, D.; Fourment, C.; Goyon, C.; Hulin, S.; Petit, S.; Peyrusse, O., Ultrafast Short-Range Disordering of Femtosecond-Laser-Heated Warm Dense Aluminum. Phys. Rev. Lett. 2013, 111, 245004.

112. Li, J.-F.; Zhang, Y.-J.; Ding, S.-Y.; Panneerselvam, R.; Tian, Z.-Q., Core–Shell Nanoparticle-Enhanced Raman Spectroscopy. Chem. Rev. 2017, 117, 5002-5069.

113. Li, L.-L.; Diau, E. W.-G., Porphyrin-Sensitized Solar Cells. Chem. Soc. Rev. 2013, 42, 291-304.

114. Liao, P.; Wokaun, A., Lightning Rod Effect in Surface Enhanced Raman Scattering. J. Chem. Phys. 1982, 76, 751-752.

115. Lin, S.; Diercks, C. S.; Zhang, Y.-B.; Kornienko, N.; Nichols, E. M.; Zhao, Y.; Paris, A. R.; Kim, D.; Yang, P.; Yaghi, O. M., Covalent Organic Frameworks Comprising Cobalt Porphyrins for Catalytic CO2 Reduction in Water. Science 2015, 349, 1208-1213.

116. Lindley, S. A.; Zhang, J. Z., Bumpy Hollow Gold Nanospheres for Theranostic Applications: Effect of Surface Morphology on Photothermal Conversion Efficiency. ACS Appl. Nano Mater. 2019, 2, 1072-1081.

117. Link, S.; El-Sayed, M., Spectral Properties and Relaxation Dynamics of Surface Plasmon Electronic Oscillations in Gold and Silver Nanodots and Nanorods. J. Phys. Chem. B 1999, 103, 8410-8426.

118. Link, S.; El-Sayed, M. A., Shape and Size Dependence of Radiative, Non-Radiative and Photothermal Properties of Gold Nanocrystals. Intl. Rev. Phys. Chem. 2000, 19, 409-453.

119. Liu, J.; Subir, M.; Nguyen, K.; Eisenthal, K. B., Second Harmonic Studies of Ions Crossing Liposome Membranes in Real Time. J. Phys. Chem. B 2008, 112, 15263-15266.

120. Liu, Y.; Dadap, J.; Zimdars, D.; Eisenthal, K. B., Study of Interfacial Charge-Transfer Complex on TiO2 Particles in Aqueous Suspension by Second-Harmonic Generation. J. Phys. Chem. B 1999, 103, 2480-2486.

121. Lopata, K.; Neuhauser, D., Multiscale Maxwell–Schrödinger Modeling: A Split Field Finite-Difference Time-Domain Approach to Molecular Nanopolaritonics. J. Chem. Phys. 2009, 130, 104707.

122. Lu, C.; Das, S.; Magut, P. K.; Li, M.; El-Zahab, B.; Warner, I. M., Irradiation InducedFfluorescence Enhancement in PEGylated Cyanine-Based NIR Nano-and Mesoscale GUMBOS. Langmuir 2012, 28, 14415-14423.

123. Lu, H.-P.; Tsai, C.-Y.; Yen, W.-N.; Hsieh, C.-P.; Lee, C.-W.; Yeh, C.-Y.; Diau, E. W.-G., Control of Dye Aggregation and Electron Injection for Highly Efficient Porphyrin Sensitizers Adsorbed on Semiconductor Films with Varying Ratios of Coadsorbate. J. Phys. Chem. C 2009, 113, 20990-20997.

124. Lu, L.; Burkey, G.; Halaciuga, I.; Goia, D. V., Core–Shell Gold/Silver Nanoparticles: Synthesis and Optical Properties. J. Colloid Interface Sci. 2013, 392, 90-95.

125. Lu, L.; Wang, H.; Zhou, Y.; Xi, S.; Zhang, H.; Hu, J.; Zhao, B., Seed-Mediated Growth of Large, Monodisperse Core–Shell Gold–Silver Nanoparticles With Ag-Like Optical Properties. ChemComm 2002, 144-145.

126. Maeda, C.; Taniguchi, T.; Ogawa, K.; Ema, T., Bifunctional Catalysts Based on m-Phenylene-Bridged Porphyrin Dimer and Trimer Platforms: Synthesis of Cyclic Carbonates from Carbon Dioxide and Epoxides. Angew. Chem. 2015, 54, 134-138.

127. Magut, P. K.; Das, S.; Fernand, V. E.; Losso, J.; McDonough, K.; Naylor, B. M.; Aggarwal, S.; Warner, I. M., Tunable Cytotoxicity of Rhodamine 6G via Anion Variations. J. Am. Chem. Soc. 2013, 135, 15873-15879.

128. Majumdar, A.; Fushinobu, K.; Hijikata, K., Effect of Gate Voltage on Hot-Electron and Hot Phonon Interaction and Transport in a Submicrometer Transistor. J. Appl. Phys. 1995, 77, 6686-6694.

129. McGilvray, K. L.; Fasciani, C.; Bueno-Alejo, C. J.; Schwartz-Narbonne, R.; Scaiano, J. C., Photochemical Strategies for the Seed-Mediated Growth of Gold and Gold–Silver Nanoparticles. Langmuir 2012, 28, 16148-16155.

130. McPeak, K. M.; Jayanti, S. V.; Kress, S. J.; Meyer, S.; Iotti, S.; Rossinelli, A.; Norris, D. J., Plasmonic Films Can Easily Be Better: Rules and Recipes. ACS Photonics 2015, 2, 326-333.

131. McPeak, K. M.; Le, T. P.; Britton, N. G.; Nickolov, Z. S.; Elabd, Y. A.; Baxter, J. B., Chemical Bath Deposition of ZnO Nanowires at Near-Neutral pH Conditions Without Hexamethylenetetramine (HMTA): Understanding the role of HMTA in ZnO Nanowire Growth. Langmuir 2011, 27, 3672-3677.

132. Meyer, S. A.; Le Ru, E. C.; Etchegoin, P. G., Combining Surface Plasmon Resonance (SPR) Spectroscopy With Surface-Enhanced Raman Scattering (SERS). Anal. Chem. 2011, 83, 2337-2344.

133. Mickley Conron, S. M.; Shoer, L. E.; Smeigh, A. L.; Ricks, A. B.; Wasielewski, M. R., Photoinitiated Electron Transfer in Zinc Porphyrin–Perylenediimide Cruciforms and Their Self-Assembled Oligomers. J. Phys. Chem. B 2013, 117, 2195-2204.

134. Mourdikoudis, S.; Pallares, R. M.; Thanh, N. T., Characterization Techniques for Nanoparticles: Comparison and Complementarity Upon Studying Nanoparticle Properties. Nanoscale 2018, 10, 12871-12934.

135. Mozer, A. J.; Griffith, M. J.; Tsekouras, G.; Wagner, P.; Wallace, G. G.; Mori, S.; Sunahara, K.; Miyashita, M.; Earles, J. C.; Gordon, K. C., Zn− Zn Porphyrin Dimer-Sensitized Solar Cells: Toward 3-D Light Harvesting. J. Am. Chem. Soc. 2009, 131, 15621-15623.

136. Negre, C. F.; Milot, R. L.; Martini, L. A.; Ding, W.; Crabtree, R. H.; Schmuttenmaer, C. A.; Batista, V. S., Efficiency of Interfacial Electron Transfer From Zn-Porphyrin Dyes Into TiO2 Correlated to the Linker Single Molecule Conductance. J. Phys. Chem. C 2013, 117, 24462-24470.

137. Ngo, T. D.; Kashani, A.; Imbalzano, G.; Nguyen, K. T.; Hui, D., Additive Manufacturing (3D printing): A Review of Materials, Methods, Applications and Challenges. Composites Part B 2018, 143, 172-196.

138. Nguyen, T. T.; Sly, K. L.; Conboy, J. C., Comparison of the Energetics of Avidin, Streptavidin, NeutrAvidin, and Anti-Biotin Antibody Binding to Biotinylated Lipid Bilayer Examined by Second-Harmonic Generation. Anal. Chem. 2011, 84, 201-208.

139. Nie, S.; Emory, S. R., Probing Single Molecules and Single Nanoparticles by Surface-Enhanced Raman Scattering. Science 1997, 275, 1102-1106.

140. Nikoobakht, B.; Wang, J.; El-Sayed, M. A., Surface-Enhanced Raman Scattering of Molecules Adsorbed on Gold Nanorods: Off-Surface Plasmon Resonance Condition. Chem. Phys. Lett. 2002, 366, 17-23.

141. Norris, C. B.; Joseph, P. R.; Mackiewicz, M. R.; Reed, S. M., Minimizing Formaldehyde Use in the Synthesis of Gold− Silver Core− Shell Nanoparticles. Chem. Mater. 2010, 22, 3637-3645.

142. Norris, P. M.; Caffrey, A. P.; Stevens, R. J.; Klopf, J. M.; McLeskey Jr, J. T.; Smith, A. N., Femtosecond Pump–Probe Nondestructive Examination of Materials. Rev. Sci. Instrum. 2003, 74, 400-406.

143. O'Connor, A. E.; Gallagher, W. M.; Byrne, A. T., Porphyrin and Nonporphyrin Photosensitizers in Oncology: Preclinical and Clinical Advances in Photodynamic Therapy. Photochem. Photobiol. 2009, 85, 1053-1074.

144. Oh, H.; Lee, J.; Seo, M.; Baek, I. U.; Byun, J. Y.; Lee, M., Laser-Induced Dewetting of Metal Thin Films for Template-Free Plasmonic Color Printing. ACS Appl. Mater. Interfaces 2018, 10, 38368-38375.

145. Ohkita, H.; Cook, S.; Astuti, Y.; Duffy, W.; Tierney, S.; Zhang, W.; Heeney, M.; McCulloch, I.; Nelson, J.; Bradley, D. D., Charge Carrier Formation in Polythiophene/Fullerene Blend Films Studied by Transient Absorption Spectroscopy. J. Am. Chem. Soc. 2008, 130, 3030-3042.

146. Omagari, T.; Suzuki, A.; Akita, M.; Yoshizawa, M., Efficient Catalytic Epoxidation in Water by Axial N-Ligand-Free Mn-Porphyrins Within a Micellar Capsule. J. Am. Chem. Soc. 2016, 138, 499-502.

147. Örtegren, J.; Wantke, K.-D.; Motschmann, H.; Möhwald, H., A Study of Kinetic Molecular Exchange Processes in the Medium Frequency Range by Surface SHG on an Oscillating Bubble. J. Colloid Interface Sci. 2004, 279, 266-276.

148. Pandey, R. K.; BELLNIER, D. A.; SMITH, K. M.; DOUGHERTY, T. J., Chlorin and Porphyrin Derivatives as Potential Photosensitizers in Photodynamic Therapy. Photochem. Photobiol. 1991, 53, 65-72.

149. Patra, S.; Sen, D.; Pandey, A. K.; Bahadur, J.; Mazumder, S.; Ramagiri, S. V.; Bellare, J. R.; Roth, S. V.; Santoro, G.; Yu, S., Time Resolved Growth of Membrane Stabilized Silver NPs and Their Catalytic Activity. RSC Adv. 2014, 4, 59379-59386.

150. Pekkarinen, L.; Linschitz, H., Studies on Metastable States of Porphyrins. II. Spectra and Decay Kinetics of Tetraphenylporphine, Zinc Tetraphenylporphine and Bacteriochlorophyll1. J. Am. Chem. Soc. 1960, 82, 2407-2411.

151. Perrault, S. D.; Chan, W. C., Synthesis and Surface Modification of Highly Monodispersed, Spherical Gold Nanoparticles of 50− 200 nm. J. Am. Chem. Soc. 2009, 131, 17042-17043.

152. Petkau, K.; Kaeser, A.; Fischer, I.; Brunsveld, L.; Schenning, A. P., Pre-and Postfunctionalized Self-Assembled π-Conjugated Fluorescent Organic Nanoparticles for Dual Targeting. J. Am. Chem. Soc. 2011, 133, 17063-17071.

153. Plummer, E.; Shi, J.; Tang, S.-J.; Rotenberg, E.; Kevan, S., Enhanced Electron–Phonon Coupling at Metal Surfaces. Prog. Surf. Sci 2003, 74, 251-268.

154. Polte, J.; Herder, M.; Erler, R.; Rolf, S.; Fischer, A.; Würth, C.; Thünemann, A. F.; Kraehnert, R.; Emmerling, F., Mechanistic Insights Into Seeded Growth Processes of Gold Nanoparticles. Nanoscale 2010, 2, 2463-2469.

155. Polte, J. r.; Ahner, T. T.; Delissen, F.; Sokolov, S.; Emmerling, F.; Thünemann, A. F.; Kraehnert, R., Mechanism of Gold Nanoparticle Formation in the Classical Citrate

Synthesis Method Derived From Coupled In Situ XANES and SAXS Evaluation. J. Am. Chem. Soc. 2010, 132, 1296-1301.

156. Polte, J. r.; Tuaev, X.; Wuithschick, M.; Fischer, A.; Thuenemann, A. F.; Rademann, K.; Kraehnert, R.; Emmerling, F., Formation Mechanism of Colloidal Silver Nanoparticles: Analogies and Differences to the Growth of Gold Nanoparticles. ACS Nano 2012, 6, 5791-5802.

157. Prigodich, A. E.; Lee, O.-S.; Daniel, W. L.; Seferos, D. S.; Schatz, G. C.; Mirkin, C. A., Tailoring DNA Structure to Increase Target Hybridization Kinetics on Surfaces. J. Am. Chem. Soc. 2010, 132, 10638-10641.

158. Qin, Y.; Ji, X.; Jing, J.; Liu, H.; Wu, H.; Yang, W., Size Control Over Spherical Silver Nanoparticles by Ascorbic Acid Reduction. Colloids Surf., A 2010, 372, 172-176.

159. Qiu, T.; Tien, C., Femtosecond Laser Heating of Multi-Layer Metals—I. Analysis. Int. J. Heat Mass Transf. 1994, 37, 2789-2797.

160. Rapp, S.; Kaiser, M.; Schmidt, M.; Huber, H. P., Ultrafast Pump-Probe Ellipsometry Setup for the Measurement of Transient Optical Properties During Laser Ablation. Opt. Express 2016, 24, 17572-17592.

161. Ray, K.; Chowdhury, M. H.; Lakowicz, J. R., Aluminum Nanostructured Films as Substrates for Enhanced Fluorescence in the Ultraviolet-Bue Spectral Region. Anal. Chem. 2007, 79, 6480-6487.

162. Ray, P. C., Size and Shape Dependent Second Order Nonlinear Optical Properties of Nanomaterials and Their Application in Biological and Chemical Sensing. Chem. Rev. 2010, 110, 5332-5365.

163. Regmi, B. P.; Monk, J.; El-Zahab, B.; Das, S.; Hung, F. R.; Hayes, D. J.; Warner, I. M., A Novel Composite Film for Detection and Molecular Weight Determination of Organic Vapors. J. Mater. Chem. 2012, 22, 13732-13741.

164. Roke, S.; Gonella, G., Nonlinear Light Scattering and Spectroscopy of Particles and Droplets in Liquids. Annu. Rev. Phys. Chem. 2012, 63, 353-378.

165. Russier-Antoine, I.; Benichou, E.; Bachelier, G.; Jonin, C.; Brevet, P., Multipolar Contributions of the Second Harmonic Generation From Silver and Gold Nanoparticles. J. Phys. Chem. C 2007, 111, 9044-9048.

166. Sabbah, A.; Riffe, D. M., Femtosecond Pump-Probe Reflectivity Study of Silicon Carrier Dynamics. Phys. Rev. B 2002, 66, 165217.

167. Samal, A. K.; Polavarapu, L.; Rodal-Cedeira, S.; Liz-Marzán, L. M.; Pérez-Juste, J.; Pastoriza-Santos, I., Size Tunable Au@Ag Core–Shell Nanoparticles: Synthesis and Surface-Enhanced Raman Scattering Properties. Langmuir 2013, 29, 15076-15082.

168. Sauerbeck, C.; Haderlein, M.; Schürer, B.; Braunschweig, B. r.; Peukert, W.; Klupp Taylor, R. N., Shedding Light on the Growth of Gold Nanoshells. ACS Nano 2014, 8, 3088-3096.

169. Shen, Y., Surface Properties Probed by Second-Harmonic and Sum-Frequency Generation. Nature 1989, 337, 519.

170. Shirakawa, M.; Fujita, N.; Shinkai, S., A Stable Single Piece of Unimolecularly π-Stacked Porphyrin Aggregate in a Thixotropic Low Molecular Weight Gel: A One-Dimensional Molecular Template for Polydiacetylene Wiring Up To Several Tens of Micrometers In Length. J. Am. Chem. Soc. 2005, 127, 4164-4165.

171. Siraj, N.; Hasan, F.; Das, S.; Kiruri, L. W.; Steege Gall, K. E.; Baker, G. A.; Warner, I. M., Carbazole-Derived Group of Uniform Materials Based on Organic Salts: Solid State Fluorescent Analogues of Ionic Liquids for Potential Applications in Organic-Based Blue Light-Emitting Diodes. J. Phys. Chem. C 2014, 118, 2312-2320.

172. Smith, A. N.; Norris, P. M., Influence of Intraband Transitions on the Electron Thermoreflectance Response of Metals. Appl. Phys. Lett. 2001, 78, 1240-1242.

173. Smith, H. T.; Karam, T. E.; Haber, L. H.; Lopata, K., Capturing Plasmon–Molecule Dynamics in Dye Monolayers on Metal Nanoparticles Using Classical Electrodynamics With Quantum Embedding. J. Phys. Chem. C 2017, 121, 16932-16942.

174. Song, Z.; Sarkar, S.; Vogt, A. D.; Danzer, G. D.; Smith, C. J.; Gualtieri, E. J.; Simpson, G. J., Kinetic Modeling of Accelerated Stability Testing Enabled by Second Harmonic Generation Microscopy. Anal. Chem. 2018, 90, 4406-4413.

175. Sperling, R. A.; Gil, P. R.; Zhang, F.; Zanella, M.; Parak, W. J., Biological Applications of Gold Nanoparticles. Chem. Soc. Rev. 2008, 37, 1896-1908.
176. Stedman, R.; Almqvist, L.; Nilsson, G., Phonon-Frequency Distributions and Heat Capacities of Aluminum and Lead. Phys. Rev. 1967, 162, 549.

177. Steiger, B.; Baskin, J. S.; Anson, F. C.; Zewail, A. H., Femtosecond Dynamics of Dioxygen–Picket-Fence Cobalt Porphyrins: Ultrafast Release of O2 and the Nature of Dative Bonding. Angew. Chem. 2000, 39, 257-260.

178. Sun, C.-K.; Vallee, F.; Acioli, L.; Ippen, E.; Fujimoto, J., Femtosecond Investigation of Electron Thermalization in Gold. Phys. Rev. B 1993, 48, 12365.

179. Sun, C.-K.; Vallée, F.; Acioli, L.; Ippen, E.; Fujimoto, J., Femtosecond-Tunable Measurement of Electron Thermalization in Gold. Phys. Rev. B 1994, 50, 15337.

180. Tan, S. F.; Chee, S. W.; Lin, G.; Bosman, M.; Lin, M.; Mirsaidov, U.; Nijhuis, C. A., Real-Time Imaging of the Formation of Au–Ag Core–Shell Nanoparticles. J. Am. Chem. Soc. 2016, 138, 5190-5193.

181. Thomas, D. W.; Martell, A. E., Absorption Spectra of Para-Substituted Tetraphenylporphines1, 2. J. Am. Chem. Soc. 1956, 78, 1338-1343.

182. Thyagarajan, K.; Rivier, S.; Lovera, A.; Martin, O. J., Enhanced Second-Harmonic Generation From Double Resonant Plasmonic Antennae. Opt. Express 2012, 20, 12860-12865.

183. Tsuji, M.; Miyamae, N.; Lim, S.; Kimura, K.; Zhang, X.; Hikino, S.; Nishio, M., Crystal Structures and Growth Mechanisms of Au@ Ag Core−Shell Nanoparticles Prepared by the Microwave−Polyol Method. Crystal growth & design 2006, 6, 1801-1807.

184. Turkpence, D.; Akguc, G. B.; Bek, A.; Tasgin, M. E., Engineering Nonlinear Response of Nanomaterials Using Fano Resonances. J. Opt. 2014, 16, 105009.

185. Uetomo, A.; Kozaki, M.; Suzuki, S.; Yamanaka, K.-i.; Ito, O.; Okada, K., Efficient Light-Harvesting Antenna With a Multi-Porphyrin Cascade. J. Am. Chem. Soc. 2011, 133, 13276-13279.

186. Vance, F. W.; Lemon, B. I.; Hupp, J. T., Enormous Hyper-Rayleigh Scattering From Nanocrystalline Gold Particle Suspensions. J. Phys. Chem. B 1998, 102, 10091-10093.

187. Vickers, E. T.; Garai, M.; Bonabi Naghadeh, S.; Lindley, S.; Hibbs, J.; Xu, Q.-H.; Zhang, J. Z., Two-Photon Photoluminescence and Photothermal Properties of Hollow Gold Nanospheres for Efficient Theranostic Applications. J. Phys. Chem. C 2017, 122, 13304-13313.

188. Wang, B.; Gallais, L., A Theoretical Investigation of the Laser Damage Threshold of Metal Multi-Dielectric Mirrors for High Power Ultrashort Applications. Opt. Express 2013, 21, 14698-14711.

189. Wang, Q.; Morrow, J. D.; Ma, C.; Duffie, N. A.; Pfefferkorn, F. E., Surface Prediction Model for Thermocapillary Regime Pulsed Laser Micro Polishing of Metals. J. Manuf. Processes 2015, 20, 340-348.

190. Wang, Y.; Camargo, P. H.; Skrabalak, S. E.; Gu, H.; Xia, Y., A Facile, Water-Based Synthesis of Highly Branched Nanostructures of Silver. Langmuir 2008, 24, 12042-12046.

191. Warner, I. M.; El-Zahab, B.; Siraj, N., Perspectives On Moving Ionic Liquid Chemistry Into the Solid Phase. Anal. Chem. 2014, 86, 7184-7191.

192. Wasielewski, M. R., Self-Assembly Strategies for Integrating Light Harvesting and Charge Separation in Artificial Photosynthetic Systems. Acc. Chem. Res. 2009, 42, 1910-1921.

193. Weiner, R. G.; Kunz, M. R.; Skrabalak, S. E., Seeding a New Kind of Garden: Synthesis of Architecturally Defined Multimetallic Nanostructures by Seed-Mediated Co-Reduction. Acc. Chem. Res. 2015, 48, 2688-2695.

194. Wellershoff, S.-S.; Hohlfeld, J.; Güdde, J.; Matthias, E., The Role of Electron–Phonon Coupling in Femtosecond Laser Damage of Metals. Appl. Phys. A 1999, 69, S99-S107.

195. Whiteside, P. J.; Chininis, J. A.; Hunt, H. K., Techniques and Challenges for Characterizing Metal Thin Films With Applications in Photonics. Coatings 2016, 6, 35.

196. Woehl, T. J.; Evans, J. E.; Arslan, I.; Ristenpart, W. D.; Browning, N. D., Direct In Situ Determination of the Mechanisms Controlling Nanoparticle Nucleation and rowth. ACS Nano 2012, 6, 8599-8610.

197. Xu, X.; Yang, F.; Li, X.; Gao, Y., Non-Equilibrium Heat Transport of Copper-Silver Alloy Films by Femtosecond Laser With Double Pump Beams. Optik 2019, 176, 114-118.

198. Yadroitsev, I.; Bertrand, P.; Smurov, I., Parametric Analysis of the Selective Laser Melting Process. Appl. Surf. Sci. 2007, 253, 8064-8069.

199. Yan, E. C.; Liu, Y.; Eisenthal, K. B., New Method for Determination of Surface Potential of Microscopic Particles by Second Harmonic Generation. J. Phys. Chem. B 1998, 102, 6331-6336.

200. Yang, J.; Choi, J.; Bang, D.; Kim, E.; Lim, E. K.; Park, H.; Suh, J. S.; Lee, K.; Yoo, K. H.; Kim, E. K., Convertible Organic Nanoparticles for Near-Infrared Photothermal Ablation of Cancer Cells. Angew. Chem. 2011, 50, 441-444.

201. Yang, K.; Xu, H.; Cheng, L.; Sun, C.; Wang, J.; Liu, Z., In Vitro and In Vivo Near-Infrared Photothermal Therapy of Cancer Using Polypyrrole Organic Nanoparticles. Adv. Mater. 2012, 24, 5586-5592.

202. Yap, C. Y.; Chua, C. K.; Dong, Z. L.; Liu, Z. H.; Zhang, D. Q.; Loh, L. E.; Sing, S. L., Review of Selective Laser Melting: Materials and Applications. Appl. Phys. Rev. 2015, 2, 041101.

203. Ye, X.; Shi, H.; He, X.; Wang, K.; Li, D.; Qiu, P., Gold Nanorod-Seeded Synthesis of Au@ Ag/Au Nanospheres With Broad and Intense Near-Infrared Absorption for Photothermal Cancer Therapy. J. Mater. Chem. B 2014, 2, 3667-3673.

204. Yella, A.; Lee, H.-W.; Tsao, H. N.; Yi, C.; Chandiran, A. K.; Nazeeruddin, M. K.; Diau, E. W.-G.; Yeh, C.-Y.; Zakeeruddin, S. M.; Grätzel, M., Porphyrin-Sensitized Solar Cells With Cobalt (II/III)–Based Redox Electrolyte Exceed 12 Percent Efficiency. Science 2011, 334, 629-634.

205. Yoneda, H.; Morikami, H.; Ueda, K.-i.; More, R. M., Ultrashort-Pulse Laser Ellipsometric Pump-Probe Experiments on Gold Targets. Phys. Rev. Lett. 2003, 91, 075004.

206. Yu, H.; Baskin, J.; Steiger, B.; Wan, C.; Anson, F.; Zewail, A., Femtosecond Dynamics of Metalloporphyrins: Electron Transfer and Energy Redistribution. Chem. Phys. Lett. 1998, 293, 1-8.

207. Yu, H.-Z.; Baskin, J. S.; Steiger, B.; Anson, F. C.; Zewail, A. H., Femtosecond Dynamics and Electrocatalysis of the Reduction of O2: Tetraruthenated Cobalt Porphyrins. J. Am. Chem. Soc. 1999, 121, 484-485.

208. Yu, H.-Z.; Baskin, J. S.; Zewail, A. H., Ultrafast Dynamics of Porphyrins in the Condensed Phase: II. Zinc Tetraphenylporphyrin. J. Phys. Chem. A 2002, 106, 9845-9854.

209. Zarick, H. F.; Boulesbaa, A.; Talbert, E. M.; Puretzky, A.; Geohegan, D.; Bardhan, R., Ultrafast Excited-State Dynamics in Shape-and Composition-Controlled Gold–Silver Bimetallic Nanostructures. J. Phys. Chem. C 2017, 121, 4540-4547.

210. Zhang, J.; Averitt, R., Dynamics and Control in Complex Transition Metal Oxides. Annu Rev Mater Res 2014, 44, 19-43.

211. Zhao, Q.; Wang, Y.; Xu, Y.; Yan, Y.; Huang, J., Out-Of-Plane Coordinated Porphyrin Nanotubes With Enhanced Singlet Oxygen Generation Efficiency. Sci. Rep 2016, 6, 31339.

212. Zhao, T.; Steves, M. A.; Chapman, B. S.; Tracy, J. B.; Knappenberger Jr, K. L., Quantification of Interface-Dependent Plasmon Quality Factors Using Single-Beam Nonlinear Optical Interferometry. Anal. Chem. 2018, 90, 13702-13707.

213. Zimmerman, J. D.; Diev, V. V.; Hanson, K.; Lunt, R. R.; Yu, E. K.; Thompson, M. E.; Forrest, S. R., Porphyrin-Tape/C60 Organic Photodetectors with 6.5% External Quantum Efficiency in the Near Infrared. Adv. Mater. 2010, 22, 2780-2783.

Vita

Jeewan Chaminda Ranasinghe majored in Chemistry at University of Peradeniya, Sri Lanka, receiving his B.S. in Chemistry in 2010. He joined Professor Louis Haber's research group in the Department of Chemistry at Louisiana State University in the fall semester of 2014. Upon competition of his Ph.D. he will be working at University of California, Santa Barbara, as a Postdoctoral Research Scientist.